Vehicle-to-Vulnerable Road Users Channel Modeling in Critical Scenarios

vorgelegt von
M. Sc.
Ibrahim Rashdan
ORCID: 0000-0001-9208-8078

an der Fakultät IV - Elektrotechnik und Informatik
der Technischen Universität Berlin
zur Erlangung des akademischen Grades

Doktor der Ingenieurwissenschaften
-Dr.-Ing.-

genehmigte Dissertation

Promotionsausschuss:
Vorsitzender: Prof. Slawomir Stanczak
Gutachter: Prof. Giuseppe Caire
Gutachter: Prof. Uwe-Carsten Fiebig
Gutachter: Prof. Thomas Kürner
Tag der wissenschaftlichen Aussprache: 19. Mai 2023

Berlin 2023

Zusammenfassung

Nach Angaben der Weltgesundheitsorganisation fordern Verkehrsunfälle jedes Jahr weltweit etwa 1,35 Millionen Menschenleben und verursachen mehr als 50 Millionen Verletzungen. Fast die Hälfte der Verkehrsopfer sind Fußgänger, Radfahrer und Motorradfahrer. Diese Verkehrsteilnehmer sind im Straßenverkehr besonders gefährdet, wodurch sie auch als schwache Verkehrsteilnehmer oder Vulnerable Road Users (VRU) benannt werden. Die direkte Kommunikation zwischen Fahrzeugen und vulnerablen Verkehrsteilnehmern (V2VRU) kann Unfälle verhindern, indem sie eine Rundumsicht ermöglicht und die gegenseitige Erkennung und Lokalisierung von Fahrzeugen als auch von Verkehrsteilnehmern verbessert. Ein realistischer Kanal ist eine entscheidende Voraussetzung für die Entwicklung eines zuverlässigen V2VRU-Kommunikationssystems. Im Gegensatz zur Fahrzeug-zu-Fahrzeug- (V2V) und Fahrzeug-zu-Infrastruktur (V2I) Kommunikation wurde der V2VRU-Kommunikation in der Forschung noch nicht viel Aufmerksamkeit geschenkt. Ein dediziertes Kanalmodell für V2VRU-Kommunikation in kritischen Unfallszenarien ist noch nicht vorhanden. Um hier Abhilfe zu schaffen, zielt diese Arbeit darauf ab, die erste vollständige Parametrisierung eines geometriebasierten stochastischen Kanalmodells (geometry-based stochastik channel model, GSCM) für kritische Unfallszenarien in Städten zu erstellen. Zu diesem Zweck wurden experimentelle Single-Input-Single-Output (SISO)-Kanalmessungen sowohl im freien Feld als auch in städtischen Umgebungen durchgeführt. Für die Kanalmessungen wurden Signale mit einer Bandbreite von 120 MHz bei einer Trägerfrequenz von 5,2 GHz eingesetzt, die in der Nähe des 5,9-GHz-ITS-G5-Bandes und des 5,7-GHz-ISM-Bandes (Industrie, Wissenschaft und Medizin) liegen. Dabei wurden kritische Unfallszenarien mit Fahrzeugen und VRUs in den Messungen nachgestellt.

Obwohl sich eine Handvoll neuerer Studien mit dem Pfadverlust des Fahrzeug-Fußgänger-Kanals (V2P) befasst haben, ist nur wenig über die Auswirkungen der Mobilität des Fußgängers, der Behinderung durch geparkte Fahrzeuge und der Abschattung durch eine umgebende Menschenmenge auf die Empfangsleistung bekannt. In dieser Arbeit werden diese Aspekte untersucht und neue Modelle für den Pfadverlust vorgeschlagen. Außerdem wird der Beugungsverlust aufgrund der Behinderung durch geparkte Fahrzeuge berechnet und modelliert. Die Erkenntnisse über den Beugungsverlust werden außerdem durch Simulationen unterstützt, die zeigen, dass das Multiple-Knife-Edge Modell eine gute Übereinstimmung mit dem gemessenen Beugungsverlust bietet.

Es ist in der Literatur gut belegt, dass Fahrzeugkanäle nicht stationär sind. Um ein GSCM-Kanalmodell zu parametrisieren, ist daher die Kenntnis der Stationaritätsdistanz erforderlich. Die Nicht-Stationarität des V2VRU-Kanals wurde jedoch in der Literatur noch nicht analysiert. Daher wird in dieser Arbeit die Nicht-Stationarität des V2VRU-Kanals untersucht und die Stationaritätsdistanz geschätzt. Darüber hinaus wird festgestellt, dass die zeitvariante Kanalimpulsantwort (Channel Impulse Response, CIR) in der städtischen Umgebung durch diffuse Mehrwegekomponenten (Diffuse Multipath Components, DMCs) stark geprägt ist. Um eine Charakterisierung der reflektierte Mehrweg Komponenten (Specular Multipath Components, SMCs) zu ermöglichen, wird eine neuartige Methode zur Extraktion der SMCs aus der CIR basierend auf der Dichte ihrer benachbarten Mehrwegkomponenten vorgeschlagen. Darüber hinaus wird ein Algorithmus zur Verfolgung von SMCs über die Zeit auf der Grundlage ihrer Verzögerung und Amplitude vorgestellt. Um einen besseren Einblick in die Entwicklung des Funkkanals zu erhalten, wird die Position der Streuer in der Ausbreitungsumgebung mit Hilfe eines Algorithmus zur gemeinsamen Verzögerungs-und-Doppler-Schätzung ermittelt.

Schließlich wird in dieser Arbeit eine vollständige Parametrisierung für das GSCM vom WINNER-Typ vorgeschlagen. Insbesondere werden die Kanalparameter und ihre (Kreuz-) Korrelationen im log-Bereich geschätzt. Die Ergebnisse zeigen, dass die lognormale Verteilung eine gute Annäherung an die Verteilungen der Kanalparameter bietet. Nach der Parametrisierung werden Kanalsimulationen mit dem quasi deterministischen Funkkanalgenerator (QuaDRiGa) durchgeführt.

Abschließend wird der GSCM mit den vorgeschlagenen Parametern validiert. Die Kanalvalidierung zeigt, dass das vorgeschlagene Modell eine sehr gute Darstellung des V2VRU-Ausbreitungskanals in den betrachteten Szenarien liefert. Daher kann das vorgeschlagene Kanalmodell in Simulationen verwendet werden, um V2VRU-Kommunikation und Kollisionsvermeidungsalgorithmen in kritischen Unfallszenarien zu entwickeln und zu bewerten.

Abstract

According to the world health organization, traffic accidents take about 1.35 million lives and cause more than 50 million injured persons globally each year. Vulnerable road users (VRUs), i.e., pedestrians, cyclists and motorcyclists, account for almost half of the road victims. Direct vehicle-to-VRU (V2VRU) communication can prevent accidents by providing 360° awareness and improving detection, localization, and tracking of both vehicles and VRUs. Having a realistic channel is a prerequisite for developing a reliable V2VRU communication system. Contrary to vehicle-to-vehicle (V2V) and vehicle-to-infrastructure (V2I) communications, V2VRU communication did not attract much attention in research. A dedicated channel model for V2VRU communication in critical accident scenarios is still missing. In order to remedy this situation, this thesis aims to provide the first full parametrization for a geometry-based stochastic channel model (GSCM) for critical urban scenarios. For this purpose, experimental single-input single-output (SISO) channel measurements were conducted in both open-field and urban environments. The measurements were carried out at a carrier frequency of 5.2 GHz which is close to the 5.9 GHz ITS-G5 band and to the 5.7 GHz industrial, scientific and medical (ISM) band. The measurements were executed with a bandwidth of 120 MHz taking into account the most critical accident scenarios involving vehicle and VRUs.

Even though a handful of recent studies addressed the path loss of the vehicle-to-pedestrian (V2P) channel, little is known about the impact of the pedestrian mobility, obstruction by parked vehicles, and shadowing by a crowd surrounding the pedestrian on the received power. In this thesis, these aspects are investigated and path loss models are proposed. Moreover, the diffraction loss due to the obstruction of parked vehicles is calculated. The findings on the diffraction loss are then verified

by simulations. It is shown that the multiple knife-edge model provides a good match to the measured diffraction loss.

Note that it is well established in literature that vehicular channels are non-stationary. Therefore, in order to parameterize a GSCM channel model, the stationarity distance is required. However, the non-stationarity of the V2VRU channel has not yet been analyzed in literature. Hence, in this work, the non-stationarity of the V2VRU channel is investigated and the stationarity distance is estimated. Furthermore, the time-variant channel impulse response (CIR) in the urban environment is found to be highly cluttered by diffuse multipath components (DMCs). To allow for further characterization of the specular multipath components (SMCs), a novel method is proposed to extract the SMCs from the CIR based on the density of their neighboring multipath components (MPCs). Further, an algorithm for tracking SMCs over time based on their delay and magnitude is presented. In order to gain more insight on the evolution of the radio channel, the locations of all scatterers in the propagation environment are estimated by employing a joint delay-Doppler estimation algorithm.

Finally, the thesis proposes a full parametrization for the WINNER-type GSCM. In particular, the large scale parameters (LSPs) and their correlations are estimated in the log domain. The results show that the log-normal distribution provides a good fit to the distributions of the LSPs. Following the parameterization, channel simulations are performed with the quasi deterministic radio channel generator (QuaDRiGa) implementation. Thereafter, the GSCM with the proposed parameters is validated. The channel validation shows that the proposed model provides a very good representation for the V2VRU propagation channel in the considered scenarios.

The proposed channel model can be used in simulations to develop and evaluate V2VRU communication and collision avoidance algorithms in critical accident scenarios.

List of Published Content

The thesis is in part based on seven original publications. The author has had the main responsibility for performing the analysis and writing all the papers.

1. I. Rashdan, S. Sand, S. Jiang, W. Wang, and G. Caire. "Non-Stationarity Analysis of Vehicle-to-Vulnerable Road Users Channel in Critical Scenarios". In: *2023 17th European Conference on Antennas and Propagation (EuCAP)*, 2023.

2. I. Rashdan, P. Unterhuber, F. de Ponte Müller, S. Sand, and G. Caire "Diffuse Multipath Analysis of Vehicle-to-Vulnerable Road User Channel in Urban Environment". In: *2021 15th European Conference on Antennas and Propagation (EuCAP)*, 2021.

3. I. Rashdan, F. de Ponte Müller, S. Sand, T. Jost, and G. Caire "Measurement-based Geometrical Characterisation of the Vehicle-to-Vulnerable-Road-User Communication Channel". In: *IET Microwaves, Antennas and Propagation*, 2020.

4. I. Rashdan, M. Walter, W. Wang, and G. Cair "Large Scale Fading Characteristics for Vehicle-to-Cyclist Channel in Urban Environment at 5 GHz". In: *2020 14th European Conference on Antennas and Propagation (EuCAP)*, 2020.

5. I. Rashdan, F. de Ponte Müller, T. Jost, and S. Sand "Measurement-based Geometrical Characterization of the Vehicle-to-Pedestrian Channel". In: *2019 13th European Conference on Antennas and Propagation (EuCAP)*, 2019.

6. I. Rashdan, F. de Ponte Müller, T. Jost, S. Sand, and G. Caire "Large-Scale Fading Characteristics and Models for Vehicle-to-Pedestrian Channel at 5-GHz". In: *IEEE Access*, 2019.

7. I. Rashdan, F. de Ponte Müller, W. Wang, M. Schmidhammer, and S. Sand "Vehicle-to-Pedestrian Channel Characterization: Wideband Measurement

Campaign and First Results". In: *IEEE 12th European Conference on Antennas and Propagation (EuCAP)*. London, UK, Apr. 2018.

To my parents

Acknowledgements

First and foremost, I wish to express my deepest gratitude to my supervisor Prof. Giuseppe Caire for giving me the opportunity to pursue my Ph.D. studies under his guidance. I am very grateful for the help of Dr. Stephan Sand, my co-supervisor Dr. Fabian de Ponte Müller, and Prof. Uwe-Carsten Fiebig for their invaluable guidance, encouragement, and support. Furthermore, I am thankful to Prof. Thomas Kürner for his interest and the examination of this thesis.

Thanks to all my colleagues for all the fruitful discussions we had, and their support in conducting the measurement campaigns. I am fortunate to work in such friendly environment that you created.

I am especially grateful to my dear friends, Adnan, Ammar, Dina, Nayef, Soli, and Yazan. Thanks for sharing all the happiness and sadness. I feel so lucky to have you in my life. Above all, I would like to thank my family; my parents and siblings. I would never have made it this far without your unconditional support and love.

Ibrahim Rashdan

Gilching, July 2022

Table of Contents

List of Figures

List of Tables

Acronyms

AoA	Angle of arrival
AoD	Angle of departure
APDP	Average power delay profile
AS	Angular spread
ASA	Azimuth spread of arrival
ASD	Azimuth spread of departure
C-V2X	Cellular-vehicle-to-everything
CDF	Cumulative distribution function
CIR	Channel impulse response
COST	European cooperation in science and technology
DMC	Diffuse multipath component
DPSS	Discrete prolate spheroidal sequence
DS	RMS delay spread
DSRC	Dedicated short range communication
FBS	First-bounce scatterer
GDP	Gross domestic product
GLoS	Geometric LoS
GLSF	Generalized local scattering function
GO	Geometrical optics

GSCM	Geometry-based stochastic channel model
KEST	Kalman enhanced super resolution tracking
KF	Narrowband K-factor
LBS	Last-bounce scatterer
LoS	Line of sight
LQS	Local quasi-stationarity
LSF	Local scattering function
LSP	Large scale parameter
LTE	Long term evolution
MPC	Multipath component
MRA	Modified reverse arrangement test
OLoS	Obstructed-line of sight
PDP	Power delay profile
PDR	Packet delivery ratio
RMS	Root-mean-square
RSSI	Received signal strength indication
RT	Ray-tracing
Rx	Receiver
SAGE	Space-alternating generalized expectation-maximization
SCM-E	Spatial channel model-extended
SF	Shadow fading
SISO	Single-input single-output
SMC	Specular multipath component
TDL	Tapped-delay line

Tx	Transmitter
US	Uncorrelated scattering
V2I	Vehicle-to-infrastructure
V2P	Vehicle-to-pedestrian
V2V	Vehicle-to-vehicle
V2VRU	Vehicle-to-vulnerable road user
V2X	Vehicle-to-everything
VRU	Vulnerable road user
WINNER	Wireless world initiative for new radio
WSS	Wide-sense stationary
WSSUS	Wide-sense stationary uncorrelated scattering

1 Introduction

1.1 Motivation

In recent decades, road traffic has increased enormously due to the rapid growth of population and cities. One major drawback of this expansion is the increase of road traffic accidents. According to the World Health Organization, traffic accidents take about 1.35 million lives and result in more than 50 million injured persons globally each year with an associated governmental cost of about 3 % of the gross domestic product (GDP) [1]. Vulnerable road users (VRUs), i.e., pedestrians, cyclists and motorcyclists, account for almost half of the road victims. Based on accident statistics reported in [2] and [3], the most critical pre-crash scenarios that involve pedestrians and cyclists occur in urban environments. In these scenarios, shown in Figure 1.1, the driver visibility toward the pedestrian and cyclist is blocked by buildings at intersections or by parked vehicles along the roadside.

Currently, driver assistance systems and automated vehicles only rely on their own perception sensors to detect and locate other surrounding traffic participants. However, radar sensors, laser-scanners, and camera-based systems have one critical limitation: They require a direct line-of-sight (LoS) towards the other road users. Additionally, light-based systems show a low performance under adverse weather

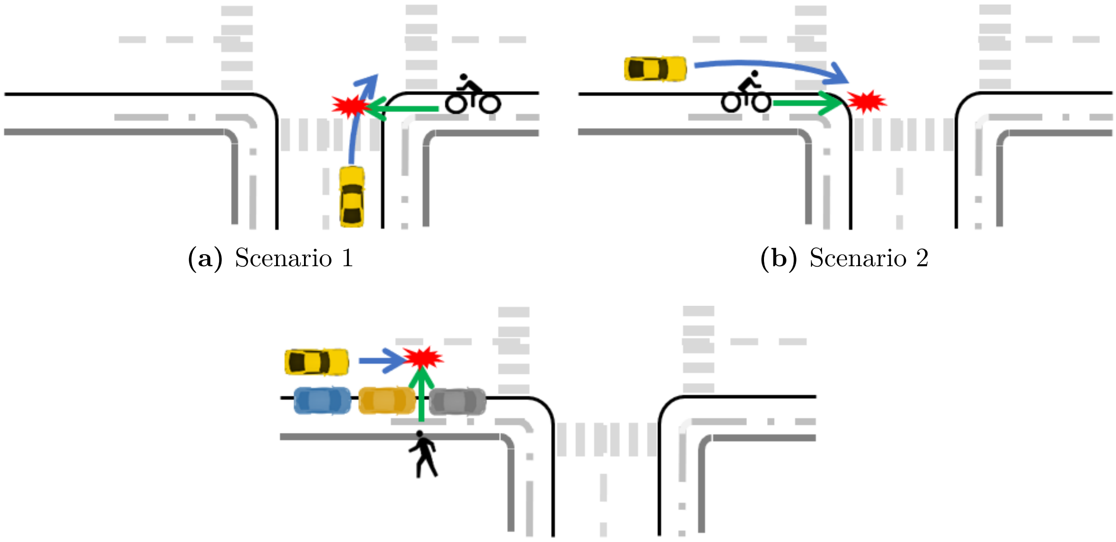

(a) Scenario 1

(b) Scenario 2

(c) Scenario 3

Figure 1.1: Illustrations of the most critical accident scenarios in urban environments.

or lighting conditions [4, 5, 6]. One way to overcome this limitation and obtain 360 degree of awareness is to use a communication technology to directly exchange information between vehicles and VRUs [7, 8]. Using vehicle-to-VRU (V2VRU) communication, also called vehicle-to-pedestrian (V2P) communication, can improve mutual detection, localization, and tracking of both vehicles and VRUs. Each vehicle and VRU periodically transmits its position and heading. Using this information, a collision avoidance system can trigger warning messages when a potential collision is detected. V2VRU communication is part of the vehicle-to-everything (V2X) communication which also includes vehicle-to-vehicle (V2V) and vehicle-to-infrastructure (V2I) communications. V2X communication has the potential to increase safety and efficiency of transportation systems. There are two main technologies that enable the V2X communication, i.e., WiFi-based and cellular-based technologies. Dedicated short range communication (DSRC) in the US or ITS-G5 in Europe are IEEE 802.11p-based technologies, which were developed over a decade ago. The 3GPP consortium is incorporating V2X communication capabilities into their long term evolution (LTE) standard under the name LTE-V2X or cellular-V2X (C-V2X) communication. The reliability of the safety application is highly dependent on the quality of the communication link between vehicles and VRUs, which relies on the properties of the propagation channel. Therefore, profound knowledge of the propagation channel is a prerequisite for the development of the communication system. Hence, in order to develop a reliable communication system and evaluate its performance, realistic channel models are required.

Several channel models were proposed for V2V and V2I communications [9, 10, 11]. However, different from V2V and V2I, V2VRU does not attract similar attention in research. To the best of the author's knowledge, a dedicated channel model for V2VRU communication in realistic and critical accident scenarios in urban environments is still missing.

Since the vehicle is a common element in V2V, V2I and V2VRU, some similarities potentially arise in the propagation channel. Assuming that a safety system based on V2VRU communication is incorporated in the pedestrian's or cyclist's smartphone, important differences in the propagation channel can be identified due to:

- The mobility pattern and velocity of the VRU
- The changing antenna height and orientation depending on the smartphone's location and VRU's activity (texting, phoning, etc)
- The relatively low height of the VRU's smartphone antenna, such that the LoS could be partially or completely obstructed by road side objects, e.g. trees, moving or parked vehicles and surrounding VRUs.

These aspects will impose different propagation characteristics. Signals may experience additional attenuation and thus they need to be accounted for when developing the channel model. To derive an accurate model, the V2VRU channel has to be thoroughly investigated. These channel models should be able to reproduce reliably and with low complexity the time-variant behavior of the channel characteristics. Additionally, due to the movement of the transmitter (Tx), the receiver (Rx) and the scatterers, the relatively low antenna heights and the resulting variability of the multipath richness of the environment, the V2VRU channel is non-stationary [12]. This non-stationarity needs to be considered which makes characterizing and modeling the channel more difficult and challenging.

Channel models can be broadly divided in three categories: deterministic, stochastic, and geometry-based stochastic channel models (GSCMs). The two main factors that influence the decision of which modeling approach to follow are the complexity and the accuracy of the model. Taking the non-stationarity nature of the V2VRU channel into account, a deterministic approach can provide a highly accurate and realistic channel model. However, it is site-specific and requires intensive and time consuming computations. Stochastic models, on the other hand, have relatively low complexity which makes them easy to use. Yet, they are inadequate to produce realistic models for non-stationary channels [13]. Combining the geometrical and statistical elements of the deterministic and stochastic models, GSCMs provide accurate geometrical relations with a reduced computational cost. Moreover, GSCMs are found to be well suited for non-stationary environments [12]. Therefore, we have chosen the GSCM approach in modeling the V2VRU channel in this thesis. The two main types of GSCMs are the COST 2100 which has been defined within the European cooperation in science and technology [14] and the wireless world initiative for new radio (WINNER II) [15]. Since the COST 2100 channel model, on the one hand, is cluster-centric, it requires to draw the distribution of the scattering clusters from the measurement data. Unfortunately, our collected data are based on single-input single-output (SISO) measurements, which limits the ability to accurately acquire such distributions. On the other hand, the WINNER-type channel model is user-centric, i.e., the placement of the scatterers in the simulated propagation environment is based on the large scale parameters (LSPs). These LSPs can be estimated based on the measurement data. Therefore, the WINNER-type channel model is chosen in this work. More details about channel modeling approaches are presented in Section 2.2.

1.2 Contribution and Structure of this Thesis

This thesis aims at characterizing and modeling the V2VRU channel based on channel sounding measurements in critical accident scenarios. During the work on this thesis, the author published, as first author, two journal papers [16, 17] and eight conference papers [18, 19, 20, 21, 22, 23, 24, 25]. Four of the conference papers

[18, 19, 20, 21] considered several aspects related to V2X communications, and are not directly related to the topic of this thesis. For reasons of consistency, this work is not included in this thesis.

The following paragraphs provide an overview of the structure and contribution of this thesis.

Chapter 2 gives an overview of the propagation channel fundamentals by first describing the different electromagnetic wave propagation mechanisms. Next, different approaches for channel modeling are briefly discussed, and the recent developments in V2VRU channel modeling are presented. Finally, a description of the proposed channel model is provided, followed by a detailed explanation of the channel coefficient generation procedure.

Chapter 3 provides a detailed description of the two SISO channel measurement campaigns. Both campaigns were conducted using the RUSK-DLR channel sounder at a carrier frequency of $f_c = 5.2\,\mathrm{GHz}$ and with a bandwidth of $B = 120\,\mathrm{MHz}$. The first campaign presented in Section 3.1 was conducted in an open-field environment considering an accident scenario between a vehicle and a pedestrian [22]. This location was chosen since it represents a controlled environment with only a small number of far-located scatterers. Therefore, the location makes it possible to isolate and study the impact on the propagation channel caused by the different elements in the propagation environment, as well as by the mobility of the Tx and Rx. In Section 3.2, the second measurement campaign that was conducted in an urban environment is described. The three most critical accident scenarios involving pedestrians and cyclists were considered. The proposed channel model in this thesis is based on data collected during this campaign.

To make the contributions clearer, Figures 1.2 and 1.3 illustrate the main contributions and the flow of the work that has been followed in this thesis in open-field and urban environments.

Chapter 4 addresses several aspects of channel modeling. In Section 4.1, path loss models for open-field and urban channel are proposed [16, 23]. The path loss does not only provide valuable insight into the impact of the propagation environment on the received power, but it is also used as an input to the channel model. Moreover, the spatial correlation of the shadow fading can lead to degradation in the communication

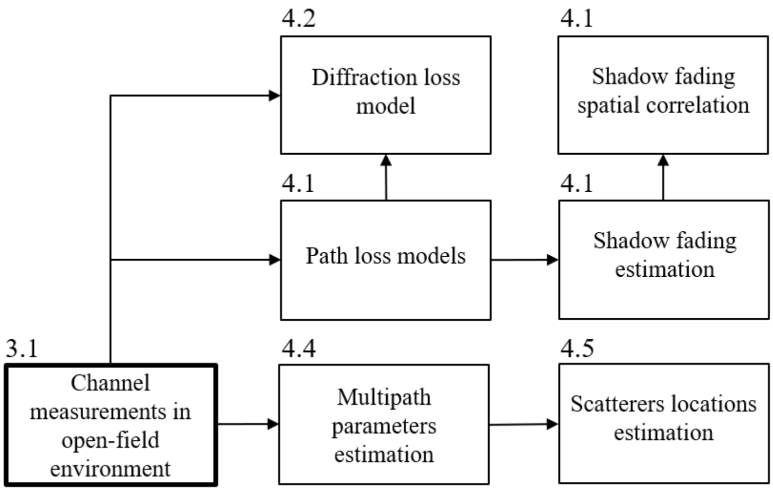

Figure 1.2: Illustration of the main contributions and the flow of the work that has been followed in this thesis based on the *open-field* measurements. The number near the top-left corner of each box indicates the number of the section or chapter in which the topic is introduced.

performance. Therefore, the spatial correlation of the shadow fading in open-field is analyzed and models are proposed [16]. To study the propagation loss due to the obstruction of the LoS by parked vehicles, a 3D tool has been developed in Section 4.3. The tool detects the diffraction edges and calculates the Fresnel-Kirchoff parameter that is used to calculate the knife-edge diffraction loss.

Due to the non-stationarity of the V2VRU channel, the channel is characterized by dividing it into regions where the wide-sense stationary uncorrelated scattering (WSSUS) assumption holds and then the LSPs are estimated in each individual region. In Section 4.4, the non-stationarity of the V2VRU channel is analyzed by estimating the generalized local scattering function (GLSF) and its collinearity based on the channel measurement data in the urban environment, and the estimated stationarity distance is presented. In Section 4.5, the multipath parameters are estimated using the Kalman enhanced super resolution tracking (KEST) algorithm. To separate the specular multipath components (SMCs) and the diffuse multipath components (DMCs), a novel method is proposed to extract specular reflections from the estimated time-variant channel impulse responce (CIR) based on the density of their neighboring multipath components (MPCs). This extraction allows for further characterization of the specular reflections. Furthermore, a simple but effective algorithm for multipath tracking based on the differences in delay and magnitude between SMCs is presented [17]. Based on the previous step, in Section 4.6, the SMC parameters are employed to localize the physical scatterers in the propagation environment using a joint delay-Doppler estimation algorithm [17, 24]. The estimated positions of the scatterers are then used to estimate the angle of departure (AoD) and angle of arrival (AoA) of the SMCs. In Section 4.7, the DMCs are extracted in order to calculate their contribution to the total received power [25].

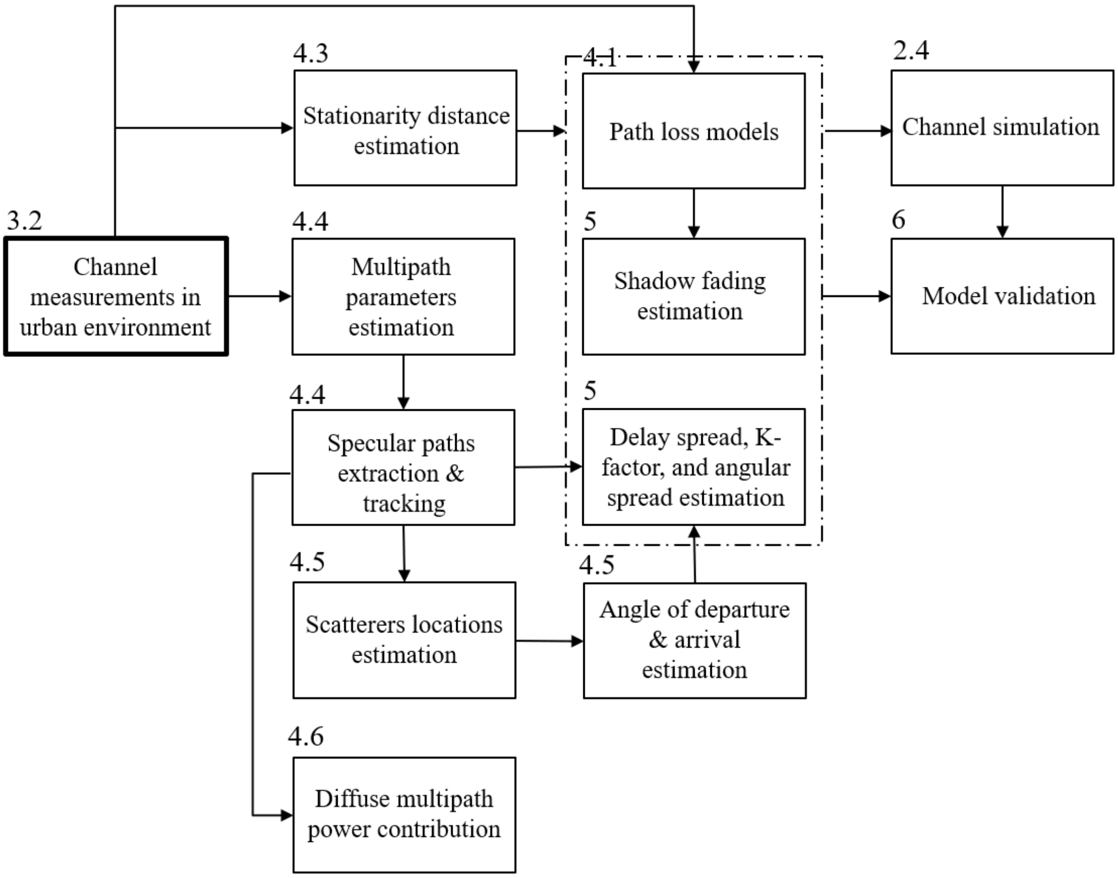

Figure 1.3: Illustration of the main contributions and the flow of the work that has been followed in this thesis based on the *urban* measurements. The number near the top-left corner of each box indicates the number of the section or chapter in which the topic is introduced. The output of the dashed box contains the model parameters, which are used as an input for the simulation, and as validation metrics.

Chapter 5 explains how the LSPs are estimated and modeled. For developing a WINNER-type GSCM for V2VRU propagation channel, the LSPs are estimated in the power and delay domain, i.e., shadow fading (SF), root-mean-square (RMS) delay spread (DS), and narrowband K-factor (KF), and in the angular domain, i.e., azimuth spread of departure (ASD), and azimuth spread of arrival (ASA). In order to maintain the spatial correlation of the LSPs observed in the measured channel, the autocorrelations of these LSPs are analyzed and the correlation distances are calculated. Furthermore, to ensure spatial consistency, the cross-correlation coefficients among the LSPs are calculated. The model parameters are then used as an input to the simulator.

Chapter 6 presents the validation of the SISO channel model. The simulated channels are generated by the WINNER-type QuaDRiGa simulator described in Chapter 2. By comparing the distributions of the model parameters extracted from the simulated channels with their counterparts extracted from the measured channels and used as input to the proposed model, the simulated and measured channels are compared qualitatively. In addition to the distributions of the LSPs, the correlation distance of each LSP as well as the cross-correlation between each pair of LSPs is also considered in the validation process. The channel validation reveals that the proposed model represents the V2VRU propagation channel in the considered scenarios very well.

Finally, **Chapter 7** gives a brief summary of this thesis, and presents future research directions.

2

Wave Propagation and Channel Modeling Fundamentals

This chapter provides an overview of wave propagation and channel modeling fundamentals. The main electromagnetic wave propagation mechanisms are described. Next, different approaches for channel modeling are briefly discussed and the recent development in V2VRUs channels are summarized. Finally, a description of the proposed channel model is provided, followed by a detailed explanation of the channel coefficient generation procedure.

2.1 Wave Propagation Mechanisms

In wireless communication systems, the emitted electromagnetic wave from the transmitting antenna travels to the receiving antenna on different paths. This effect is called multipath propagation and occurs due to different wave propagation mechanisms such as reflection, scattering, and diffraction. The received signal is therefore a superposition of a number of attenuated, delayed, and phase-shifted copies of the transmitted signal. Generally, in real urban environments there are various objects with different sizes and materials such as trees, buildings, cars, and traffic signs. When an electromagnetic wave travels in an urban environment, it interacts with these objects and different propagation mechanisms can occur depending on the sizes and electromagnetic properties of these objects. In the following paragraphs, these propagation mechanisms are briefly discussed.

Reflection

Specular reflection occurs when the wave impinges on a smooth surface that has large dimension compared to the incident wavelength [26]. In urban vehicular communication, reflection usually occurs on the earth surface, buildings, parked and moving vehicles, and traffic signs. The angle of reflection is equal to the angle of incidence and the amount of the reflected energy depends on electromagnetic properties of the material [27, 28], the incident angle, and the wave polarization.

Scattering

Scattering occurs when the electromagnetic wave has a wavelength much larger than the dimensions of the interacting object in the propagation environment [26]. Scattering may also occur on non-uniform or rough surfaces and in this case it is called diffuse scattering [29]. Contrary to reflection surfaces in indoor environments, reflection surfaces in outdoor environments are typically rough. The roughness of the surface causes the impinging wave to be scattered in non-specular directions. Furthermore, the non-specular components could be stronger than the specular component in some cases.

Diffraction

Diffraction describes the bending of waves around edges or corners of objects with dimensions larger than the wavelength [27]. The diffraction phenomenon can be explained by Huygen's principle. According to Huygen's principle, all points on a wavefront act as point sources of secondary wavelets which contribute to generate a new wavefront that propagates into the shadowed region. The power of the diffracted wave experiences considerable loss. However, the diffracted waves can have a significant contribution to the total received power. The diffraction loss can be predicted by the single and multiple knife-edge diffraction models [30]. Several methods are proposed in literature to calculate the diffraction loss based on the multiple knife-edge diffraction model such as Bullington, Japanese, Epstein-Peterson, and Daygout methods [31].

2.2 Wireless Channel Models

A channel model aims to represent the wireless propagation channel. It is a tool used to design, simulate, and analyze a communication system. Through channel modeling, an understanding of the channel evolution and its properties is acquired which allows to design a reliable communication system. Channel models can be broadly divided in three categories: deterministic, stochastic, and Geometry-based stochastic channel models (GSCMs). In the following subsections, these types of channel models are briefly described.

2.2.1 Deterministic Channel Models

A deterministic channel model is a site-specific model used to characterize the propagation channel in a specific environment through simulations. Ray-tracing (RT) is considered the most popular approach in the deterministic channel modeling in both indoor and outdoor environments [32, 33]. The RT approach simulates the reflection and diffraction of waves based on the geometrical optics (GO) model [34]. In GO, the wavelength is assumed to be relatively small when compared with the dimensions of objects in the propagation environment. The RT is initialized with the position of the Tx and the Rx, then each path is described by straight lines, or rays, where all propagation paths between the Tx and the Rx are determined by geometric considerations. At the Rx side, the received MPCs are characterized by their amplitude, delay and phase, and then the channel is obtained by the superposition of all MPCs.

A deterministic approach can produce highly accurate and realistic representations of the wireless propagation channel in a certain scenario [35]. However, it requires detailed geometrical representation to characterize the channel environment. Therefore, using RT requires intensive and time consuming computations, and it is not easily used for system-level simulations. Also, it is very cumbersome to capture and enter all the relevant details of the physical environment into the ray-tracer, especially in outdoor environments.

2.2.2 Stochastic Channel Models

Stochastic channel models statistically describe the radio propagation channel by means of probability distributions derived from the measurement data. Stochastic channel models, e.g., the tapped-delay line (TDL) model, are widely used for cellular communications and have been used as a reference model for IEEE 802.11p standard [36, 37]. The TDL models provide statistics for the received power at a certain Doppler, delay and angle under the assumption of WSSUS. However, under the WSSUS assumption, the statistics of each delay tap are time-invariant (WSS) and are independent between each delay tap (US). Therefore, the TDL models are only valid within the stationarity region as they lack the ability to describe the transition between stationarity regions. Therefore, stochastic TDL models are inadequate to produce realistic models for non-stationary channels such as vehicular channels, which results in a poor estimation of the communication system performance [13]. The key advantage of stochastic models is that they are mathematically simple and have relatively low complexity, which makes them easy to use.

2.2.3 Geometry-based Stochastic Channel Models

By combining the geometrical and statistical elements of the deterministic and stochastic channel models, GSCMs provide accurate geometrical relations at a reduced computational cost. Moreover, GSCMs are found to be well suited for non-stationary environments [12]. GSCMs can be further divided into two types, namely, the European cooperation in science and technology (COST) and the wireless world initiative for new radio (WINNER). The COST-type GSCMs, on the one hand, are cluster-centric models that geometrically place random scattering clusters, drawn from specific distributions, in the simulated propagation environment. These distributions are derived from the channel measurement data [14]. These scatterers, i.e., clusters, fade in and out based on their visibility regions, which in turn depend on the positions of the Tx and the Rx. The LSPs are then synthesized based on the visible scatterers to the Tx and Rx. The COST channel models support continuous time evaluation of the channel. However, the parameterization of the clusters is challenging. The WINNER-type GSCMs, on the other hand, are user-centric, i.e., the placement of the scatterers in the simulated propagation environment is based on the estimated LSPs. Hence, the LSPs control the behavior of the channel and describe the distribution of the received power over the delay and angular domains. Several extensions of the WINNER-type GSCM have been proposed during the last decade, such as WINNER II [15], WINNER+ [38], 3GPP-3D [39], and the QuaDRiGa [40] models.

2.3 State of the Art

Several channel models were proposed for V2V and V2I communications [9], [11], [41], [42]. However, to the best of the author's knowledge, a dedicated channel model for V2VRU communication in realistic and critical accident scenarios in urban environment is still missing.

There are only a handful of recent studies focused on modeling different aspects of the V2VRU channel. The authors in [43] performed V2P channel measurements at 3.8 GHz and with a bandwidth of 200 MHz. Based on the measurements in the LoS scenario, the authors presented a two-ray path loss model for the strongest path contribution, and log-distance path loss model for the path loss of discrete scatterers. Normal and Ricean distributions for large and small scale fading were also reported. The authors extended this work to a LoS/Non-LoS (NLoS) scenario in [44], where a multi-slope log-distance path loss model is proposed. The authors in [45] investigated the autocorrelation function of the V2P channel in LoS and partial LoS scenarios. According to their findings, the channel decorrelates rapidly in time domain which indicates a non-stationary behavior of the V2P channel. In [46], the authors investigated the first-order characteristics of the V2P channel at 5.8 GHz in a business district environment. The K-factor was calculated for different locations of the Tx and Rx antennas and vehicle speeds. However, their work was based on narrowband received signal strength indication (RSSI) measurements. The path loss was studied in [47] based on narrowband channel measurements in LoS when the pedestrian is standing as well as when the pedestrian is moving along the road.

Further studies related to V2VRU communication can be found in the literature. However, their focus is on evaluating the performance of a V2P communication system based on narrowband measurements and simulations. For instance, the authors in [48] conducted a study on the applicability of WiFi-based communication for V2P scenarios. The authors evaluated the performance of the communication in terms of packet delivery ratio (PDR) and packet inter-reception time. Based on experiments, they found out that, in order to satisfy a collision avoidance application, a transmission rate greater than 1 Hz is required. In [49], the performance of IEEE 802.11p-based V2P communication was evaluated and compared with WiFi and cellular-based communications. The PDR and end-to-end latency in LoS and NLoS scenarios were calculated. The authors reported that LTE-based communication yields better PDR than IEEE 802.11p while the latter one yields a lower latency. WiFi-based communication shows worse performance than the IEEE 802.11p in terms of both, PDR and latency. Honda and Qualcomm developed an IEEE 802.11-based pedestrian safety system in [7]. They implemented a DSRC stack within the WiFi chipset on a smartphone. To lower the smartphone's power consumption, a false-alarm suppression algorithm was developed. The communication performance was studied in terms of RSSI and inter-reception time. In [8], the use of IEEE 802.11p-based communication between VRUs and vehicles was addressed. The authors conducted experiments using Cohda MK4 communication units. They found out that the obstacles located between the Tx and the Rx had a severe impact on the achievable communication range. The authors in [50] considered an intersection scenario at which they evaluated the performance of the IEEE 802.11p-based V2P communication for crash avoidance application through simulations. Their results showed that even in scenarios with relatively low channel load, there was a significant loss of packets. According to their results, lower packet inter-reception time can be achieved by choosing higher-order modulations in IEEE 802.11p. A number of other studies proposed using cellular-based communication instead of direct ad-hoc V2VRU communication to enable VRU protection systems (e.g., [51] and [52]).

2.4 Channel Model Description

The modeling approach in this thesis follows the QuaDRiGa modeling approach [40]. the QuaDRiGa model extends the well known WINNER II [15] and WINNER+ [38] models by adding time evolution and 3D propagation. In this model, the trajectories of both the Tx and the Rx are divided into segments. A channel segment can be seen as a part of the Tx and the Rx trajectories, in which the LSPs do not change considerably. The positions of the scatterers are calculated based on the LSPs. Within a channel segment, the scatterer positions are fixed. However, due to the movement of the Tx and the Rx within the segment, the propagation path parameters, i.e, the power, delay, phase, and angles will change. The time evolution of the channel due to the movement of the Tx and Rx is accomplished by the so-called drifting and the birth/death of the scatterers. Drifting deals with the time evolution inside a channel segment. It was introduced in spatial channel model-extended (SCM-E) [53]. When the Tx and the Rx move from one channel segment to another, different scatterers will be created. The birth and death process of the scatterers ensures a smooth transition between adjacent channel segments.

2.4.1 Model Parameters

The model parameters are divided into two sets. The first set of parameters are the LSPs. The second set contains the supporting parameters.

Large scale parameters : The following five LSPs describe the distribution of the power over the delay and angular dimensions and control the evolution of the channel model.

- Shadow fading (SF)
- RMS delay spread (DS)

- Ricean K-factor (KF)
- Azimuth spread of departure (ASD)
- Azimuth spread of arrival (ASA)

The distributions of the LSPs are obtained from the parameters of the SMCs, i.e.,the power, delay, and angles, that are estimated in Sections. 4.5 and 4.6. All LSPs are modeled with log-normal distribution with mean μ and standard deviation σ.

Supporting parameters : The following supporting parameters are estimated from the LSPs and the measured channels.

- Correlation distance of the LSPs
- Cross-correlation of the LSPs
- Number of scattering clusters
- Scaling coefficient for delay distribution
- Scaling coefficient for angle of departure distribution
- Scaling coefficient for angle of arrival distribution

The correlation distance, also called the decorrelation distance, is a scenario-dependent parameter that determines how long the channel is assumed stationary for a specific LSP [15, 40]. The cross-correlations between each pair of the LSPs form a positive definite correlation matrix. They introduce the inter-dependency between the LSPs. The scaling coefficients are also called the proportionality factors [15]. They are used to scale path delays and angles to ensure that the differences in the spreads are reflected in the powers.

All these parameters will be used to generate the channel coefficients that will be explained in the following subsection. The method used to obtain the LSPs and the supporting parameters will be addressed in Chapter 5.

2.4.2 Generation of the Channel Coefficients with QuaDRiGa

The block diagram in Figure 2.1 shows the procedure of the channel generation. In the first step, the network layout is created by defining the number of the Tx and the Rx and antenna configurations. The user then needs to provide the trajectories of the Tx and the Rx. Both the Tx and the Rx move along their trajectories and each of them has a list of positions defining the trajectory. Since the Tx and the Rx could move with different speeds, their trajectories may have different lengths. However, both trajectories have the same number of snapshot positions. The trajectories are divided into 8 segments with a minimum length of 5 m, an average length of 15 m, and a standard deviation of 5 m. Since a segment can be seen as an interval in which the LSPs do not change considerably, these parameters that define the length of the segments are roughly drawn from the correlation distances of the LSPs that are evaluated in Chapter 5. The segments of the Tx and the Rx are identical. As an example, if a segment that has a length of 2000 measurement snapshots begins at snapshot number 501 and ends at snapshot number 2500 of the Tx trajectory, it would also start at snapshot number 501 and end at snapshot number 2500 of the Rx trajectory. The segments are then classified as LoS, obstructed-LoS (OLoS), or NLoS based on the propagation situation of the channel within the segment in the considered scenario. For example, in Scenario 1 (see Figure 1.1), the LoS starts to appear at Tx-Rx distance of 15 m after being obstructed by buildings, therefore, all segments that correspond to Tx-Rx distance large than 15 m are classified as NLoS, and the rest are classified as LoS segments.

In the following, the main steps of the channel coefficients generation are summarized. A more detailed description is found in [15, 40].

A. Calculation of correlated LSP maps

For each LSP, a 2D map is generated. The map gives local values of the LSP at each Tx and Rx position. Moreover, the spatial correlation of the LSP as well as its cross-correlation with other LSPs are applied in the map. To clarify, let us consider the example of the SF discussed in Section 4.2. When the receiver moves to a shadowed area, it remains shadowed for some time or corresponding

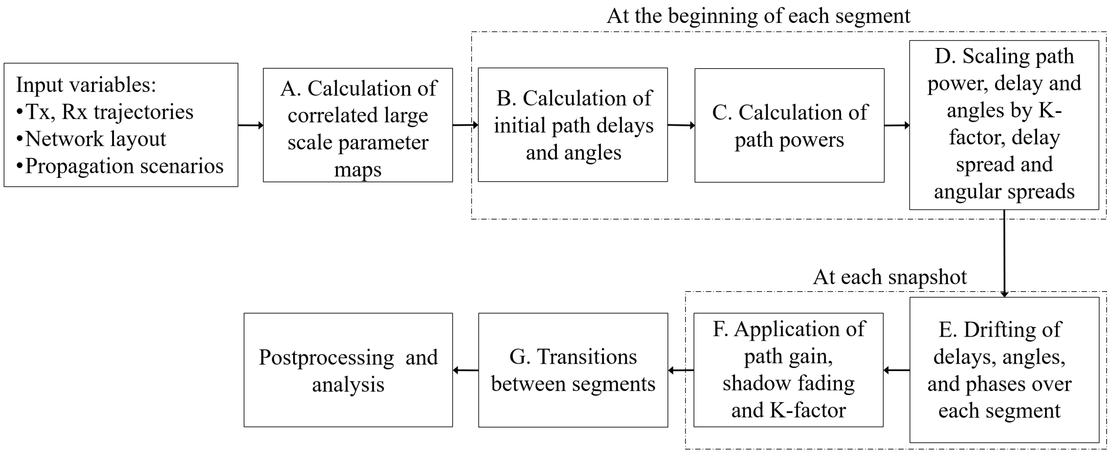

Figure 2.1: Steps for calculation of time-evolving channel coefficients.

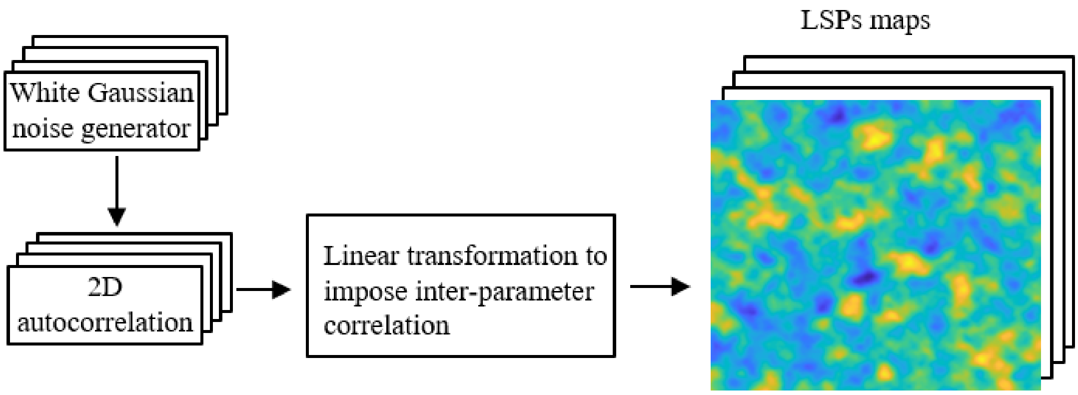

Figure 2.2: Principle of the generation of correlated LSPs maps.

traveled distance. This implies that shadowing is spatially correlated. The spatial correlation can be captured by using 2D SF map. As illustrated in Figure 2.2, based on the Gaussian model, a random (uncorrelated) SF map is generated (Figure 2.3a). A filter is then applied on the uncorrelated SF map along x and y axes, and along the two diagonal directions. The used filter is a decaying exponential filter with coefficients determined from the measured correlation distance [54]. Compared to the uncorrelated SF map, the resulting correlated SF map in Figure 2.3b is less fluctuating.

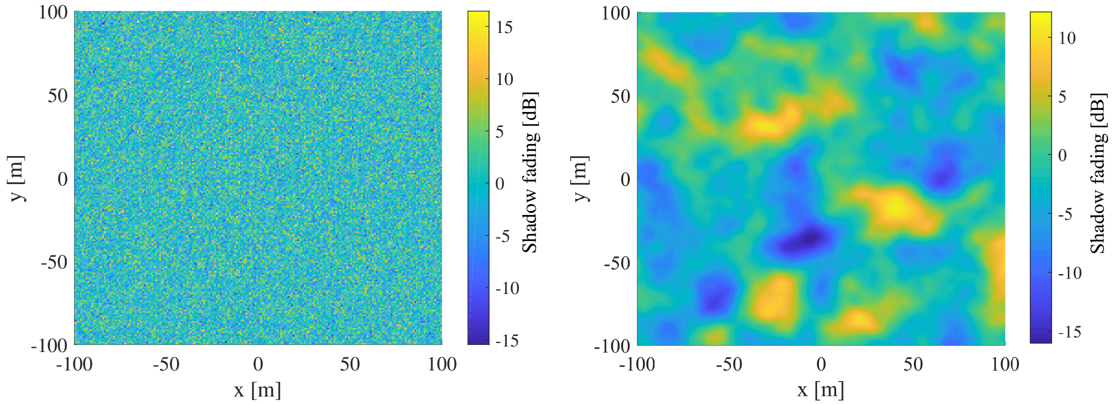

(a) Uncorrelated **(b)** Spatially correlated

Figure 2.3: Examples of uncorrelated and spatially correlated Gaussian shadow fading maps.

The cross-correlations are applied to the 2D maps by linear transformation using the measurement-based cross-correlation matrix. Note that, matrix square root is used instead of Cholesky decomposition for inter-parameter correlation. The map is then scaled by the mean and standard deviation value of the LSP. Finally, at a specific location of the Tx and the Rx, the value of LSP is extracted from the map.

In the next steps B, C, and D, the path delays, powers, and angles are only calculated for the initial positions, i.e., the beginning of each channel segment.

B. Calculation of initial path delays and angles

The initial delay values for the NLoS paths are randomly drawn from a single-sided exponential distribution with unit mean and unit standard deviation as in [40]

$$\tilde{\tau}_l = -\ln\left(\boldsymbol{X}_l^\tau\right), \tag{2.1}$$

where l is the path index and $\boldsymbol{X}_l^\tau \sim \mathcal{U}(0,1)$ is uniformly distributed and spatially correlated random variable that has values between 0 and 1. In this step, the LoS path is assigned with a zero delay.

In the next step, the two azimuth angles are initialized for each NLoS path. The angles are drawn randomly from a uniform distribution as

$$\tilde{\phi}_l = \boldsymbol{X}_l^{\phi} \sim \mathcal{U}\left(-\frac{\pi}{2}, \frac{\pi}{2}\right), \tag{2.2}$$

while the initial angles for the LoS path are set to 0. Under the assumption that all scatterers are located on the same horizontal plane with the Tx and the Rx antennas, the elevation angles of the paths have zero values.

C. Calculation of initial path powers
Based on the initial delays $\tilde{\tau}_l$, and initial azimuth angles of departure $\tilde{\phi}_l^d$ and arrival $\tilde{\phi}_l^a$, the initial path powers are calculated as [40]

$$\tilde{P}_l = \exp\{-\tilde{\tau}_l \cdot g^{\mathrm{DS}} - (\tilde{\phi}_l^d)^2 \cdot g^{\mathrm{ASD}} - (\tilde{\phi}_l^a)^2 \cdot g^{\mathrm{ASA}}\}, \tag{2.3}$$

where g^{DS},g^{ASD}, and g^{ASA} are the scaling coefficients used to ensure that the differences in the spreads are reflected in the powers. Differently from [40], the scaling factors are calculated based on their definitions in [15]. The scaling factor of the delay is defined as the ratio between the standard deviation of the path delays and the RMS delay spread. Similarly, the scaling factor of the angles is defined as the ratio between the standard deviation of the path angles and the angle spread.

D. Applying K-factor, delay spread and angle spreads
After initializing the path delays, angles, and powers, the actual values of the K-factor, delay spread and the two angular spreads (AS) are applied. By definition, the K-factor K is the ratio of the power of the LoS path to the sum of the power of all other paths. Therefore, the power of the LoS path is scaled as

$$\tilde{P}_1 = K \cdot \sum_{l=2}^{L} \tilde{P}_l \quad , \tag{2.4}$$

with L being the number of total paths. The path powers are then normalized to have a sum power equals one Watt as

$$P_l = \tilde{P}_l / \sum_{l=1}^{L} \tilde{P}_l \quad , \tag{2.5}$$

After that, the scaled path powers P_l from Equation (2.5) and the initial path delays $\tilde{\tau}_l$ from Equation (2.1) are used to calculate the initial delay spread as

$$\tilde{\sigma_\tau} = \sqrt{\frac{1}{P} \cdot \sum_{l=1}^{L} P_l \cdot (\tilde{\tau}_l)^2 - \left(\frac{1}{P} \cdot \sum_{l=1}^{L} P_l \cdot \tilde{\tau}_l\right)^2} \quad , \tag{2.6}$$

where P is the sum of all path powers. Next, by applying the initial delay spread $\tilde{\sigma_\tau}$ and the real value of the delay spread σ_τ from the correlated 2D map, the initial path delays from Equation (2.1) are scaled to obtain the a new path delays as

$$\tau_l = \tilde{\tau}_l \cdot \frac{\sigma_\tau}{\tilde{\sigma_\tau}} \quad . \tag{2.7}$$

By using these path delays together with the path powers from Equation (2.5) the correct delay spread can be achieved.

The angular spread is a measure of the spread of the path powers in angular domain. Similar to applying the delay spread, the initial angular spread is calculated by

$$\tilde{\sigma_\phi} = \sqrt{\frac{1}{P} \cdot \sum_{l=1}^{L} P_l \cdot \left(\tilde{\phi}_l\right)^2 - \left(\frac{1}{P} \cdot \sum_{l=1}^{L} P_l \cdot \tilde{\phi}_l\right)^2} \quad , \tag{2.8}$$

then the initial angles $\tilde{\phi}_l$ from Equation (2.2) are scaled using the correct angular spread σ_ϕ from the 2D correlated map as

$$\phi_l = \exp\left(j \cdot \tilde{\phi}_l \cdot s\right) \quad , \quad s = \frac{\sigma_\phi}{\tilde{\sigma_\phi}} \quad , \tag{2.9}$$

where the exp function is used to warp the angles around the unit circle.

As mentioned earlier, the azimuth angles of departure ϕ_1^d and arrival ϕ_1^a of the LoS path were set to 0. The correct angles are now calculated from the positions of the Tx and the Rx as

$$\phi_1^d = \arctan_2 \{y_r - y_t, x_r - x_t\} \ , \tag{2.10}$$

$$\phi_1^a = \phi_l^d + \pi \ . \tag{2.11}$$

Next, the path angles are converted from spherical to Cartesian coordinates by

$$\mathbf{c}_l = \begin{pmatrix} \cos\phi_l \\ \sin\phi_l \end{pmatrix} \ . \tag{2.12}$$

Then, the angles are rotated around the y-axis using a rotation matrix constructed from the LoS angles as

$$\hat{\mathbf{c}}_l = \begin{pmatrix} \cos\phi_1 & -\sin\phi_1 \\ \sin\phi_1 & \cos\phi_1 \end{pmatrix} \cdot \mathbf{c}_l \ . \tag{2.13}$$

In the last step, the final angles are obtained by converting $\hat{\mathbf{c}}_l$ back to spherical coordinates as

$$\phi_l = \arctan_2 \{\hat{c}_{l,x}, \hat{c}_{l,y}\} \ , \tag{2.14}$$

where $\arctan_2$ is the multi-valued inverse tangent. Note that, in the previous steps the elevation angles are ignored as they are set to 0.

E. Drifting of delays, angles and phases over each segment
Until now, the path delays, powers, and angles are calculated at the initial positions of the Tx and the Rx, i.e., at the beginning of each channel segment. When the Tx and the Rx move, the values of the path delays, power, and angles should be updated accordingly.

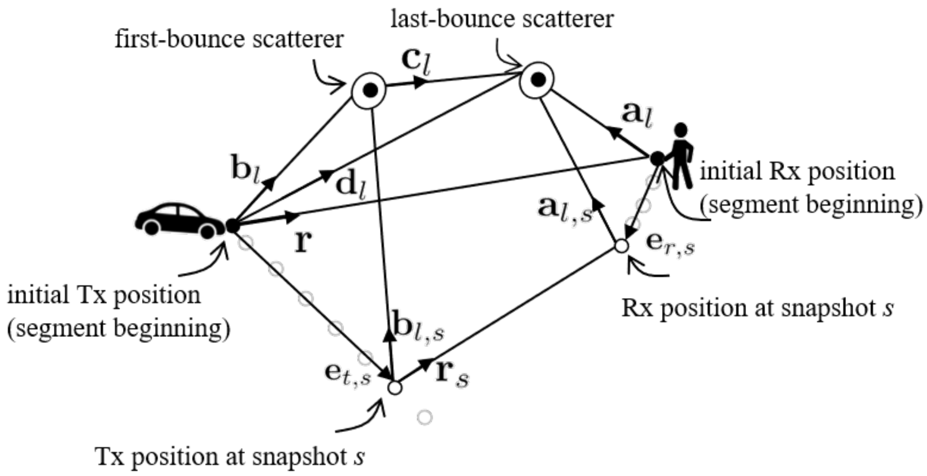

Figure 2.4: Illustration of the calculation of the scatterer positions and updates of the departure and arrival angles in the multi-bounce model.

A double-bounce model, illustrated in Figure 2.4, is considered in implementing the channel model. Therefore, the NLoS path consists of three parts. In the first part, the vector $\mathbf{b}_l$ points from the Tx antenna to the first-bounce scatterer (FBS). In the second part, the vector $\mathbf{c}_l$ points from the FBS to the last-bounce scatterer (LBS), and in the third part, the vector $\mathbf{a}_l$ points from the Rx antenna to the LBS. The total path length d_l is calculated from the path delay τ_l at the initial position, i.e., at the beginning of the segment. Hence, the total path length is

$$d_l = |\mathbf{b}_l| + |\mathbf{c}_l| + |\mathbf{a}_l| \quad . \tag{2.15}$$

Calculating the position of the FBS and the LBS requires the lengths of the vectors $\mathbf{a}_l$ and $\mathbf{b}_l$. One way to calculate $|\mathbf{a}_l|$ and $|\mathbf{b}_l|$ is by solving the following optimization problem with an objective to minimize the length $|\mathbf{c}_l|$ as follows

$$\begin{aligned} \underset{|\mathbf{a}_l|,|\mathbf{b}_l|}{\text{minimize}} \quad & |\mathbf{c}_l| = d_l - |\mathbf{b}_l| - |\mathbf{a}_l| \\ \text{subject to} \quad & \mathbf{r} = \hat{\mathbf{b}}_l \cdot |\mathbf{b}_l| + \hat{\mathbf{c}}_l \cdot |\mathbf{c}_l| - \hat{\mathbf{a}}_l \cdot |\mathbf{a}_l| \quad , \\ & |\mathbf{b}_l| \geq d_{\text{min}} \quad , \\ & |\mathbf{a}_l| \geq d_{\text{min}} \quad , \end{aligned} \tag{2.16}$$

where $d_{\min}$ is the minimum distance between the antenna and the nearest scatterers, and it is introduced in order to obtain realistic results. The unit-length vectors $\hat{\mathbf{b}}_l$ and $\hat{\mathbf{a}}_l$ are calculated from the departure and arrival angles. The ideal solution of the optimization problem is obtained when $|\mathbf{c}_l|$ becomes zero and then the double-bounce model turns into a single-bounce model. During a segment, the positions of the scatterers stay fixed and used to update the path delays and angles at each measurement snapshot.

At snapshot s, the arrival angle is obtained by converting back to spherical coordinates as

$$\phi^a_{l,s} = \arctan_2 \left\{ a_{l,s,y}, a_{l,s,x} \right\} \quad , \tag{2.17}$$

where $\mathbf{a}_{l,s}$ is a vector pointing from the Rx location at snapshot s to the LBS. Similarly, the departure angle is calculated at snapshot s by

$$\phi^d_{l,s} = \arctan_2 \left\{ b_{l,s,y}, b_{l,s,x} \right\} \quad , \tag{2.18}$$

where $\mathbf{b}_{l,s}$ is a vector pointing from the Tx location at snapshot s to the FBS.

The path phases $\psi_{l,s}$ and delays $\tau_{l,s}$ are calculated from the total path length at snapshot s as follows

$$d_{l,s} = |\mathbf{b}_{l,s}| + |\mathbf{c}_{l,s}| + |\mathbf{a}_{l,s}| \quad , \tag{2.19}$$

$$\psi_{l,s} = \frac{2\pi}{\lambda} \cdot (d_{l,s} \bmod \lambda) \quad . \tag{2.20}$$

$$\tau_{l,s} = \frac{d_{l,s}}{c} \quad , \tag{2.21}$$

with c being the speed of light. Finally, the LoS angles are updated as

$$\phi^d_{1,s} = \arctan_2 \left\{ r_{s,y}, r_{s,x} \right\} \quad , \tag{2.22}$$

$$\phi_{1,s}^{a} = \arctan_2 \left\{ -r_{s,y}, -r_{s,x} \right\} \quad , \tag{2.23}$$

where $\mathbf{r}_s$ is a vector pointing from the Tx location to the Rx location at snapshot s.

F. Application of path gain, shadow fading and K-factor

The path gain PG_s at snapshot s is derived from the path loss models introduced in Section 4.1. The SF is obtained from the 2D correlated map. The effective path gain is obtained by combining the PG and the SF as

$$\mathrm{PG}_s^{[\mathrm{eff}]} = \sqrt{10^{0.1\left(\mathrm{PG}_s^{[\mathrm{dB}]} + \mathrm{SF}_s^{[\mathrm{dB}]}\right)}} \quad . \tag{2.24}$$

As the KF is spatially correlated, it changes its value when the Tx and the Rx change their position. Previously, the path powers at the beginning of the segment P_l are scaled by the initial KF in Equations (2.4) and (2.5). However, since the KF changes, additional scaling factor for the path powers is required

$$K_{l,s}^{[\mathrm{scale}]} = \sqrt{1 + P_1 \left(\frac{K_s}{K_0} - 1 \right)} \cdot \begin{cases} \sqrt{\frac{K_s}{K_0}} & \text{for } l = 1; \\ 1 & \text{otherwise} \quad , \end{cases} \tag{2.25}$$

where K_0 is the KF at the beginning of the segment, K_s is the KF at snapshot s obtained from the 2D correlated map, and P_1 is the power of the LoS path calculated in Equation (2.4).

Finally, the complex-valued channel coefficients are calculated by

$$g_{l,s} = \mathrm{PG}_s^{[\mathrm{eff}]} \cdot K_{l,s}^{[\mathrm{scale}]} \cdot \sqrt{P_l} \cdot e^{-j\psi_{l,s}} \quad . \tag{2.26}$$

G. Transition between segments

In the previous steps, scatterers, channel coefficients, and path delays are created independently for each segment. Within each segment the scatterring clusters remain fixed, and the LSPs change slowly. When the Tx and the Rx move from one segment to another, different scatterers will be created, and the LSPs will change considerably. However, in reality, the physical channel does not change rapidly when moving between adjacent segments. In order to allow the Tx and the Rx move longer distances and maintain LSPs consistent, longer time evolution of the channel is required. The time evolution is achieved by the birth and death process of the scatterers. This process is modeled by merging the scatterers, i.e., the NLoS paths of adjacent segments.

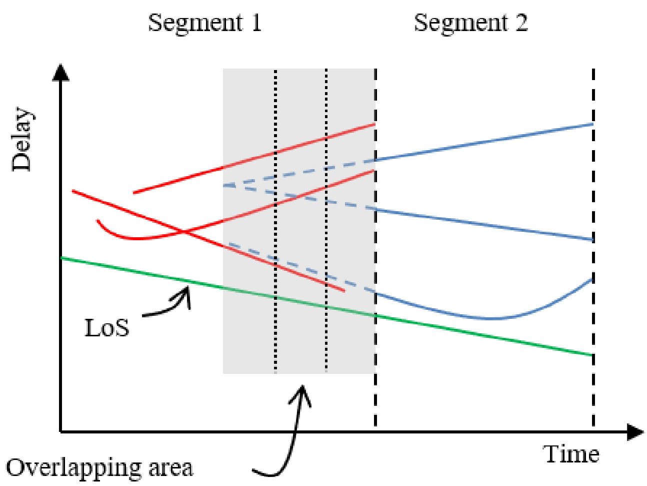

Figure 2.5: Illustration of the overlapping area used for calculating the transitions between segments.

As depicted in Figure 2.5, segment 2 is extended to overlap with segment 1. Within the overlap gray area, the extension of each scattering cluster, i.e., NLoS path is depicted with a dashed blue line. Therefore, the resulting scatterring clusters have lifetimes restricted to the combined length of two adjacent segments. The overlapping area is split into multiple parts equal to the number of the scatterers, e.g., three parts in this example. Within each overlapping part, one old NLoS path is paired with one new path. The selections of the two paths to be merged is done carefully based on their powers and delays. The selection criteria is minimizing the sudden fluctuation of the LSPs when moving between the two segments. Then, the power of the old path ramps down and the power of the new path ramps up. The power ramps are modeled by a squared sine function [40]

$$w^{[\mathrm{sin}]} = \sin^2\left(\frac{\pi}{2} \cdot w^{[\mathrm{lin}]}\right) \quad , \tag{2.27}$$

where $w^{[\mathrm{lin}]}$ is the linear ramp with range from 0 to 1, and $w^{[\mathrm{sin}]}$ is the sine-shaped ramp.

Finally, the proposed channel model is validated where the simulated channels, generated by the previous steps, and the measured channels are compared qualitatively in Chapter 6.

However, in order to estimate the model parameters and generate the channel coefficients, channel measurements need to be conducted. Extensive wideband channel measurements were performed in both open-field and urban environments. A detailed description of the two channel measurement campaigns is presented in the next chapter.

3

Wideband Channel Measurements

In order to obtain the parameters required for modeling the V2VRU communication channel, measurement data needs to be recorded. In this chapter, two measurement campaigns are described. The first campaign was executed in an open-field environment and presented in Section 3.1. The data collected in this campaign is later used to study the impact of several aspects on the propagation channel, e.g., Tx and Rx mobility, and LoS blockage by parked vehicles. In Section 3.2, the second measurement campaign in an urban environment considering the three most critical accident scenarios is described. The proposed channel model in this thesis is based on data collected during the measurements in the urban environment.

3.1 Open-field Measurements

To get detailed insight into the propagation of electromagnetic waves between vehicles and VRUs, we performed a measurement campaign in March 2017 at the airport in Oberpfaffenhofen near Munich. This location was chosen since it represents a controlled environment with open-sky visibility and a small number of far-located objects that could potentially reflect or scatter the electromagnetic waves. This location makes it possible to isolate and study the impact on the propagation channel caused by the different elements in the propagation environment as well as by the mobility of the Tx and Rx. For our measurement campaign, a collision scenario of a vehicle and a pedestrian was considered. Here, the test vehicle drove straight towards the pedestrian, which was approaching an imaginary collision point, from the right side. Both the pedestrian and the vehicle met at an imaginary collision point. Figure 3.1 displays the trajectory of both the test vehicle and the pedestrian on an aerial view of Google Maps. In our experiments, the test vehicle acted as the transmitter, while the pedestrian played the receiver role. The next two sections describe the measurement systems and scenarios.

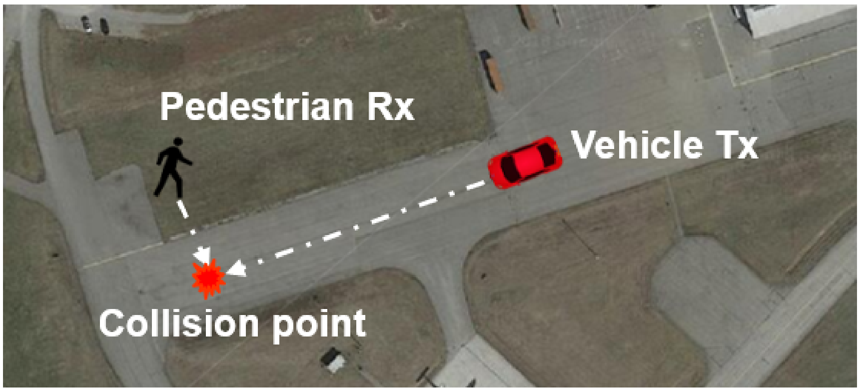

Figure 3.1: Aerial view of the measurement scenario showing the trajectories of the TX and the RX towards the imaginary collision point. (Google Maps 2017 Geobasis-de/BKG.)

3.1.1 Measurement Systems

The wideband channel sounding measurements were performed using the RUSK-DLR channel sounder at a center frequency $f_\mathrm{c} = 5.2\,\mathrm{GHz}$. The measurements bandwidth was $B = 120\,\mathrm{MHz}$, which corresponds to a delay resolution of $\Delta\tau = 8.33\,\mathrm{ns}$. The time-variant channel transfer function was recorded every $T_\mathrm{g} = 1.024\,\mathrm{ms}$, which allows to record a maximum absolute Doppler frequency of $f_\mathrm{d} = 488\,\mathrm{Hz}$. To fulfill the requirement of maximum Doppler frequency, the vehicle velocity was restricted to $v_\mathrm{max} = 11\,\mathrm{m/s}$. The length of each time-variant channel transfer function snapshot was $T_\mathrm{p} = 0.8\ \mu s$. The configuration parameters of the channel

Parameter	**Value**
RF center frequency f_c	5.2 GHz
Bandwidth B	120 MHz
Transmit power	37 dBm
Signal period T_p	0.8 µs
Time grid T_g	1.024 ms
Tx antenna	Onmi-directional (V-polarized), 8 dBi
Rx antenna	Omni-directional (V-polarized), 8 dBi and Dual-polarized array
Vehicle speed	11 m/s
Pedestrian speed	1.2 m/s

Table 3.1: Channel sounder parameters in the open-field measurements.

sounder are summarized in Table 3.1. The transmit antenna was positioned at the front side of the roof of the vehicle at a height of $h_{\mathrm{Tx}} = 1.9\,\mathrm{m}$ above the ground. The receive antenna was placed either on a tripod or carried by a pedestrian at heights of $h_{\mathrm{Rx}} = 1.1\,\mathrm{m}$ or $1.3\,\mathrm{m}$.

In order to synchronize the transmitter and the receiver, two rubidium clocks were used. However, during post processing, it was found that a clock offset had been accumulated during the time of the experiments. In order to compensate this offset drift, the relative position of the Tx and Rx was used to calculate the difference between the propagation delay of the LoS path in the CIR and the true propagation delay. The drift values were calculated in all experiments. It was found that the offset increased linearly during the measurements day. Based on the linear increase, the value of the offset for each measurement snapshot was calculated and compensated. GNSS was used as a ground truth for the position of both transmit and receive antennas. The vehicle, the tripod and the pedestrian were equipped with a Topcon Legacy E+ L1/L2 GLONASS/GPS receiver. A geodetic-grade GNSS antenna was placed on the roof of the vehicle, on one end of the tripod and attached to the helmet of the pedestrian (see Figure 3.2). The 10 Hz recorded GPS and GLONASS raw data were post processed to find a carrier-fixed solution with centimeter-level accuracy (1σ). The displacement between GNSS and the communication antennas at Rx and Tx was considered when computing the exact position for the propagation analysis with the channel sounder and the ITS-G5 system. To determine the location of the parked vehicles acting as obstruction to the LoS, an LD-MRS multi-layer laser scanner from Sick was attached at the front bumper of the test vehicle and a ublox LEA 4T GPS receiver was employed. In post-processing, the laser point cloud was transformed from a vehicle coordinate frame to a global coordinate frame using the code-solution from the GPS receiver.

3.1.2 Measurement Scenarios

The test vehicle in which the transmitter was located was a Mercedes G400 (Figure 3.2a). After an initial acceleration phase, the vehicle moved from 100 m distance towards the collision point with constant speed of 11 m/s . To study the influence of movement and body shadowing of the pedestrian, we performed tests with a static and with a moving pedestrian. In the static case, the pedestrian (Figure 3.2b) was replaced by a tripod (Figure 3.2c). The tripod was placed at three different positions with different distances (12 m, 7 m and 2 m) from the collision point. In the moving case, the pedestrian was approaching the collision point from 12 m distance at a speed of approximately 1.2 m/s.

(a) Tx Test Vehicle

(b) Rx Pedestrian

(c) Rx Tripod

(d) Rx Antenna Array

Figure 3.2: Transmitter (Tx) and receiver (Rx) involved in the open-field measurement campaign.

To study the impact of the parked vehicles at the roadside on the propagation channel especially the blockage of the LoS path, a row of cars and vans were parked in a line parallel to the trajectory of the test vehicle. Five different constellations using one to six vehicles of different size and shape were tested. Additionally, one of the cars was used to study the effect on the communication channel of an additional reflection coming from the opposite roadside, once, from a parked car and, once, from a moving car. Further, to study the effect of the shadowing of a crowd of people surrounding the pedestrian, the pedestrian was surrounded by four test persons. In addition, a circular antenna array with 2×16 elements was used (See Figure 3.2d) in order to detect the angle of arrival of different multipath components and study scattering phenomena.

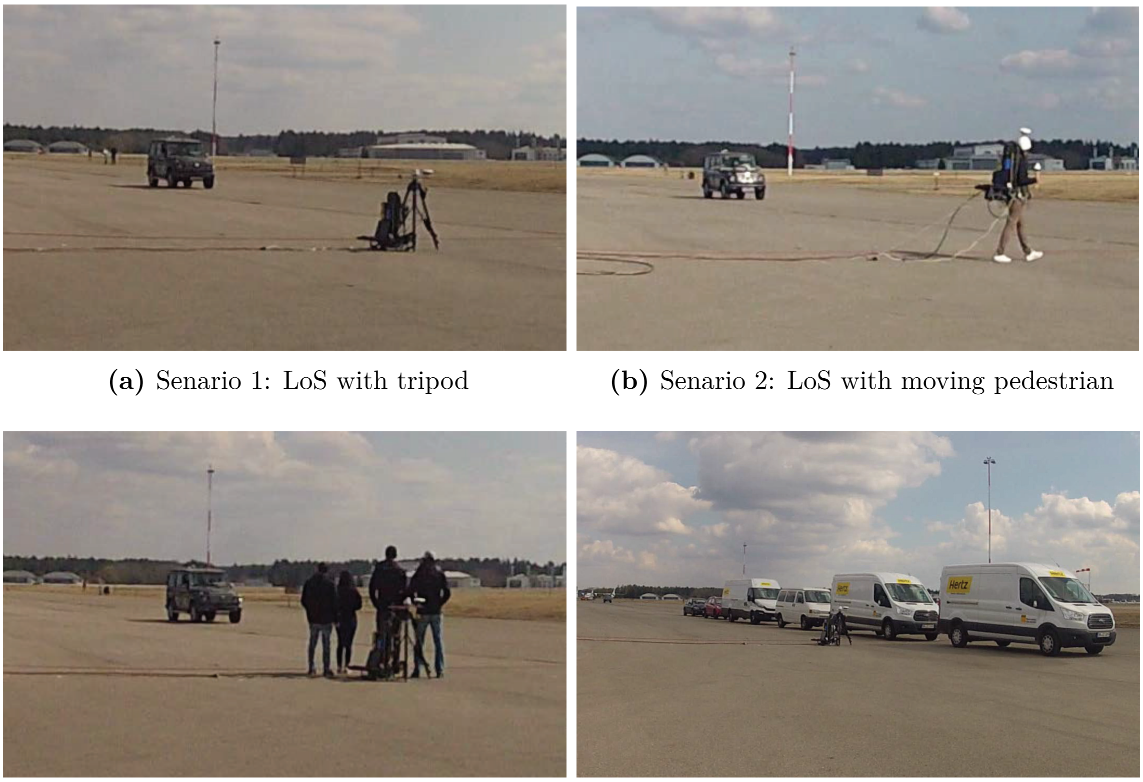

(a) Senario 1: LoS with tripod

(b) Senario 2: LoS with moving pedestrian

(c) Senario 3: Shadowing crowd

(d) Senario 4: NLoS with static tripod

Figure 3.3: Four measurement scenarios in the open-field environment addressed in this thesis.

All in all, a total set of 30 experiments with different combinations of moving/static pedestrian, LoS/NLoS, different combinations of parked vehicles and with/without crowd shadowing were performed. In this thesis, the following four scenarios will be discussed in details:

- Scenario 1 (Figure 3.3a): LoS condition with static tripod
- Scenario 2 (Figure 3.3b): LoS condition with moving pedestrian
- Scenario 3 (Figure 3.3c): LoS condition with shadowing crowd

- Scenario 4 (Figure 3.3d): NLoS condition with static tripod

3.2 Urban Measurements

Channel measurements were conducted in October 2018 at three different streets in the city of Germering near Munich. In this thesis, the channel measurements in Göthestraße will be analyzed (see Figure 3.4) where $3-6$ story buildings lined up along the street on one side, while separated by green area on the other side. The street consists of one lane for each direction with parked cars on both sides. It is 12 m wide, with 3 m wide sidewalks.

Figure 3.4: Aerial view of the measurement scenarios in the urban environment showing the trajectory of the vehicle (in blue), and the trajectory of the cyclist/pedestrian (in green with the number of the scenario) towards the imaginary collision point. (Google Earth 2018 Geobasis-DE/BKG.).

3.2.1 Measurement Systems

The V2VRU measurement campaign was carried out using the RUSK-DLR channel sounder. The measurement signals were transmitted at a carrier frequency of f_c = 5.2 GHz, which is close to the 5.9 GHz ITS band. The bandwidth was B = 120 MHz, and thus providing a delay resolution of $\Delta\tau$ = 8.33 ns. During the measurements, the time-variant channel transfer function was recorded every T_g = 1.024 ms allowing to resolve a maximum Doppler shift of $f_{\mathrm{d\,max}}$ = 488 Hz. The main measurement parameters can be found in Table 3.2. In order to record the position of the Tx and the Rx antennas, GNSS receivers were used. Two lidar sensors from Velodyne were mounted on the test vehicle and near the cyclist/pedestrian to provide 3-dimensional high resolution images of the environment. The antennas positions on Tx and Rx side can be seen in Figure 3.5.

Figure 3.5: Antennas positions on the pedestrian, the cyclist, and the test vehicle.

3.2.2 Measurement Scenarios

Figure 3.4 displays the trajectories of the test vehicle, the cyclist, and the pedestrian on an aerial view for the accidents scenarios. Three critical accident scenarios between vehicle and VRU were considered:

- Scenario 1 (Figure 3.6a): The vehicle is moving 100 m with an average velocity of 5 – 11 m/s towards the intersection then turning right while the cyclist is moving 10 m with an average speed of 1.5 m/s toward the imaginary collision

Parameter	**Value**
RF center frequency f_c	5.2 GHz
Bandwidth B	120 MHz
Transmit power P_T	37 dBm
Signal period T_p	3.2 µs
Time grid T_g	1.024 ms
Tx antenna	Onmi-directional (V-polarized), 8 dBi
Rx antenna	Omni-directional (V-polarized), 8 dBi
Vehicle speed	5 −11 m/s
Cyclist speed	1.5 m/s
Pedestrian speed	1 m/s

Table 3.2: Channel sounder parameters in the urban measurements.

point from the right. This scenario accounts for 42 % of the total cyclist accidents as reported by the general association of the German insurance industry (GDV) [3]. In this scenario, the LoS between the vehicle and the cyclist is initially blocked by buildings, then it becomes obstructed by parked vehicles as both the vehicle and the cyclist are approaching the collision point. In this scenario, a total of 10 measurement runs were conducted.

- Scenario 2 (Figure 3.6b): In contrast to Scenario 1, the cyclist is moving parallel to the vehicle toward the collision point at the intersection. This scenario is less critical than Scenario 1 as it accounts for only 11 % of the total cyclist accidents [3]. In this scenario, the LoS between the vehicle and the cyclist repeatedly transits between LoS and OLoS situations due to obstruction by parked vehicles. In this scenario, a total of 2 measurement runs were conducted.

- Scenario 3 (Figure 3.6c): The pedestrian is crossing the street with an average speed of 1 m/s while the vehicle is approaching from the left. In this scenario, the visibility between the vehicle and the pedestrian is partially or completely blocked by the parked vehicles. According to the national highway traffic safety administration (NHTSA) [2], this scenario is the most critical accident scenario for pedestrians and it accounts for 26 % of all pedestrian accidents. In this scenario, a total of 9 measurement runs were conducted.

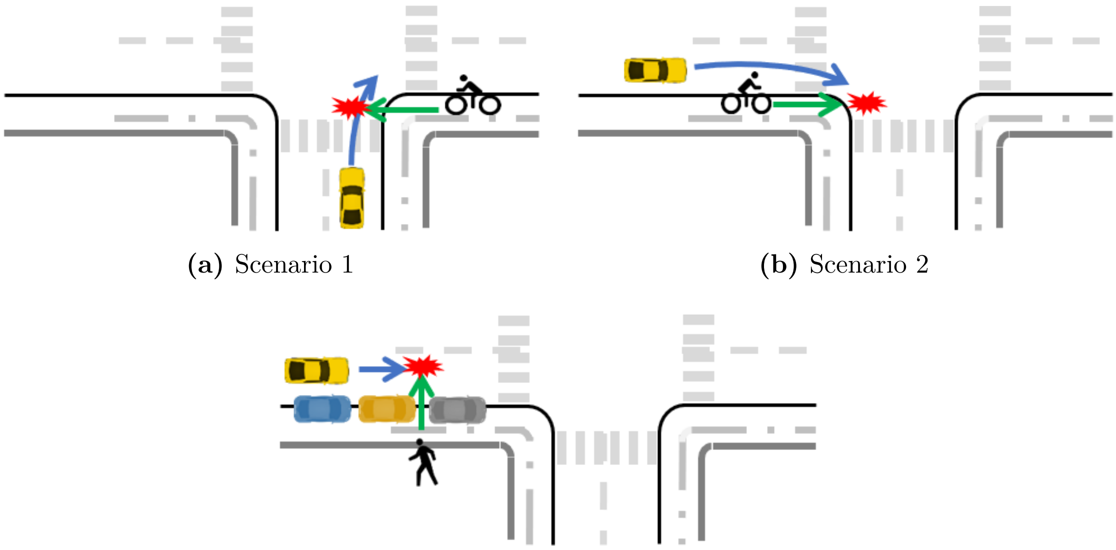

(a) Scenario 1

(b) Scenario 2

(c) Scenario 3

Figure 3.6: Illustrations of the accident scenarios in urban environment. The data collected in these scenarios are used to model the V2VRU channel.

4

Channel Characteristics and General Modeling Aspects

This chapter addresses several aspects of channel modeling. In Section 4.1, path loss models for open-field and urban channels are proposed. Moreover, due to the spatial correlation of the shadow fading, consecutive packet losses can occur, which lead to degradation in the communication performance. Therefore, the spatial correlation of the shadow fading in the open-field is analyzed and models are proposed. To study the propagation loss due to the obstruction of the LoS by parked vehicles, a 3D ray tracing tool has been developed in Section 4.3. The tool detects the diffraction edges and calculates the Fresnel-Kirchoff parameter that is used to calculate the knife-edge diffraction loss.

Due to the non-stationarity of the V2VRU channel, the channel is characterized by dividing it into regions where the WSSUS assumption holds and then the LSPs are estimated in each individual region. In Section 4.4, the non-stationarity of the V2VRU channel is analyzed by estimating the GLSF and its collinearity based on the channel measurement data in the urban environment, and the estimated stationarity distance is presented.

In Section 4.5, the multipath parameters are estimated using the KEST algorithm. A novel method is proposed to extract SMCs from the estimated CIR based on the density of their neighboring MPCs. This extraction allows for further characterization of these SMCs. Furthermore, a simple but effective algorithm for multipath tracking based on the differences in delay and magnitude between SMCs is presented. Based on the previous step, in Section 4.6, the SMCs parameters are employed to localize the physical scatterers in the propagation environment using a joint delay-Doppler estimation algorithm. The estimated positions of the scatterers are then used to estimate the AoD and AoA. In Section 4.7, the diffuse multipath is extracted in order to calculate its contribution to the total received power.

4.1 Path Loss Model

In this section, path loss models for the measured scenarios in the open-field and urban environments are presented.

The CIR can be expressed mathematically as a sum of $N(t)$ Dirac impulses [55]:

$$h(t,\tau) = \sum_{i=0}^{N(t)-1} \alpha_i(t) \cdot \delta_i(\tau - \tau_i(t)), \tag{4.1}$$

where $\alpha_i(t)$ and $\tau_i(t)$ are the complex amplitude and delay of the i-th MPC at time step t and $\delta(\cdot)$ is the Dirac function. The instantaneous power delay profile (PDP) is then calculated by:

$$P(t,\tau) = |h(t,\tau)|^2, \tag{4.2}$$

where $|h(t,\tau)| = \sqrt{(I_h(t,\tau))^2 + (Q_h(t,\tau))^2}$, where $I_h(t,\tau)$ and $Q_h(t,\tau)$ are the real part and the imaginary part of the complex amplitude $\alpha_i(t)$ [56]. Next, the average PDP (APDP) $\overline{P(t,\tau)}$ is obtained by applying a sliding window[1] on the PDP with a length corresponding to a traveled distance of $l_w = 10\,\lambda$ which is equivalent to $N_{\text{av}} = \frac{l_w}{v \cdot T_{\text{g}}} = 54$ PDPs in the open-field measurements and 169 PDPs in the urban measurements, where $v = 11\,\text{m/s}$ is the average velocity of the transmitter in open-

[1] Different window sizes are tested, a window size of $10\,\lambda$ is found to best fit the data. It provides a sufficient number of samples to accurately extract the small-scale fading.

field measurements and it is equal to 7 m/s in the urban measurements, T_g =1.024 ms is the time grid, and λ is the wavelength. Within each segment of 10 λ, the channel is assumed to be quasi-stationary.

Based on the APDP, the received power $P_r(t)$ can be calculated as:

$$P_\mathrm{r}(t) = \sum_{i=0}^{N(t)-1} \overline{P(t,\tau_i)}\ , \tag{4.3}$$

where $N(t)$ is the number of the APDP samples at time t. Thereafter, the path loss P_L is obtained by:

$$P_\mathrm{L} = \frac{P_\mathrm{t} G_\mathrm{Tx} G_\mathrm{Rx}}{P_\mathrm{r}}, \tag{4.4}$$

where P_t, P_r, G_Tx, and G_Rx are the transmitted power, received power, Tx antenna gain and Rx antenna gain, respectively.

The path loss can be expressed in logarithmic scale as a sum of two components, namely, the distance-dependent path loss model and the SF:

$$P_\mathrm{L} = \underbrace{\overline{P_\mathrm{L}(d)}}_{\text{path loss model}} + \underbrace{X}_{\text{shadow fading}} . \tag{4.5}$$

The SF is caused by shadowing processes and leads to a change in the local mean of the path loss over relatively large distances. Whereas the small-scale fading is the variation due to the superposition of multiple propagation paths. It leads to power variations when moving over relatively short distances in the order of the signal wavelength. The small-scale fading is extracted by applying the aforementioned sliding window.

The log-distance path loss model is used to predict the propagation loss in different environments. The average large-scale path loss is a function of the separation distance between the Tx and Rx as expressed by

$$\overline{P_\mathrm{L}(d)} = P_\mathrm{L}(d_0) + 10n\log_{10}(d/d_0), \tag{4.6}$$

where $P_\mathrm{L}(d)$ denotes the path loss in dB at a distance d between Tx and Rx, $P_\mathrm{L}(d_0)$ is the path loss at a reference distance d_0, and n is the path loss exponent. Using linear regression analysis, the path loss exponent n that minimizes the difference between the measured and modeled values is determined.

In scenarios where the LoS becomes partially or completely obstructed, it has been found that the measured path loss can be more accurately represented by a dual slope log-distance path loss model. The dual slope model is given by

$$\overline{P_{\mathrm{L}}(d)} = \begin{cases} P_{\mathrm{L}}(d_0) + 10n_1\log_{10}(d/d_0), & \text{if } d \leq d_{\mathrm{c}} \\ P_{\mathrm{L}}(d_0) + 10n_1\log_{10}(d_c/d_0) + 10n_2\log_{10}(d/d_c), & \text{if } d > d_{\mathrm{c}}\ . \end{cases} \tag{4.7}$$

where $P_{\mathrm{L}}(d_0)$ is the path loss at the reference distance d_0, and d_c is the breakpoint distance at which the second slope begins. n_1 and n_2 are the path loss exponents of the first and second slope, respectively, and they provide an indication of how the signal attenuates with the Tx-Rx separation distance. The breakpoint distance corresponds to the Tx-Rx separation distance at which the communication link state changes, i.e., from LoS to OLoS or from OLoS to NLoS. The model fitting parameters were tuned by minimizing the squared error between the measured path loss and the model (i.e., least squares criteria).

Another path loss model, widely used in literature to model the LoS channel, is the two-ray path loss model [30]. This model considers not only the direct propagation path but also the reflected one from the ground. The received power according to the two-ray path loss at a Tx-Rx separation distance d is given by

$$\overline{P_{\mathrm{L}}(d)} = 20\log_{10}(\frac{4\pi}{\lambda}) - 20\log_{10}\left|\frac{e^{-jkd_{\mathrm{LoS}}}}{d_{\mathrm{LoS}}} + \Gamma(\theta)\frac{e^{-jkd_{\mathrm{gr}}}}{d_{\mathrm{gr}}}\right|, \tag{4.8}$$

where the parameter $k = 2\pi/\lambda$ is the wavenumber at the center frequency f_{c} and λ is the wavelength. $d_{\mathrm{LoS}} = \sqrt{d^2 + (h_{\mathrm{Tx}} - h_{\mathrm{Rx}})^2}$ and $d_{\mathrm{gr}} = \sqrt{d^2 + (h_{\mathrm{Tx}} + h_{\mathrm{Rx}})^2}$ are the propagation distances for the LoS and the ground reflection. h_{Tx} and h_{Rx} are the heights of the Tx antenna and the Rx antenna, respectively. $\Gamma(\theta)$ is the ground reflection coefficient for the reflection angle θ and is calculated for vertical polarization by

$$\Gamma(\theta) = \frac{\epsilon_{\mathrm{r}}\sin(\theta) + \sqrt{\epsilon_{\mathrm{r}} - \cos^2(\theta)}}{\epsilon_{\mathrm{r}}\sin(\theta) - \sqrt{\epsilon_{\mathrm{r}} - \cos^2(\theta)}} \tag{4.9}$$

where ϵ_{r} is the relative permittivity of the ground and $\theta = \tan^{-1}(\frac{h_{\mathrm{Tx}}+h_{\mathrm{Rx}}}{d})$.

Figure 4.1 shows the measured path loss and the proposed path loss models for the open-field measured scenarios described in Section 3.1.2. Note that the free space path loss model has $n = 2$ and $P_{\mathrm{L}}(d_0) = 46.77\,\mathrm{dB}$, where $d_0 = 1$, and is plotted for comparison. Table 4.1 summarizes the results of fitting the measured path loss linearly to the proposed log-distance models.

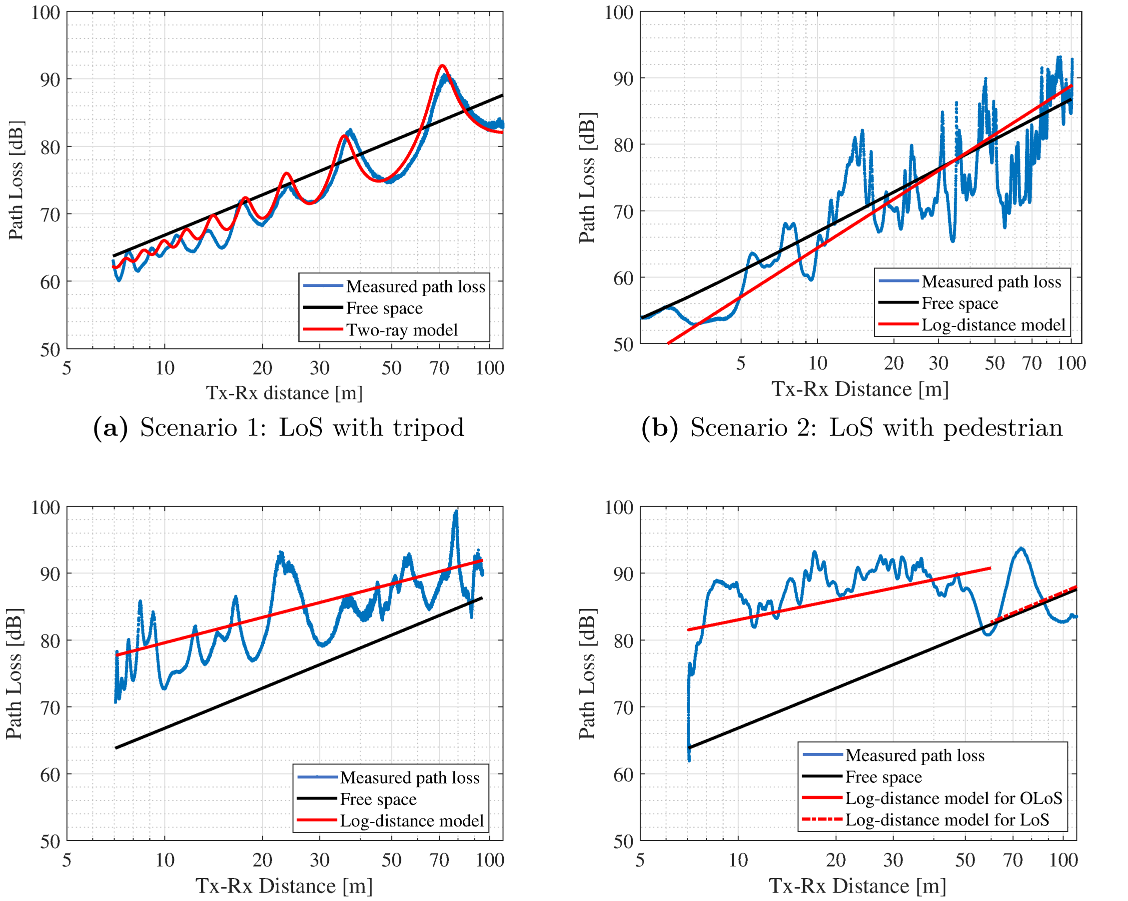

(a) Scenario 1: LoS with tripod

(b) Scenario 2: LoS with pedestrian

(c) Scenario 3: shadowing crowd

(d) Scenario 4: NLoS

Figure 4.1: The measured and modeled path loss in the open-field environment.

In Scenario 1, the receiver antenna is fixed on a static tripod at height $h_{\mathrm{Tx}} = 1.1\,\mathrm{m}$. The tripod was 7 m away from the collision point (see Figure 3.3a). Figure 4.1a shows the obtained path loss versus the distance between the Tx and Rx. A typical two-ray effect, i.e., the LoS path and the ground reflected path, can be noticed which causes a power variation slowly over the distance between the Tx and Rx. With an estimated relative permittivity $\epsilon_{\mathrm{r}} = 1.05$ for the ground and standard deviation $\sigma = 0.68$ dB, the two-ray model provides a good fit to the measurement data even at short distance between the Tx and Rx.

In Scenario 2, the receive antenna was mounted with a moving pedestrian (see Figure 3.3b). Figure 4.1b shows the corresponding path loss versus the distance between the Tx and Rx. The two-ray model does not fit to the measurement data and, therefore, is not visualized. A rapid fluctuation of the measured path loss can be seen. This fluctuation is probably the result of the MPC originated by the human body. Further, the moving human body also results in dynamic antenna altitude and position. The estimated log-distance path loss exponent n is 2.44, which is larger than the n for the free space propagation.

In Scenario 3 (see Figure 3.3c), the shadowing influence of neighboring pedestrians on the received power is evaluated. Figure 4.1c shows the obtained path loss from the measurement. Due to the shadowing effect caused by the crowd around the Rx, the two-ray effect can not be clearly observed. In general, the measured path loss value is $5-10$ dB larger than the LoS case. The estimated path loss exponent n is 1.26, which is smaller than the n in Scenario 1. It indicates that the power in Scenario 3 decreases slower than in Scenario 1, however, with more shadowing caused by the pedestrians, i.e., a higher value of $P_{\mathrm{L}}(d_0) = 67$ dB. A similar finding is also reported in [57].

In Scenario 4, the receive antenna was stationary next to a convoy consisting of 6 parked vehicles with different sizes. Adjacent parked vehicles are separated with a gap of 1 m (see Figure 3.3d). During the movement of the Tx toward the Rx, the LoS is partially or completely obstructed. Figure 4.1d shows the measurement result for the path loss values. The measurement samples between 60 and 100 m are obtained under LoS condition without obstruction by the parked vehicles. It can be seen that the path loss value is similar to the LoS condition in Figure 4.1a between 60 and 100 m.

It can be noticed that compared to the free space path loss model, the obstruction of the LoS causes an extra loss between $10-20$ dB depending of the size of the

	n	$P_\mathrm{L}(d_0)$ [dB]	σ [dB]
Scenario 2	2.44	40	3.20
Scenario 3	1.26	67	5.47
Scenario 4 - LoS	2	46.77	4.35
Scenario 4 - OLoS	1	73	4.35

Table 4.1: Log-distance path loss model parameters in the open-field environment.

parked vehicle. For Tx-Rx distances between 7 m and 60 m the path loss experiences large values due to obstruction by the parked vehicles. Therefore, the path loss model is divided into LoS and OLoS parts. Each part has a different path loss exponent n and standard deviation σ. The parameters of the log-distance path loss model for both the LoS scenario and the LoS part of the NLoS scenario are similar to those of the free space model. On the other hand, the path loss exponent $n = 1$ during the obstruction of the LoS indicates that the power decreases slower than during LoS situation, however, with more shadowing caused by the parked vehicles, i.e., a higher value of $P_\mathrm{L}(d_0) = 73\,\mathrm{dB}$. A similar inverse proportional relation between n and $P_\mathrm{L}(d_0)$ is reported in [22]. The diffraction loss due to blockage of the LoS by the parked vehicles is investigated and modeled in the next section.

Next, path loss models for the measured path loss in the urban environment are provided. Figure 4.2 shows the measured path loss variations with the Tx-Rx distance and the proposed path loss models for the measured scenarios in the urban environment. Table 4.2 summarizes the results of fitting the measured path loss linearly to the proposed models.

In Scenario 1 (Figure 4.2a), due to movement of the vehicle (Tx) and the cyclist (Rx), the Tx-Rx link transits between NLoS, OLoS, and LoS. A NLoS situation arises due the blockage of the LoS by buildings between 100 and 32 m. Due to the obstruction, an extra loss up to 25 dB is experienced when compared to the free space path loss. Between 32 m and 15 m the LoS becomes obstructed by the parked vehicles which causes a diffraction loss of $5-15\,\mathrm{dB}$. A LoS state appears only shortly before the collision between the vehicle and the cyclist at the intersection. When

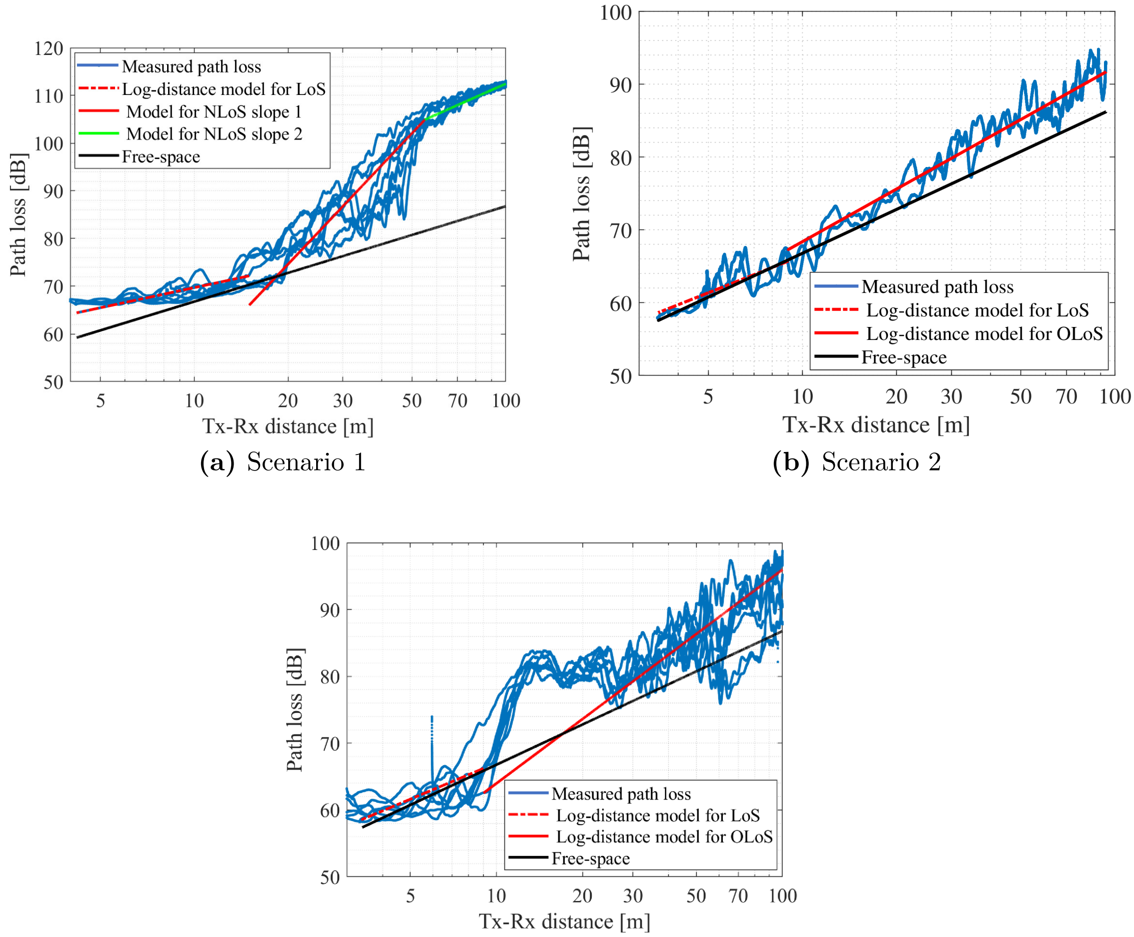

(a) Scenario 1

(b) Scenario 2

(c) Scenario 3

Figure 4.2: The measured and modeled path loss in the urban environment.

compared to the free space path loss, a difference up to 7 dB can be noticed. This difference is partially due to the ground and self-body reflection. The measured path loss is found to be more accurately represented by a dual-slope log-distance path loss model given by Equation (4.7) for distances between 15 and 100 m with a breaking distance of 55 m. Path loss exponents of 6.9 and 2.9 for the first and the second slopes, respectively, are proposed. The path loss during LoS is modeled by a single slope log-distance model with an estimated path loss exponent of 1.4.

In Figure 4.2b, the path loss for Scenario 2 is modeled by two single slopes log-distance models. The first slope is for distances up to 9 m and covers the LoS area prior to the collision with estimated path loss exponent of 1.7 . For distances between 9 m and 100 m, the link between the vehicle and the cyclist becomes partially obstructed by parked vehicles which causes a diffraction loss up to 5 dB. The estimated path loss exponent equals 2.4, which is slightly above the one of the free space model.

In Scenario 3 (Figure 4.2c), the estimated path loss exponent for LoS area, i.e., up to 9 m, does not vary much from Scenario 2 with an exponent of 1.8 . However, the path loss experiences a sudden increase by 15 dB at around Tx-Rx distance of 10 m due to the obstruction of the LoS by a large vehicle. The path loss between 9 m and 100 m shows rapid variations in the order of 5 to 15 dB due to obstruction of the LoS by parked vehicles with an estimated path loss exponent of 3.2.

	LoS			**OLoS \NLoS**				
	Slope 1			**Slope 1**			**Slope 2**	
	$PL(d_0)$ [dB]	n	σ [dB]	$PL(d_0)$	n	σ	n	σ
Scenario 1	55.70	1.40	1.90	-15.16	6.90	3.80	2.90	3.46
Scenario 2	49.46	1.70	1.53	44.37	2.40	1.88		
Scenario 3	49	1.80	3.40	31.97	3.20	5.79		

Table 4.2: Log-distance path loss model parameters for urban scenarios.

4.2 Spatial Correlation of Shadow Fading in Open-field

The SF is strongly dependent on the environment, i.e., it varies from one area to another. Movements of the vehicle, the VRU, and the surrounding scatterers result in a dynamic environment. When the receiver moves to a shadowed area, i.e., the LoS becomes obstructed, it remains obstructed for some time or corresponding traveled distance. This implies that the shadowing is spatially correlated. Due to this underlying correlation, consecutive packet losses can occur during this time interval. As a result, communication performance will be degraded. Therefore, accurate modeling of the spatial correlation of the SF is important to design a reliable V2VRU communication system. Spatial correlation models are used in simulations to generate realizations of the SF process with the desired correlation. Different techniques for generating the SF based on the correlation models can be found in literature, such as [58] and [59].

The SF is extracted by subtracting the path loss model from the measured path loss after removing the impact of the small-scale fading by averaging the measured path loss using a sliding window of length $l_w = 10\,\lambda$. This window size is found to provide a sufficient number of samples to accurately extract the small-scale fading and calculate the correlation distance of the SF. Figure 4.3 shows the extraction of the SF from the measured path loss for Scenario 4 in the open-field environment, i.e., the NLoS scenario, using a window size of $10\,\lambda$.

In what follows, the spatial correlation of the SF for Scenario 1 and Scenario 4 of the open-field environment is investigated. Scenario 4 is further divided into a LoS part (parked vehicles are not obstructing the LoS) and an OLoS part (six parked vehicles are obstructing the LoS). The LoS part covers the Tx-Rx distance larger than 60 m, while the OLoS part covers the Tx-Rx distance less than 60 m. The following analysis is published in [16].

The spatial correlation can be obtained by the autocorrelation of the SF as:

$$r(\Delta d) = \mathrm{E}\left[X(d)X(d+\Delta d)\right], \tag{4.10}$$

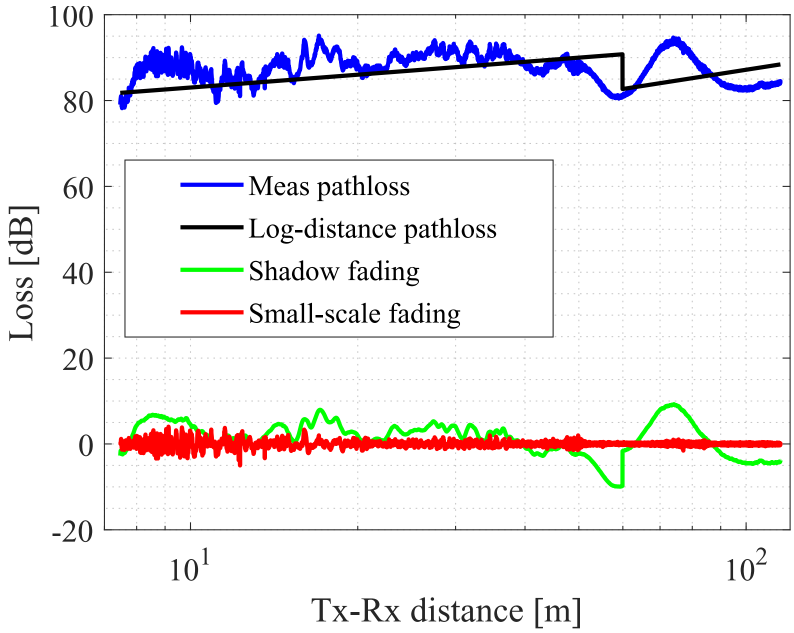

Figure 4.3: An example of the extraction of the SF from the measured path loss for Scenario 4 in the open-field using a window size of 10λ.

where d is the distance between the Tx and the Rx, and Δd is the distance between two observed positions. $\mathrm{E}[\cdot]$ denotes the expected value of $[\cdot]$. In principle, the estimation of the autocorrelation function of any random process requires having a large set of samples at every observation time t to calculate the statistical average or the so called ensemble average. By assuming ergodicity of a random process, i.e., the sample average over time t for one realization (measurement run) of the random process converges to the ensemble average as the length of the realizations tends to infinity, the autocorrelation function can be estimated by using samples collected from one measurement run.

A random process is called WSS when the mean and the autocorrelation do not vary with time. The SF can be assumed WSS since the distance-dependent part is subtracted from the measured path loss when extracting the SF [60]. However, to prove the WSS assumption, the SF is put under test, namely, the modified reverse arrangement test (MRA) [61]. The MRA test is performed by dividing the SF sample record into N_s equal segments and calculating the square mean value in each segment $(x_1^2, x_2^2, x_3^2, \dots x_{Ns}^2)$. In a stationary random process the square mean values of adjacent segments are independent [61] and any time trend will result in non-stationarity. The test checks if the examined random process has a time trend by calculating how many times, starting with x_1^2, that each subsequent square mean value $(x_2^2, x_3^2, \dots x_{Ns}^2)$ is less than x_1^2. This step is repeated with each square mean value. Each inequality is called a 'reverse arrangement'. Figure 4.4 shows an example of the mean square values of the SF for N_s =10 segments and N_s =20 segments which correspond to distance interval of 5 m and 10 m for both Scenario 1 and Scenario 4, respectively. It can be seen that the changes in the mean value do not follow a specific trend. The total number of the reverse arrangements A is then used to calculate the total score as

$$z = \frac{A - \left[\frac{N_s(N_s-1)}{4}\right]}{\sqrt{\frac{2N_s^3+3N_s^2-5N_s}{72}}}. \tag{4.11}$$

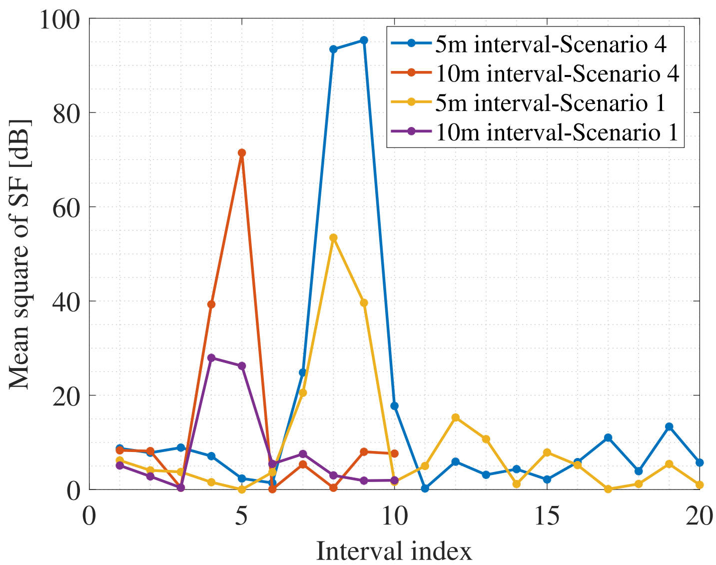

Figure 4.4: Mean square value of the SF calculated within intervals of 5 m and 10 m for Scenario 1 and Scenario 4 in open-field.

The stationarity hypothesis is then verified with 5 % significance if the absolute value of the total score $-1.96 \leq z \leq 1.96$. Figure 4.5 shows the z score of the

MRA test for 60 different number of intervals N_s. It can be seen that both scenarios as well as the two parts of the Scenario 4 pass the stationarity test.

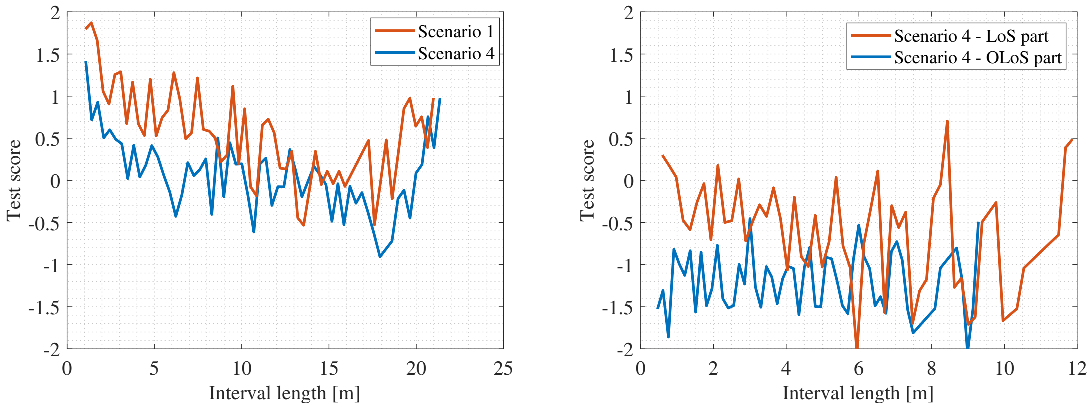

(a) Scenario 1 and Scenario 4 **(b)** LoS and OLoS parts of Scenario 4

Figure 4.5: Score of the MRA stationarity test.

The autocorrelation functions is estimated from the measurement data using Equation (4.10). Figure 4.6 shows the estimated autocorrelation functions with respect to Δd.

The correlation distance d_c is defined as the value of Δd at which the value of the normalized autocorrelation function drops to e^{-1}. The correlation distance is scenario-dependent and indicates how fast the SF is changing over distance. The SF can be assumed to stay constant within the correlation distance d_c. Applying this assumption, the SF can be considered as a block fading which leads to a simplification of modeling the SF in simulators.

Figure 4.6a illustrates the spatial autocorrelation function of the SF for both scenarios. It can be seen that the correlation distance in Scenario 1 is 7.2 m. Blocking the LoS by parked vehicles in Scenario 4 leads to a larger correlation distance of 10.4 m. This implies that compared to the LoS, the SF in the NLoS experiences less variation, i.e., similar diffraction loss, when the LoS is obstructed by the same object. The oscillation pattern in both scenarios can be explained by the constructive and destructive interference, which is due to the superposition of the direct and the ground-reflected rays, (see Figure 4.1a and Figure 4.1d).

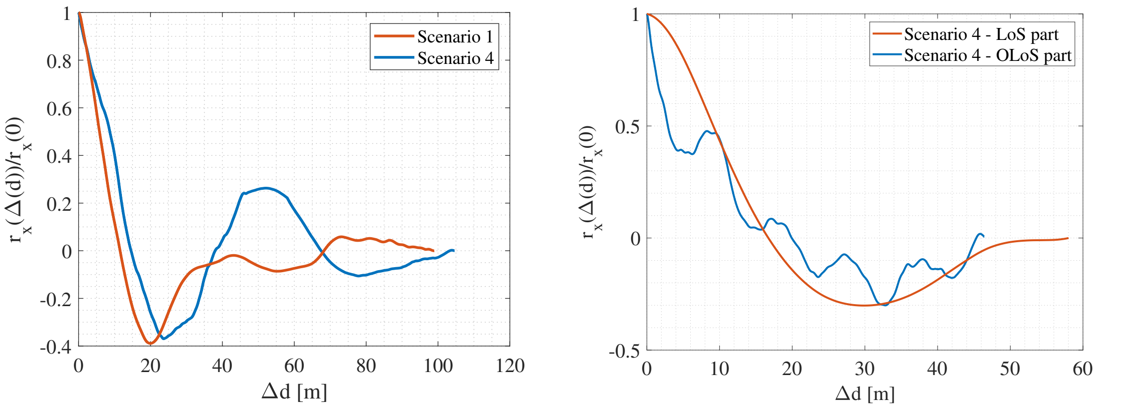

(a) Scenario 1 and Scenario 4 **(b)** LoS part and the OLoS part of Scenario 4

Figure 4.6: Normalized empirical spatial autocorrelation function of the SF for Scenario 1, Scenario 4 and the two parts of Scenario 4 in open-field.

The spatial autocorrelation function of the SF for both LoS and OLoS parts of Scenario 4 are illustrated in Figure 4.6b. Both the LoS and the OLoS parts have nearly similar correlation distances of 10.7 m and 10.9 m, respectively. However, the SF in the OLoS part experiences less correlation than the LoS part when $\Delta_d < 10\,\mathrm{m}$. This indicates that the SF varies faster compared to the LoS part within $\Delta_d < 10\,\mathrm{m}$, as can be seen in Figure 4.3. Moreover, the oscillation pattern observed in the OLoS part in Figure 4.6b is probably due to the blockage of the LoS by parked vehicles.

The empirical autocorrelation function is fitted to three theoretical autocorrelation function models, the first model is the classical model proposed by Gudmundson [62], which is based on a single negative exponential function,

$$r(\Delta d) = \exp\left(-\frac{|\Delta d|}{d_{c1}}\right), \tag{4.12}$$

where d_{c1} is the correlation distance. The second model is the double exponential model, which is also a well-known and widely used model [63]. It models the spatial correlation as a sum of two negative independent exponential functions,

$$r(\Delta d) = \alpha \exp\left(-\frac{\Delta d}{d_{c2}}\right) + (1-\alpha)\exp\left(-\frac{\Delta d}{d_{c3}}\right), \tag{4.13}$$

where $d_{c2} > 0$, $d_{c3} > 0$ and the weight factor $0 \leq \alpha \leq 1$ are tunable parameters. The third model is the exponential decaying sinusoid model [64] and is given by

$$r(\Delta d) = \exp\left(-\frac{\Delta d}{d_{c4}}\right)\left[\cos\left(-\frac{\Delta d}{d_{c5}}\right) + \frac{d_{c5}}{d_{c4}}\sin\left(-\frac{\Delta d}{d_{c5}}\right)\right], \tag{4.14}$$

where $d_{c4} > 0$ and $d_{c5} > 0$ are tunable parameters. The tunable parameters in Equations (4.13) and (4.14) are estimated in a MMSE sense.

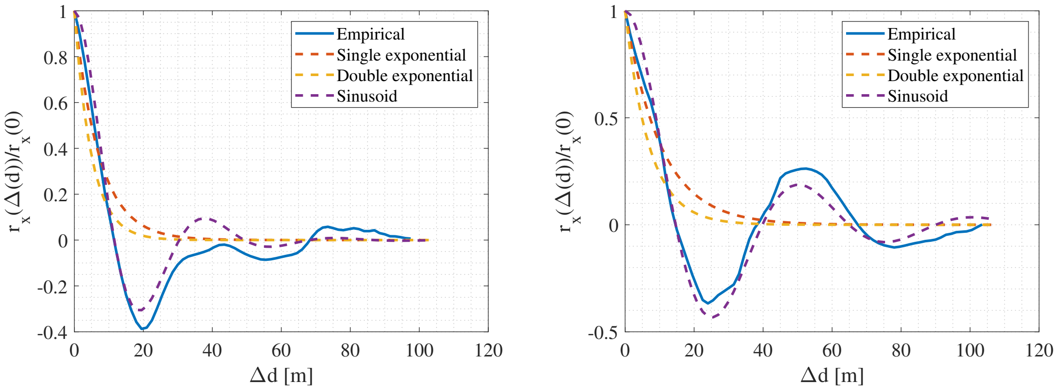

(a) Scenario 1 **(b)** Scenario 4

Figure 4.7: Normalized empirical spatial autocorrelation function of the SF and the corresponding fitting models for Scenario 1 and Scenario 4 in open-field.

From Figure 4.7 and Figure 4.8 and Table 4.3, it can be found that the single and the double exponential model can loosely follow the trend of the empirical autocorrelation function. The double exponential model performs slightly better than the exponential model with two parameters to be estimated rather than one. The exponential decaying sinusoid model provides better match to the empirical autocorrelation function in all scenarios except for the OLoS part in Figure 4.8b where all three models provide a fit with a nearly similar standard deviation σ.

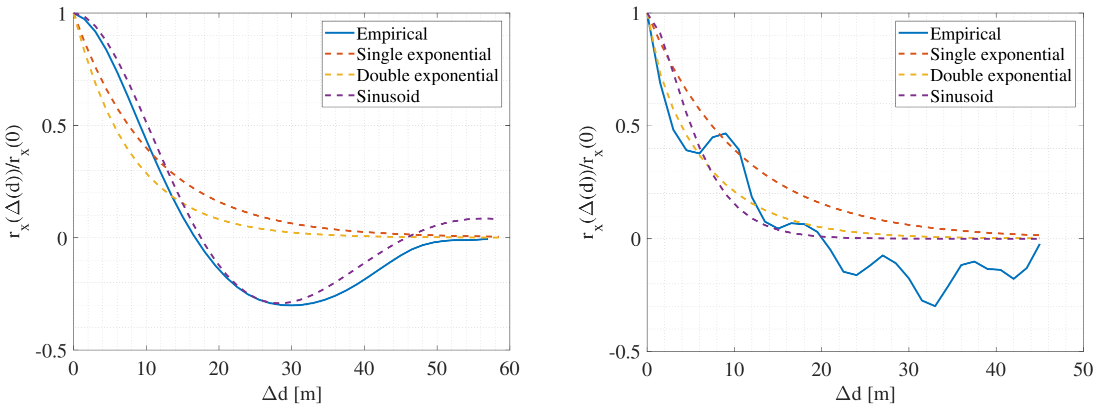

(a) LoS part (No vehicles are obstructing the LoS).

(b) OLoS part (six vehicles are obstructing the LoS).

Figure 4.8: Normalized empirical spatial autocorrelation function of the SF and the corresponding fitting models for the LoS and OLoS parts of Scenario 4 in open-field.

Model	Par	Scenario 1	Scenario 4	Scenario 4	
				OLoS part	LoS part
Single exponential	d_{c1} [m]	7.2	10.4	10.7	10.9
	σ	0.12	0.13	0.083	0.13
Double exponential	d_{c2} [m]	5	7	1	8
	d_{c3} [m]	5	7	7	8
	α	0.1	0.1	0.13	0.1
	σ	0.11	0.11	0.080	0.11
Sinusoid	d_{c4} [m]	16	30	3	23
	d_{c5} [m]	6	8	46	9
	σ	0.04	0.03	0.084	0.03

Table 4.3: Spatial correlation models' parameters.

4.3 Diffraction Loss Model

When the LoS path between the Tx and the Rx is obstructed in the Fresnel zone by an obstacle whose dimensions are larger than the wavelength of the radio wave, the measured propagation path loss is increased. The additional increase in the attenuation is due to the blockage of the LoS by the obstacles and the signal is received by diffraction of the electromagnetic waves. According to Huygens principle, the electric field is the sum of the Huygens sources located in the plane above the obstruction [30]. The calculation of the diffraction loss can be done by treating the obstacles as absorbing knife-edges [30]. Applying this simplification, the diffraction loss (in dB) becomes a function of only the Fresnel-Kirchoff parameter v as:

$$L_i = -20\ \log\left(\frac{\sqrt{[1 - C(v) - S(v)]^2 + [C(v) - S(v),]^2}}{2}\right) \tag{4.15}$$

where $C(v)$ and $S(v)$ are the Fresnel cosine and sine integrals.
The complex Fresnel integral is given by:

$$F(v) = \int_0^v \exp\left(j\frac{\pi t^2}{2}\right) \mathrm{d}t = C(v) + jS(v), \tag{4.16}$$

The Fresnel cosine and sine integrals are given by:

$$C(v) = \int_0^v \cos\left(\frac{\pi t^2}{2}\right) \mathrm{d}t \tag{4.17}$$

$$S(v) = \int_0^v \sin\left(\frac{\pi t^2}{2}\right) \mathrm{d}t \tag{4.18}$$

The sine and cosine integrals can be calculated by using their Taylor expansion as in [65],

$$\begin{aligned} C(v) &= \sum_{m=0}^{\infty} c_m v^{4m+1}, \quad c_0 = 1, \\ c_{m+1} &= \frac{-\pi^2(4m+1)c_m}{4(2m+1)(2m+2)(4m+5)} \quad . \end{aligned} \tag{4.19}$$

$$
\begin{aligned}
S(v) &= \sum_{m=0}^{\infty} s_m v^{4m+3}, \quad s_0 = \frac{\pi}{6}, \\
s_{m+1} &= \frac{-\pi^2(4m+3)s_m}{4(2m+2)(2m+3)(4m+7)} \quad .
\end{aligned}
\tag{4.20}
$$

The Fresnel-Kirchoff parameter v depends on the distance d_1 from the Tx to the diffracting edge, the distance d_2 from the diffracting edge to the Rx and the effective height h of the diffracting edge:

$$
v = h\sqrt{\frac{2(d_1 + d_2)}{\lambda d_1 d_2}}. \tag{4.21}
$$

To calculate the diffraction loss over multiple knife edges, the Epstein-Peterson method is used [66] which is illustrated in Figure 4.9. This method is found to give the best results for the given geometry. In this method, the total diffraction loss is the sum of the k losses on all edges:

$$
L_{tot} = \sum_{i=1}^{k} L_i. \tag{4.22}
$$

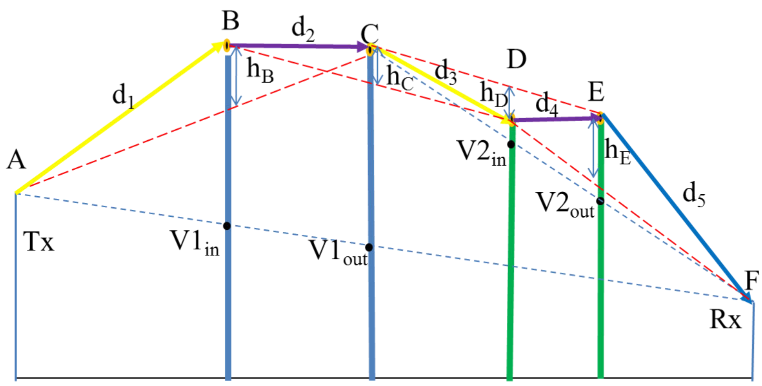

Figure 4.9: The Epstein-Peterson method for four edges. For the edge B, the geometrical parameters (d_1, d_2, h) in Equation (4.21) are (d_1, d_2, h_{B}). Similarly, for edge C, the geometrical parameters (d_1, d_2, h) in Equation (4.21) are (d_2, d_3, h_{C}). This figure can be seen as a 2D projection of the 3D model in Figure 4.11.

When calculating the loss due to diffraction from the first edge, the second edge is considered as a receiver and then to calculate the loss on the second edge, the first edge is considered as a transmitter and the third edge as a receiver and so forth.

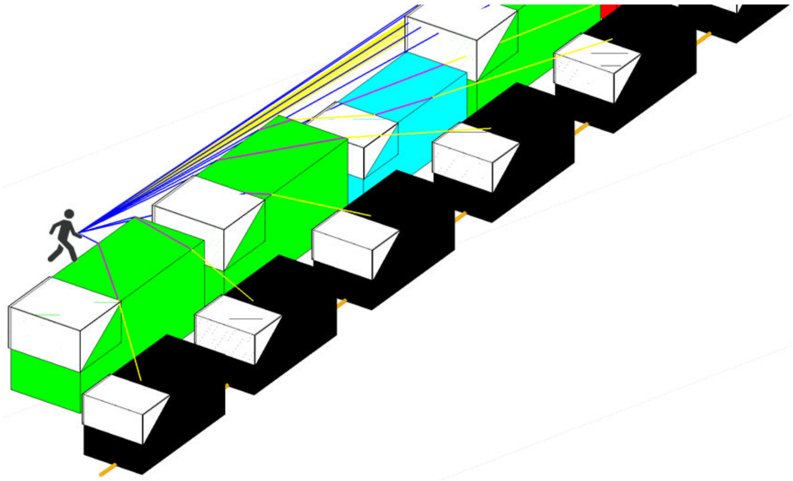

Figure 4.10: Snapshot from the 3D modeling too where the Tx (black vehicle) is shown at different positions, and the Rx (Pedestrian) is shadowed by parked vehicles.

Hence, modeling the diffraction loss requires computing the geometrical parameters d_1, d_2 and h for the diffraction process at each edge. This can be done by accurately modeling the size of the objects and their distribution in the propagation environment. To this end, a 3D tool, illustrated in Figure 4.10, is developed and published in [16]. The modeling procedure comprises the following steps:

1. Modeling static objects in the environment is done by importing the objects dimensions and locations from the laser scanner measurements and the positions of Tx and Rx from the GNSS measurements. The vehicles are represented by a cuboid and the vehicle front-end is represented by a triangular prism.

2. A direct ray from the Tx to the Rx is created, then intersections between this ray and the objects in the environment are detected as illustrated in Figure 4.11.

3. If the ray intersects with an object, two intersection points will result, entering point and exiting point. The diffraction points are found by projecting the

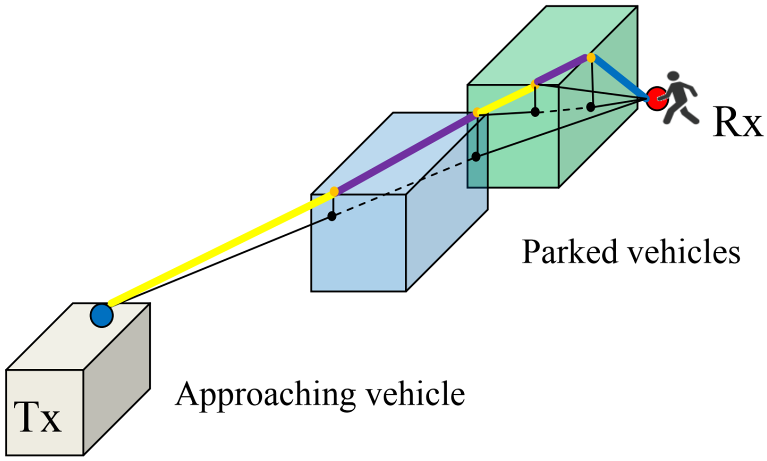

Figure 4.11: 3D illustration of the modeling procedure.

intersection points on the roof of the object. For simplicity, only roof diffraction is considered.

4. The exiting point is then treated as a secondary transmitter and the previous step is repeated to check further intersections with other objects and find the other diffraction points.

5. The diffraction loss is then calculated at each diffraction point and summed up to get the total diffraction loss.

6. The diffraction loss is combined with the two-ray path loss model to get the total propagation loss.

In Figure 4.12, the measured path loss within the obstruction region in Scenario 4 in the open-field is compared with the modeled path loss using the combined two-ray path loss model and the multiple knife-edge diffraction model. Despite its simplicity, the proposed model is able to provide a good match for the path loss with a standard deviation $\sigma = 4\,\mathrm{dB}$ when considering a line of parked vehicles between a vehicle and a pedestrian. The discontinuity of the model's curve occurs when the number of parked vehicles blocking the LoS is changed due to the movement which will result in a sudden increase or decrease in the number of diffraction edge.

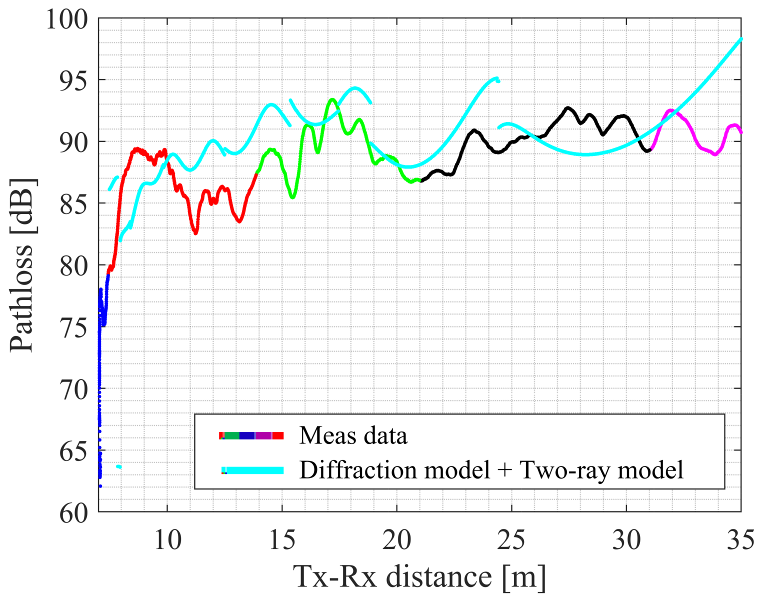

Figure 4.12: The measured path loss during obstruction of the LoS, and the modeled path loss as a summation of the multiple knife-edge diffraction model and the two-ray path loss model for Scenario 4 in open-field. The measured path loss is plotted in different colors where each color corresponds to the obstruction of the LoS by a specific vehicle. For example, the path loss in red contains the diffraction loss caused by the vehicle near the collision point.

4.4 Non-stationarity Analysis

WINNER-type GSCM channel models [15] require estimation of the LSPs and their correlation properties, such as the SF, KF, DS, and AS. For simplification, the time-variant channels are usually treated as WSSUS. Basically, a channel is called WSSUS when the first and second moments are independent from the center frequency and absolute time. However, the WSSUS assumption is often not valid especially in vehicular communications due to the high mobility of vehicles, VRUs, and the surrounding scatterers. Consequently, it is particularly important due to the non-stationarity to characterize the channel assuming local quasi-stationarity (LQS) within small regions or segments in time and frequency. The channel is divided into regions where the WSSUS assumption holds and then LSPs are estimated in each individual region. Estimation of the size of the LQS regions is important not only for the estimation of the LSPs but also for understanding the evolution of the propagation channel. The stationarity of the V2VRU channel is assisted by estimating the GLSF and its collinearity based on the channel measurement data as proposed in [67].

As detailed in [68], the local scattering function (LSF) is defined for non-WSSUS channel in continuous case as

$$C_{\mathrm{H}}(t,f;\nu,\tau) \triangleq \mathrm{F}_{\Delta t\rightarrow\nu}\left\{\mathrm{F}^{-1}_{\Delta f\rightarrow\tau}\{R_{\mathrm{H}}(t,f;\Delta t,\Delta f)\}\right\}, \tag{4.23}$$

where

$$R_{\mathrm{H}}(t,f;\Delta t,\Delta f) \triangleq \mathrm{E}\{L_{\mathrm{H}}(t,f+\Delta f)L^{*}_{\mathrm{H}}(t-\Delta t,f)\} \tag{4.24}$$

is the 4D correlation function, $L_{\mathrm{H}}(t,f)$ is the time-varying channel transfer function, and $\mathrm{E}\{.\}$ denotes the mathematical expectation. However, the LSF is not always positive and it depends on the whole correlation function $R_{\mathrm{H}}(t,f;\Delta t,\Delta f)$. Therefore [68] defines a smooth version of the LSF which is the GLSF as

$$C^{(\Phi)}_{\mathrm{H}}(t,f;\nu,\tau) \triangleq (C_{\mathrm{H}^{*}_{4}}\Phi)(t,f;\nu,\tau), \tag{4.25}$$

where

$$\Phi(t, f\nu, \tau) = \sum_{k=1}^{K} \gamma_k \int_{-\infty}^{\infty} \int_{-\infty}^{\infty} L^{*}_{\mathrm{G}_k}(-t, -f + \Delta f) \\ \times L_{\mathrm{G}_k}(-t - \Delta t, -f) e^{-j2\pi(\nu\Delta t - \tau\Delta f)} \mathrm{d}\Delta t \; \mathrm{d}\Delta f, \tag{4.26}$$

where $L_{\mathrm{G}_k}(t, f)$ are windowing functions in time-frequency, $\gamma_k \geq 0$ are normalizing constants that sum up to one, and K is the number of used windows .

Since the recorded channel transfer functions are available at discrete time and frequency instants, the discrete representation of the GLSF is given by [69]

$$C^{(\Phi)}_{\mathrm{H}}[m, q; p, n] = \sum_{k=0}^{K-1} \gamma_k \mathrm{E}\left\{ |H^{G_k}[m, q; p, n]|^2 \right\} \; . \tag{4.27}$$

The tapered frequency response is

$$H^{\mathrm{G}_k}[m, q; p, n] = \sqrt{T_s F_s} \sum_{m'=-\lfloor N_t/2 \rfloor}^{\lceil N_t/2 \rceil - 1} \sum_{q'=-\lfloor N_f/2 \rfloor}^{\lceil N_f/2 \rceil - 1} L^{*}_{\mathrm{G}_k}[m', q'] \\ \times L_{\mathrm{H}}[m + m', q + q'] e^{-j2\pi\left(\frac{pm'}{N_t} - \frac{ng'}{N_f}\right)} \; . \tag{4.28}$$

$L_{\mathrm{H}}[m, q]$, $L_{\mathrm{G}_k}[m, q]$, m, p, q, and n are the discrete representations of the continuous case, N_t and N_f are the time and frequency windows length, T_s and F_s are the difference in successive samples in time and frequency.

To evaluate the stationarity time, the collinearity between different time instants of the GLSF is estimated as

$$\alpha[m, m'] \triangleq \frac{\mathrm{tr}\left\{ \mathbf{C}^{(\Phi)^H}_{\mathrm{H}}[m, q] \mathbf{C}^{(\Phi)}_{\mathrm{H}}[m', q] \right\}}{\left\| \mathbf{C}^{(\Phi)}_{\mathrm{H}}[m, q] \right\|_F \left\| \mathbf{C}^{(\Phi)}_{\mathrm{H}}[m', q] \right\|_F} \; , \tag{4.29}$$

where tr indicates a trace operation and $\|.\|_F$ refers to frobenius norm. The resulting collinearity matrix is squared and symmetric, and the main diagonal contains values of 1. The collinearity $\alpha[m, m'] \in [0, 1]$, where 1 means a maximum correlation and 0 corresponds to no correlation. The collinearity between two GLSFs will have high value when the overlap between them is significant, and vice versa.

After the collinearity is estimated, sets $\mathcal{M}_j[m]$ are defined using a collinearity threshold th_{col} as

$$\mathcal{M}_{col}[m] \triangleq \{m'|\alpha[m,m'] > th_{col}\}\,. \tag{4.30}$$

Finally, the time dependent stationarity time is obtained

$$T_{stat,j}[m] \triangleq |\mathcal{C}_j[m]|T_s \tag{4.31}$$

where $\mathcal{C}_j[m]$ is a connected subset of $\mathcal{M}_j[m]$ that has a maximum cardinality and T_s is the samples time spacing.

To estimate the GLSF, a sliding window mechanism, with one snapshot shift, is used. A discrete prolate spheroidal sequence (DPSS) [70] is employed as a window function. Four DPS sequences in time domain and two in frequency domain ($I = 4$ and $J = 2$) are used, thus leading to a total of $K = 8$ 2D windows. The window length in time domain is set to $N_t = 30$ snapshots, which corresponds to 0.03 s or approximately 0.2 m. Since the analysis is conducted for a fixed frequency, the frequency dependency on the GLSF is omitted and only the time dependency is considered. Therefore, the window length in frequency domain is set to $N_f = 384$ frequency bins, which corresponds to the total bandwidth. The collinearity is then calculated between all GLSF delay x Doppler elements. The stationarity distance is estimated assuming a threshold $th_{col} = 0.9$ and taking into account the speed of the vehicle.

Figure 4.13 shows an example of the estimated GLSF for Scenario 3 in the urban environment at four different time instances. In Figure 4.13a, $t = 1$ s at Tx-Rx distance of 93 m, the vehicle is at the beginning of the track and moving towards the collision point, the pedestrian is standing still and shadowed by nearby parked vehicles. The LoS is diffracted at the roof of the vehicle and has a delay of 0.31 µs. Three MPCs with positive Doppler frequency are located nearby the LoS with delays between 0.32 µs and 0.34 µs originated from a building and parked vehicles on the road side opposite to the pedestrian. A negative Doppler MPC at a delay of 0.36 µs can also be seen. This MPC is due to a reflection by a building behind the vehicle. In Figure 4.13b, $t = 5$ s at distance of 55 m, the delay of the LoS component is decreased to approximately 0.18 µs as the vehicle moves towards the collision point.

The most significant MPCs have a delay between 0.19 µs and 0.26 µs with positive Doppler frequencies. These MPCs are originated from parked vehicles and buildings on both sides of the road. At distances between 55 m and 70 m, the LoS becomes less obstructed and it experiences less power fluctuations which will later has a major impact on the stationarity distance.

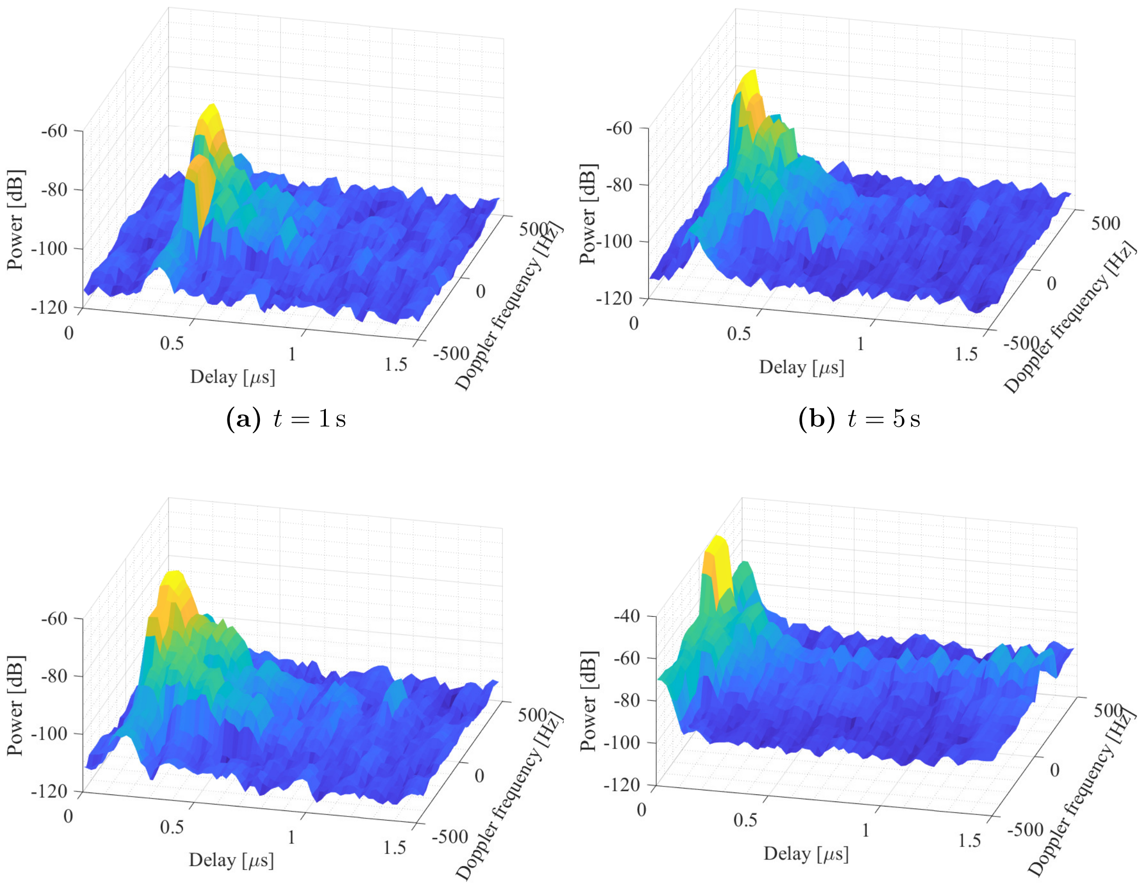

(a) $t = 1\,\mathrm{s}$ **(b)** $t = 5\,\mathrm{s}$

(c) $t = 7\,\mathrm{s}$ **(d)** $t = 11\,\mathrm{s}$

Figure 4.13: Examples of the estimated GLSF at different time instants for Scenario 3 in the urban environment.

In Figure 4.13c, $t = 7\,\mathrm{s}$ at Tx-Rx distance of 42 m, the pedestrian is attempting to cross the road and moving towards the collision point. Due to this movement, the LoS starts to experience rapid variations in power. One main difference to the previous time instant is the new MPC with zero Doppler frequency at delay of 0.26 µs which originated by reflections from parked vehicles located nearby and parallel to the moving vehicle. In Figure 4.13d, $t = 11$ s at Tx-Rx distance of 7 m, the vehicle is approximately 1 m far from the collision point where a strong LoS at 0.023 µs can be observed followed by three MPCs induced by nearby vehicles and building.

Figure 4.14 presents examples of the collinearity of the GLSF for the three scenarios in the urban environment. In all scenarios the GLSF at different Tx-Rx distances is correlated only for short travel distance/time which is implied by the observed decrease of collinearity away from the main diagonal. This decrease can be explained by the decrease of the correlation between two GLSFs as the time differences between them increases. In other words, the two GLSFs experience high correlation only for a short time period.

The collinearity of Scenario 1 in Figure 4.14a decreases much faster than in Scenario 2 and Scenario 3. This decrease can be explained by the transit from LoS to NLoS at around 30 m whereas in the other two scenarios the OLoS situation is maintained throughout most of the experiment with an exception at the collision point. The time variant structure of the collinearity in all scenarios is confirming the non-stationary nature of the propagation channel.

The estimated stationarity time is mapped to stationarity distance using the position information of the Tx and Rx. Figure 4.15 shows the corresponding stationarity distance to the collinearity of the GLSF depicted in Figure 4.14.

In all scenarios, at the shortest Tx-Rx distance, i.e., at the collision point, the stationarity distance suddenly drops. This results from the sudden change in the Doppler domain due to the LoS component, which shifts from positive to negative Doppler at the moment of passing the collision point.

Figure 4.15a shows the estimated stationarity distance for Scenario 1. An increase in the stationarity distance is observed at distances less than 20 m due to the appearance of the LoS and several strong reflections. In NLoS situation, when the cyclist is blocked by buildings, the stationarity distance varies between 0.5 m and 2.8 m. The peaks at 35 m and 70 m coincide with the appearance of a

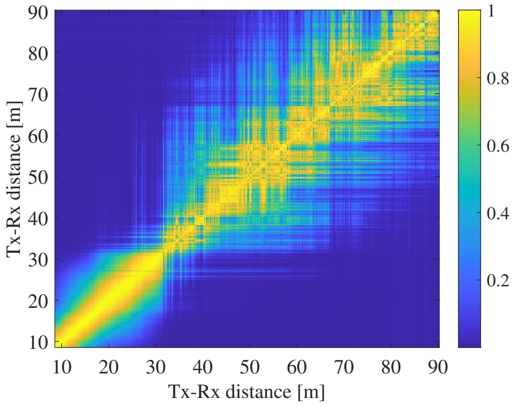

(a) Scenario 1

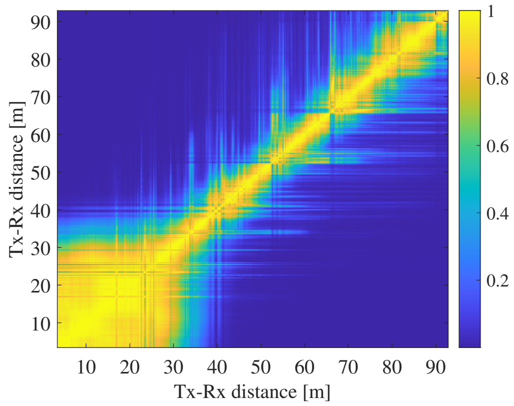

(b) Scenario 2

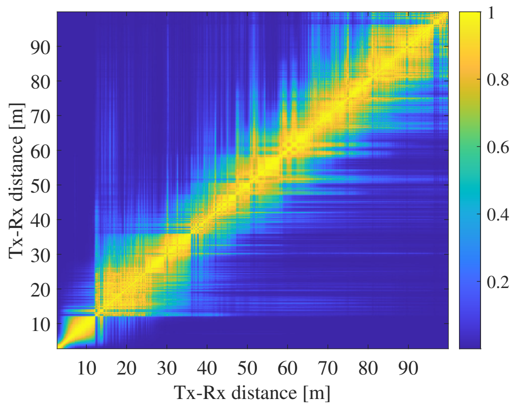

(c) Scenario 3

Figure 4.14: Examples of collinearity of the GLSF in the urban environment.

strong reflection from nearby building and a diffracted LoS on the building corner, respectively. The average stationarity distance $\overline{d_{\text{stat}}}$ in Scenario 1 is 2.13 m.

In Scenario 2 (Figure 4.15b), where the cyclist and the vehicle move on parallel tracks with an OLoS situation during the whole scenario, the average stationarity distance $\overline{d_{\text{stat}}}$ increases to 5.25 m. The maximum stationarity distance during the whole scenario is around 7 m except near the collision point where the stationarity distance rapidly varies between 3 m and 21 m due to the strong variation in LoS power. A pattern of consecutive highs and lows is observed which can be explained by the appearance and disappearance of the LoS due to the blockage by the parked vehicles. Generally, stronger LoS component leads to larger stationarity distance.

A similar pattern is observed again in Scenario 3 in Figure 4.15c. The stationarity distances in Scenarios 2 and 3 are within similar range. However, in Scenario 3 the stationarity distance at the collision point is 5 m, which is shorter than in Scenario 1 and Scenario 2. By analyzing the scatterers and their locations in Section 4.6, less reflections are found at the collision point in Scenario 3 compared to Scenario 1 and Scenario 2 which could be the reason behind the shorter stationarity distance. The average stationarity distance $\overline{d_{\text{stat}}}$ in this scenario is 3.58 m. Table 4.4 summarizes the average stationarity distances for all scenarios.

	Scenario 1	**Scenario 2**	**Scenario 3**
$\overline{d_{\text{stat}}}$ [m]	2.13	5.25	3.58

Table 4.4: Average stationarity distances in the urban environment.

The aforementioned comparison is depicted in Figure 4.16, which shows the cumulative distribution functions (CDFs) of the stationarity distances for all scenarios. Note that the the CDFs are plotted for each scenario from all measurement runs.

Stationarity Distance Relation with LoS Component, and KF in Scenario 3

To get more insight into the stationarity distance, the influence of the LoS component power on the stationarity distance is investigated. All MPCs are filtered out from

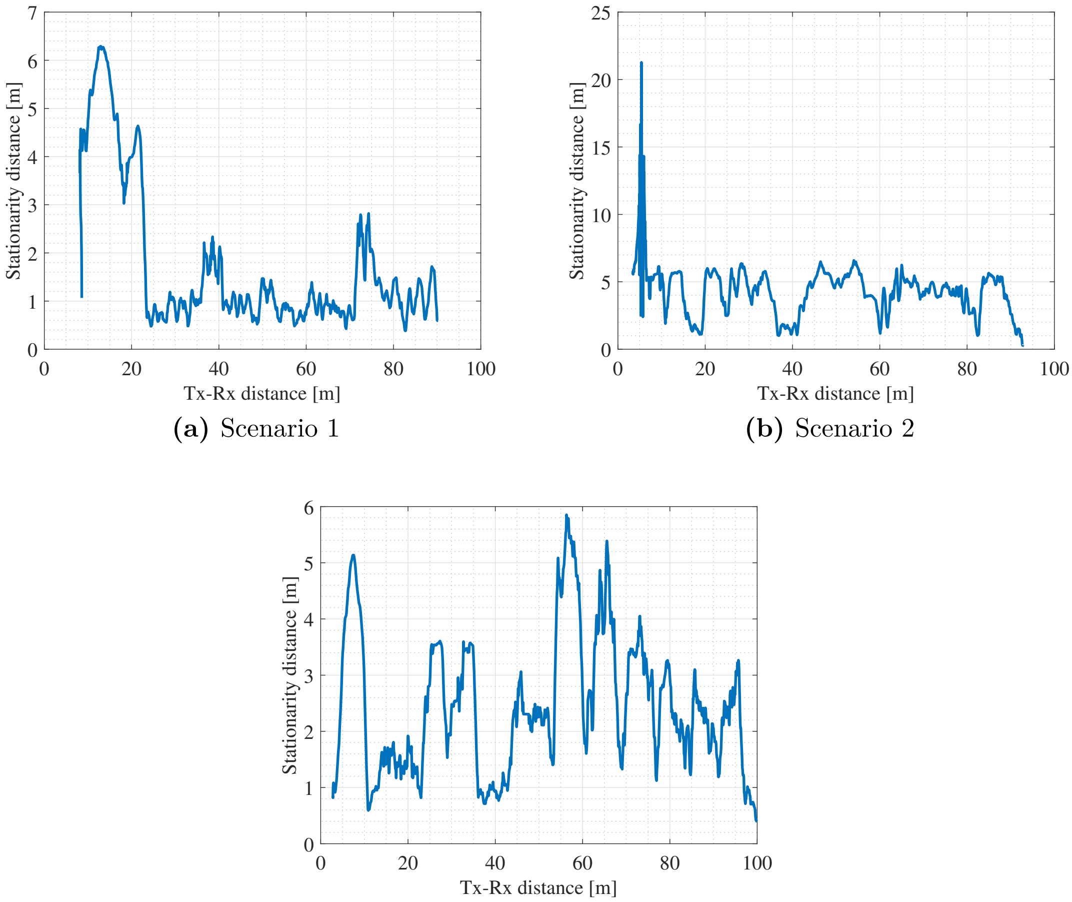

(a) Scenario 1

(b) Scenario 2

(c) Scenario 3

Figure 4.15: Stationarity distances in urban environment.

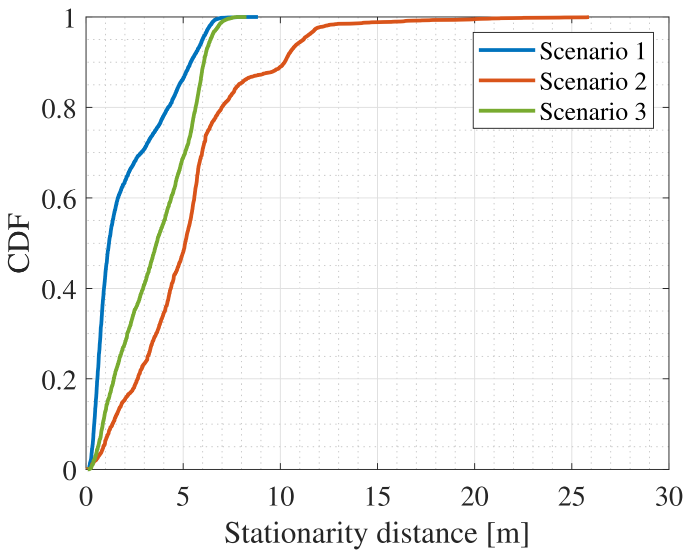

Figure 4.16: CDFs of the stationarity distances for all scenarios in the urban environment.

the corresponding CIR of Scenario 3 and only the LoS component remains. The GLSF is then estimated and based on its collinearity, the stationarity distance is estimated.

The received power carried by the LoS is plotted alongside the power carried by all MPCs, including the LoS, in Figure 4.17a. It can be seen that the total received power increases from approximately −60 dBm when the distance between the vehicle and the pedestrian is 100 m to −20 dBm at the collision point due to a strong LoS. The total received power and the power carried by the LoS component experience rapid fluctuations when the LoS between the vehicle and the pedestrian is partially or completely obstructed by parked vehicles. At a distance between 55 m and 70 m the LoS becomes less obstructed due to large gap between the parked vehicles, therefore, a slight increase in the received power and less fluctuations are observed. In Figure 4.17b the estimated K-factor is shown as it provides valuable information about the contribution of the LoS to the total received power and hence its impact on the stationarity distance. It is found that the K-factor mostly has positive values and it reaches 31 dB near the collision point. Due to diffraction loss, the LoS at some distances loses up to 15 dB from its power and therefore the K-factor drops to approximately −2 dB. However, this drop lasts only for short period.

The collinearity of the GLSF, when only the LoS component exists, is plotted in Figure 4.17c. As expected, the collinearity of the GLSF has low values at distances where the LoS undergoes rapid fluctuations, which will result in short stationarity distance. Figure 4.17d shows a comparison of the estimated stationarity distance in Scenario 3 when all MPCs are accounted for and when only the LoS component is considered. As seen from the K-factor, the LoS component is the most dominant component, therefore, the power of the LoS has the main effect on the stationarity distance. Figure 4.17b shows that the higher the K-factor, indicating higher dominance of the LoS on the total received power, the larger the stationarity distance. However, not only the power of the LoS but also its variation affects the stationarity distance. As can be noticed from Figure 4.17a, the larger and more rapid the power variations of the LoS component the shorter the stationarity distance.

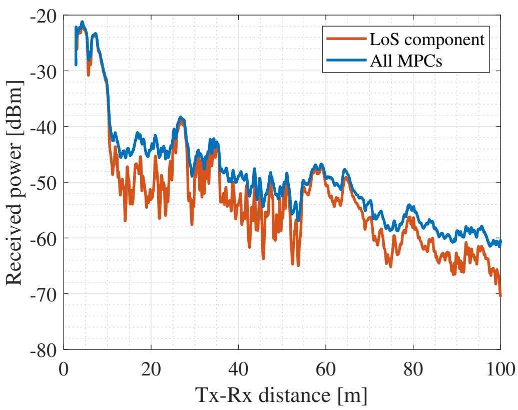

(a) Received power

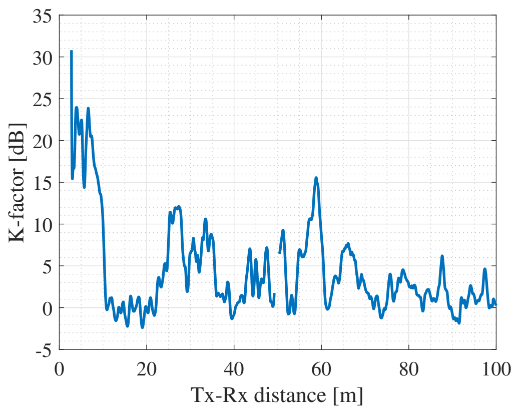

(b) K-factor

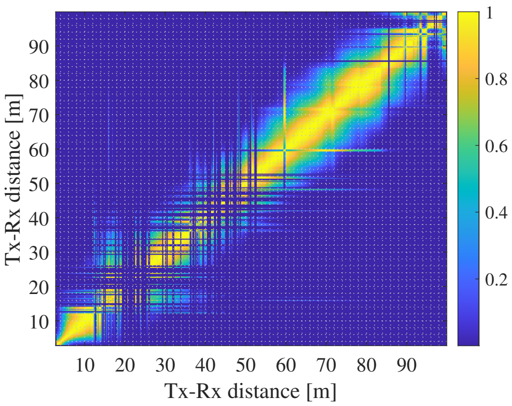

(c) Collinearity of GLSF for only LoS component

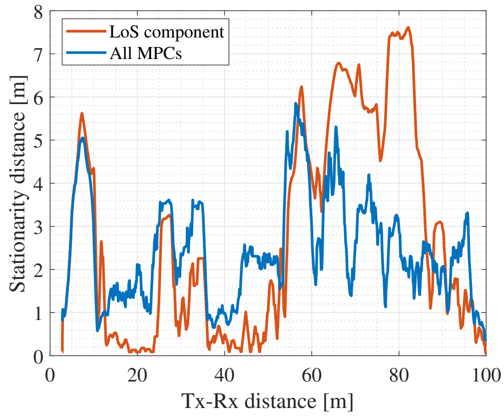

(d) Stationarity distance

Figure 4.17: Stationarity distance relation with the power of the LoS component and the KF in Scenario 3.

4.5 MPCs Parameters Estimation and Tracking

The raw measurement data obtained from channel sounding measurements cannot be directly used for a detailed characterization of the propagation channel when a GSCM channel modeling approach is targeted. Therefore, a super resolution estimation algorithm can be employed to estimate the parameters of the MPCs. Few algorithms can be found in the literature like the snapshot-based RIMAX [71], and the space-alternating generalized expectation-maximization (SAGE) [72]. Alternatively, an algorithm that takes the evolution of the multipath overtime into account such as KEST [73] will be used in this thesis.

Examples of the measured CIRs in the open-field and urban environments are shown in Figure 4.18. At the beginning of the experiment, the Tx-Rx separation distance was approximately 100 m. The LoS between the Tx and Rx was maintained in the open-field Scenario 1 with some traces parallel to the LoS. In the urban Scenario 1, as can be seen in Figure 4.18b, the LoS starts to appear, accompanied by a group of strong multipaths, at approximately 40 m distance or 12.5 s. The LoS path remains between 12.5 and 19 s but is partially obstructed by parked vehicles. During NLoS, a weak path appears as a tail of the LoS path and with a slightly more delay than the geometric LoS (GLoS) accompanied with a group of weak paths. Contrary to the open-filed, in the urban measurements, the CIR is highly cluttered. This clutter mainly consists of DMCs, but it could also contain artifacts, noise, and unreliable specular reflections, which have short lifetime (in the order of a few wavelengths) or weak power.

The behavior of the multipath channel can be described by the time variant CIR $h(t_n, \tau)$, which can be expressed mathematically as a sum of $N(t_n)$ Dirac impulses [55]:

$$h(t_n, \tau) = \sum_{m=0}^{N(t_n)-1} \alpha_m(t_n) \cdot \delta_m(\tau - \tau_m(t_n)), \tag{4.32}$$

where $\alpha_m(t_n)$, $\tau_m(t_n)$ denote the complex amplitude and the delay of the m^{th} MPC in snapshot n, and $\delta(\cdot)$ is a Dirac distribution. A dynamic multipath estimator named KEST, introduced in [73], is employed for estimating the parameters of SMCs. The estimated parameters are the absolute value of the amplitude, the delay, and the

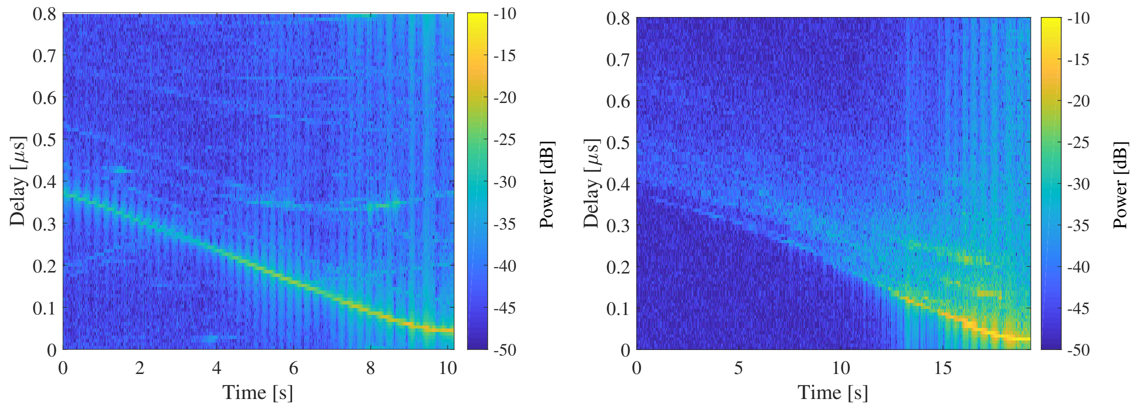

(a) Open-field: Scenario 1 **(b)** Urban: Scenario 1

Figure 4.18: Examples of the time-variant CIRs based on the measured data.

phase of each MPC at time instant t_n. KEST uses the output of SAGE algorithm [72] as measurements within a Kalman filter. SAGE is used as a snapshot-based estimator that jointly estimates the complex amplitude $\alpha_m(t_n)$ and the delay $\tau_m(t_n)$ for each MPC m. Additionally, KEST consists of several Kalman filters in parallel using different model orders for estimating the number of MPCs. Figure 4.19 shows the CIRs for open-field and urban scenarios based on the estimated parameters by the KEST algorithm. The signal period T_p of the periodically transmitted multi-tone signal in the open-field environment was selected to be equal to 0.8 µs, which corresponds to a propagation distance of 240 m. Therefore, reflections with larger propagation distance were superimposed with the CIR of the next measurement snapshot. Nevertheless, the delays of these MPCs are corrected by adding 0.8 µs in the upcoming analyses. In the open-field environment, the LoS between the Tx and the Rx was never obstructed and, consequently, the first measured path coincides with the geometric LoS. However, in the urban environment, from 0 to 12.5 s the LoS was continuously obstructed by buildings. Since the first path reaches the Rx after diffracting at the edge of the corner building, there is a misalignment between the first arriving path and the GLoS. At approximately 12.5 s or 40 m distance, the LoS path appears. A good alignment between the estimated LoS path and the GLoS can be noticed.

It can be seen that the estimation results in both scenarios confirm the initial observations made on the measured CIRs in Figure 4.18. Based on the time-delay evolution structure of the MPCs, it can be deduced, based on the long lifetimes, that all estimated MPCs in the open-field scenario are due to specular reflections. However, in the urban scenario, not only SMCs but also DMCs can be seen. Therefore, extracting the SMCs from the estimated time-variant CIR is essential in order to model the SMCs and DMCs separately.

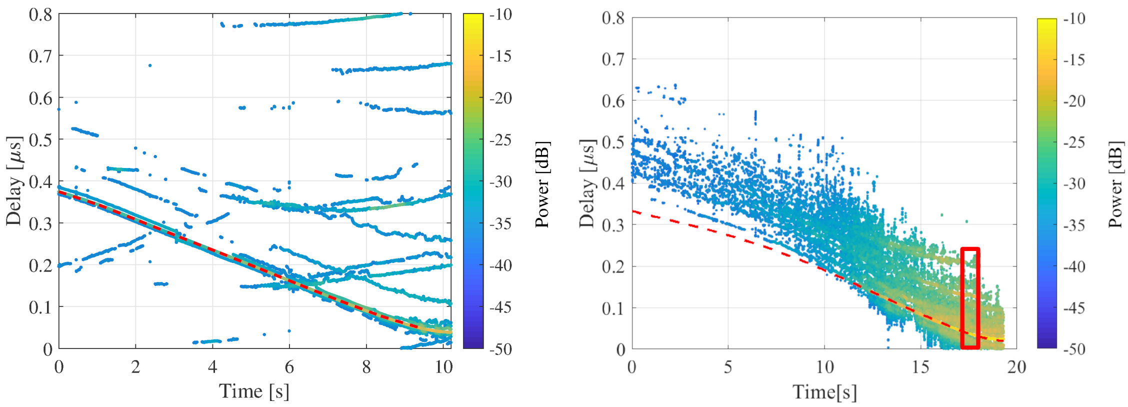

(a) Open-field: Scenario 1 **(b)** Urban: Scenario 1

Figure 4.19: Time-variant CIRs based on the estimated parameters. The geometric LoS is displayed as a red dashed line.

4.5.1 Specular Multipath Extraction

MPCs can be divided into specular reflections (SMC) and diffuse scattering (DMC). Paths with relatively high power and long lifetime are considered as SMCs. SMCs, on one hand, are coherent, which means that they have a relatively constant phase difference with the LoS path over time. While, on the other hand, DMCs will have random amplitudes and phases and therefore they are called incoherent components. Unlike SMCs, DMCs have no clear structure in the time-delay domain and are often modeled as colored noise [74, 71]. Mirror-like smooth surfaces lead to only SMCs, which are also referred to as smooth reflections. Mirror-like surfaces are rarely found in outdoor environments where most surfaces possess some roughness

(roughness in relation with the wavelength). The roughness leads to a decrease in the amplitude of the reflected path. This reduction is due to the scattering of energy in different directions. This scattered energy is carried by DMC. DMC is scattered from all or part of the rough surface and this part is called a glistening zone [29]. A very rough surface may result in canceling the contribution of the diffuse (incoherent) components. However, with a less rough surface, the DMCs contribute to the received signal and together with the specular (coherent) components produce an interference pattern on the path's amplitude. Similar to the rough surfaces, vegetation could also produces both SMCs and DMCs [75, 76].

As seen in Figure 4.19b, in the urban environment, the output of the MPCs parameters estimation not only contains SMCs but also contains DMCs. For channel modeling, the dominant SMCs with long lifetime need to be extracted. Therefore, a method to separate SMCs and DMCs based on their number of neighboring MPCs that have delay difference less or equal a specific threshold is proposed and published in [17]. The steps of the proposed method are summarized as follows:

0. For each MPC m in measurement snapshot n, a search radius δ is defined. The search region has a length of 2δ, and includes all snapshots with indices $n+p$, where $p = [-\delta, \ldots, -1, 1, 2, \ldots, \delta]$.

1. Check if the MPCs within the search region are close in delay as

$$T_{\tilde{m},n+p} = \begin{cases} 1 & \text{if} \quad |\tau_{m,n} - \tau_{\tilde{m},n+p}| \leq \zeta_{\Delta\tau} \\ 0 & \text{otherwise,} \end{cases} \tag{4.33}$$

where $\tau_{m,n}$ is the delay of the MPC m in snapshot n at time instant t_n, $\tau_{\tilde{m},n+p}$ is the delay of the MPC $\tilde{m}$ in snapshot $n+p$, $\zeta_{\Delta\tau}$ is the delay difference threshold, "1" means the MPC under examination is close in delay, and "0" means it is not. The set $\boldsymbol{\mathcal{T}}$ is defined as

$$\boldsymbol{\mathcal{T}} = \{T_{\tilde{m},n+p} \mid p = -\delta, \ldots, -1, 1, 2, \ldots, \delta, \quad \tilde{m} = 1, 2, \ldots, N_{n+p}\}, \tag{4.34}$$

where N_{n+p} is the number of MPCs in snapshot $n+p$.

2. The MPC is classified as specular or diffuse multipath as

$$\text{MPC} \triangleq \begin{cases} \text{Specular} & \text{if} \quad \sum\limits_{T_{\tilde{m},n+p} \in \mathcal{T}} T_{\tilde{m},n+p} \geq \zeta_L, \\ \text{Diffuse} & \text{otherwise,} \end{cases} \tag{4.35}$$

where ζ_L is a threshold on the number of neighbors. The MPC is considered as specular if the number of detected MPCs in the region $t_{n-\delta}, \ldots, t_{n+\delta}$ and $\tau_{m,n} - \zeta_{\Delta\tau}, \ldots, \tau_{m,n} + \zeta_{\Delta\tau}$ is larger than or equal the threshold ζ_L.

Figure 4.20 shows an example of using this method on a small part of the CIR shown in Figure 4.19b. Two MPCs, are marked by red circles, at t =17.38 s, and the search region for each of them is highlighted by a red rectangle. Based on the number of neighboring MPCs within the search region, the MPC at around 0.13 µs is classified as an SMC while the MPC at 0.11 µs is classified as a DMC and therefore it is filtered out.

Parameter	**Name**	**Value**
δ	Search region radius	25 snapshots
$\zeta_{\Delta\tau}$	Delay difference threshold	1.5 ns
ζ_L	Nr. of neighbors threshold	10 MPCs

Table 4.5: Specular reflections extraction parameters.

The values of the thresholds ζ_L and $\zeta_{\Delta\tau}$ depend on the richness of the DMCs. These values affect the performance of the extraction and therefore should be carefully chosen. By decreasing $\zeta_{\Delta\tau}$ more SMCs with high delay variations will be mistakenly classified as DMCs. Contrarily, by increasing $\zeta_{\Delta\tau}$ more DMCs will be mistakenly classified as SMCs. In order to compare the effect of variations in the $\zeta_{\Delta\tau}$ parameter, SMCs extraction is performed with three different $\zeta_{\Delta\tau}$ values. Figure 4.21 only shows the extracted SMCs for the part of the CIR within the red rectangle depicted in Figure 4.19b. With larger $\zeta_{\Delta\tau}$ more MPCs are classified as SMCs.

Similarly, decreasing ζ_L will result in more DMCs that are mistakenly classified as SMCs. On the other hand, when increasing ζ_L more SMCs, which have short

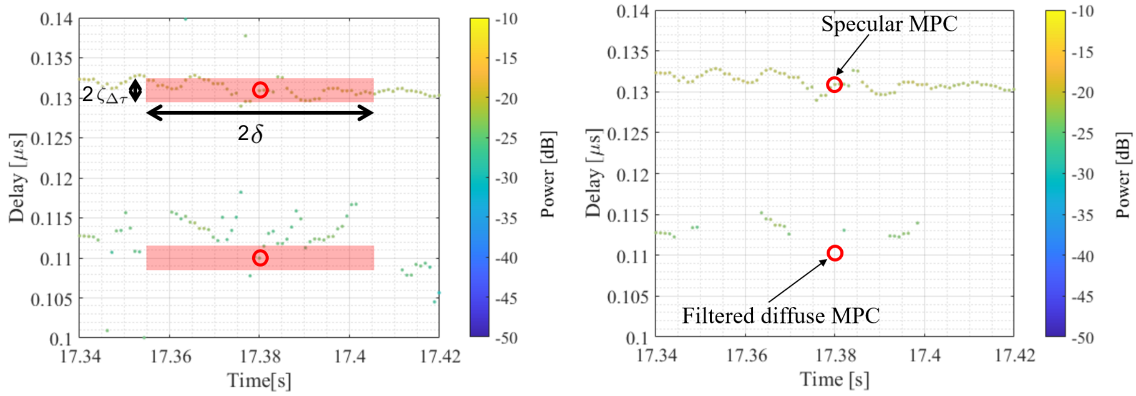

(a) Before: specular + diffuse **(b)** After: only specular

Figure 4.20: Example of applying the specular multipath extraction method.

lifetimes, are also mistakenly classified as DMCs, although a MPC that has short lifetime could be a part of a longer but discontinuous path that is associated with one scatterer in the propagation environment. The aforementioned effect of the ζ_L parameter value on the SMCs extraction can be clearly seen in Figure 4.22.

The thresholds $\zeta_{\Delta\tau}$ and ζ_L should be chosen to minimize the SMCs to be mistakenly classified as DMCs. However, this will also result in some DMCs to be classified as SMCs. Nevertheless, the misclassification of some DMCs as SMCs is affordable since their contribution to the total received power is marginal. Moreover, most of these misclassified MPCs can later be removed based on their short lifetime in the tracking step.

The aforementioned method is applied on the estimated MPCs in the urban environment from Figure 4.19b. Figure 4.23a shows the CIR based on the estimated parameters of the SMCs. The CIR of the residual after extracting the SMCs is shown in Figure 4.23b. The values of the parameters used are summarized in Table 4.5.

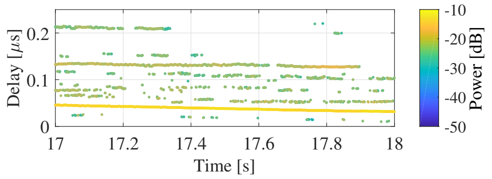

(a) $\zeta_{\Delta\tau} = 1$ ns

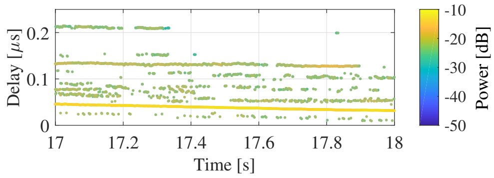

(b) $\zeta_{\Delta\tau} = 1.5$ ns

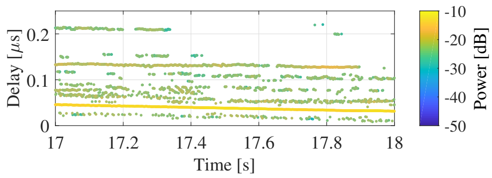

(c) $\zeta_{\Delta\tau} = 2$ ns

Figure 4.21: The extracted specular MPCs using different values for $\zeta_{\Delta\tau}$ while $\zeta_L = 10$ MPCs and $\delta = 25$ snapshots.

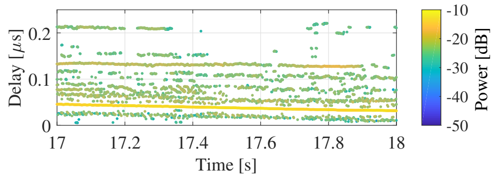

(a) $\zeta_L = 5$ MPCs

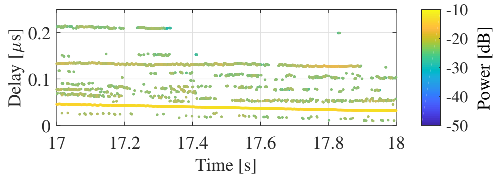

(b) $\zeta_L = 10$ MPCs

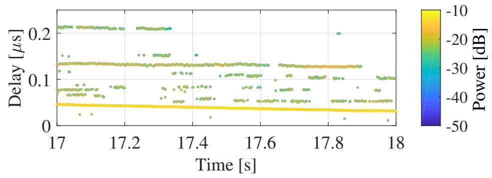

(c) $\zeta_L = 15$ MPCs

Figure 4.22: The extracted specular MPCs using different values for ζ_L while $\zeta_{\Delta\tau}$ =1.5 ns and $\delta = 25$ snapshots.

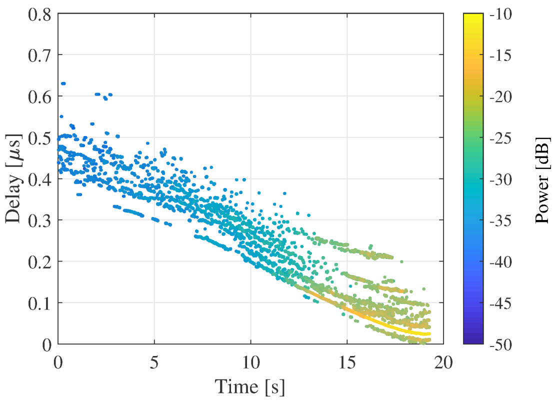

(a) Specular paths extracted from the estimated CIR

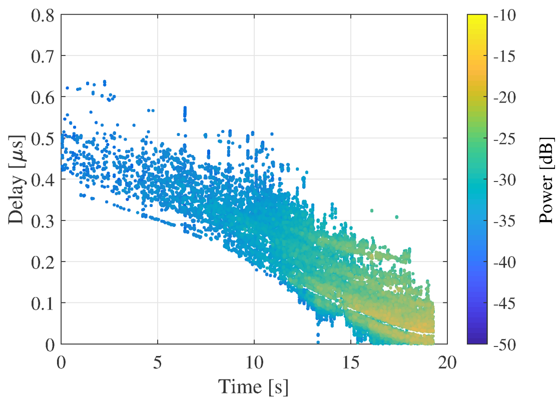

(b) The residual after extracting specular paths. The residual may contain DMC, noise, and artifacts.

Figure 4.23: Results of the specular MPCs extraction method.

4.5.2 Specular Multipath Tracking

Tracking the temporal evolution of the extracted SMCs is a prerequisite to localize their scatterers using the phase changes. The KEST algorithm is able to continuously track each estimated MPC from Figure 4.19a over time in the open-field scenario as visualized in Figure 4.24. By visual inspection it can be seen that generally the KEST algorithm correctly associates and tracks the MPCs over time. However, it is not able to track the paths for a long period of time in the urban scenario due to the richness of DMC. Therefore, in this thesis, a novel multipath component distance (MCD)-based tracking algorithm that utilizes the estimated delay and magnitude for tracking is proposed, and has been published in [17]. By assuming that in the same snapshot, the delay and magnitude of each MPC are unique, only one MPC with the same delay and magnitude exists. The main steps are as follows:

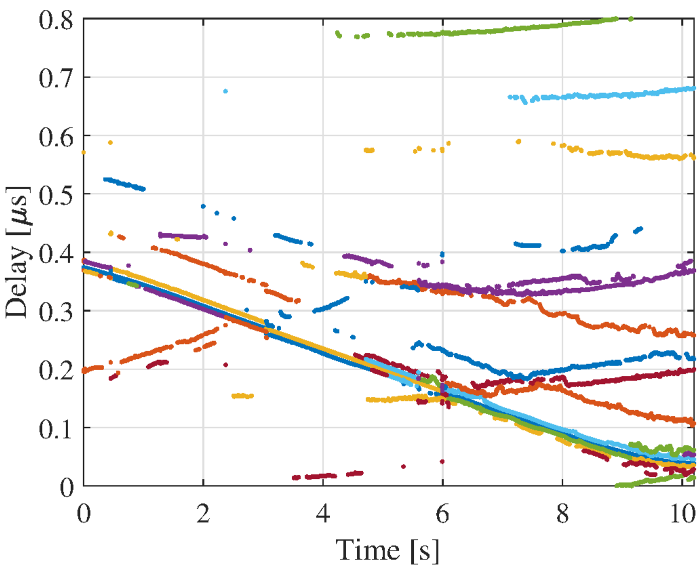

Figure 4.24: Tracked path over time in the open-field environment as a results of the KEST algorithm.

0. Initialize the set of indices (labels) of all MPCs in the first snapshot $\mathcal{I}_1 = \{1, 2, 3, \ldots, N_1\}$, Where N_1 is the number of MPCs in the snapshot $n = 1$. A delay difference threshold $\zeta_{\Delta\tau}$ is set to be equal to a predefined initial value $\zeta_{\Delta\tau_{\text{ini}}}$. A

magnitude difference threshold $\zeta_{\Delta\alpha}$ is also set to be equal to a predefined initial value $\zeta_{\Delta\alpha_{\text{ini}}}$.

For each MPC $m = 1, 2, \ldots, N_n$ in the snapshot n, do:

1. Find the set of indices of the MPCs from the previous snapshot that have delay differences to $\tau_{i_{m,n}}$ less than or equal to the threshold $\zeta_{\Delta\tau}$.

$$\boldsymbol{\mathcal{A}}_{m,n} = \{i_{\tilde{m},n-1} \in \boldsymbol{\mathcal{I}}_{n-1} \Big| \, |\tau_{i_{m,n}} - \tau_{i_{\tilde{m},n-1}}| \leq \zeta_{\Delta\tau}\}, \tag{4.36}$$

where $\boldsymbol{\mathcal{I}}_{n-1}$ is the set of all indices in the snapshot $n-1$, and $i_{\tilde{m},n-1}$ is the index (label) of the MPC $\tilde{m}$ in snapshot $n-1$.

2. Similarly, find the set of indices of the MPCs from the previous snapshot that have magnitude differences to $\alpha_{i_{m,n}}$ less than or equal to the threshold $\zeta_{\Delta\alpha}$.

$$\boldsymbol{\mathcal{B}}_{m,n} = \{i_{\tilde{m},n-1} \in \boldsymbol{\mathcal{I}}_{n-1} \Big| \, |\alpha_{i_{m,n}} - \alpha_{i_{\tilde{m},n-1}}| \leq \zeta_{\Delta\alpha}\}, \tag{4.37}$$

for simplicity in notation, $\boldsymbol{\mathcal{A}}_{m,n} \widehat{=} \boldsymbol{\mathcal{A}}$ and $\boldsymbol{\mathcal{B}}_{m,n} \widehat{=} \boldsymbol{\mathcal{B}}$.

3. Let

$$\mathcal{C} = \underset{i_{\tilde{m},n-1} \in \boldsymbol{\mathcal{I}}_{n-1}}{\arg\min} |\tau_{i_{m,n}} - \tau_{i_{\tilde{m},n-1}}| \tag{4.38}$$

be the index (label) of the MPC that has a minimum delay difference to $\tau_{i_{m,n}}$. Only one MPC will have a minimum delay difference.

4. Similarly, let

$$\mathcal{D} = \underset{i_{\tilde{m},n-1} \in \boldsymbol{\mathcal{I}}_{n-1}}{\arg\min} |\alpha_{i_{m,n}} - \alpha_{i_{\tilde{m},n-1}}| \tag{4.39}$$

be the index of the MPC that has a minimum magnitude difference to $\alpha_{i_{m,n}}$. Only one MPC will have a minimum amplitude difference.

5. For each MPC m in each snapshot n, the values of both $\zeta_{\Delta\tau}$ and $\zeta_{\Delta\alpha}$ are updated as follows

a. If $\mathcal{C} = \mathcal{D}$, $\boldsymbol{\mathcal{A}} = \emptyset$ and $\boldsymbol{\mathcal{B}} \neq \emptyset$, where $\emptyset$ is an empty set, which means that there is a MPC that has both minimum delay difference and minimum magnitude difference. However, the delay difference is above the threshold. Therefore, the current threshold is increased as

$$\zeta_{\Delta\tau} = \begin{cases} |\tau_{i_{m,n}} - \tau_{n-1}(\mathcal{C})| & \text{if } |\tau_{i_{m,n}} - \tau_{n-1}(\mathcal{C})| < \zeta_{\Delta\tau\text{ini}} \\ \zeta_{\Delta\tau\text{ini}} & \text{otherwise} \end{cases} \tag{4.40}$$

where $\tau_{n-1}(\mathcal{C})$ is the delay of the MPC that has an index $\mathcal{C}$ in snapshot $n-1$. This means that the delay difference threshold is set to be equal to the minimum difference if this minimum does not exceed the initial delay difference threshold. Otherwise, the threshold will be updated to be equal to the initial threshold.

The magnitude threshold is updated by a weighted average

$$\zeta_{\Delta\alpha} = \kappa_\alpha \overline{\Delta\alpha_k(\mathcal{D})}, \tag{4.41}$$

where $\Delta\alpha_k(\mathcal{D}) = |\alpha_k(\mathcal{D}) - \alpha_{k-1}(\mathcal{D})|$ is the absolute of the magnitude difference between two MPCs with the same index $\mathcal{D}$ in consecutive snapshots, $k = n - 500, \ldots, n-1$ are the indices of the previous 500 snapshots, and $\kappa_\alpha > 1$ is a constant parameter. This means that the magnitude difference threshold is updated by the weighted average of the magnitude differences in the closest tracked path.

b. If $\mathcal{C} = \mathcal{D}$, $\boldsymbol{\mathcal{A}} \neq \emptyset$ and $\boldsymbol{\mathcal{B}} = \emptyset$, which means that there is a MPC that has both minimum delay difference and minimum magnitude difference. However, the magnitude difference is above the threshold. Therefore, the current magnitude threshold is increased as

$$\zeta_{\Delta\alpha} = \begin{cases} |\alpha_{i_{m,n}} - \alpha_{n-1}(\mathcal{C})| & \text{if } |\alpha_{i_{m,n}} - \alpha_{n-1}(\mathcal{C})| < \zeta_{\Delta\alpha\text{ini}} \\ \zeta_{\Delta\alpha\text{ini}} & \text{otherwise} \end{cases} \tag{4.42}$$

Similar to (a), the delay threshold is updated by a weighted average

$$\zeta_{\Delta\tau} = \kappa_\tau \overline{\Delta\tau_k(\mathcal{C})}, \tag{4.43}$$

where $\Delta\tau_k(\mathcal{C}) = |\tau_k(\mathcal{C}) - \tau_{k-1}(\mathcal{C})|$ is the absolute of the delay difference between two MPCs with the same index $\mathcal{C}$ in consecutive snapshots, $k = n - 500, \ldots, n - 1$ are the indices of the previous 500 snapshots, and $\kappa_\tau > 1$ is a constant parameter.

After updating the thresholds, the tracking begins as follows:

6. If $\boldsymbol{\mathcal{A}} \cap \boldsymbol{\mathcal{B}} \neq \emptyset$, one or more matching MPCs are found. If more than one matching MPCs are found, then select the one which has the least delay difference. If the index of the matching MPC is not already assigned to another MPC in the same snapshot n (step 7), then $\mathcal{I}_{m,n} = \boldsymbol{\mathcal{A}} \cap \boldsymbol{\mathcal{B}}$.

7. If $\boldsymbol{\mathcal{A}} \neq \emptyset$, $\boldsymbol{\mathcal{B}} \neq \emptyset$, and $\boldsymbol{\mathcal{A}} \cap \boldsymbol{\mathcal{B}} = \emptyset$, then there are at least two different MPCs, one of them satisfies the magnitude difference condition and the other satisfies the delay difference condition. In order to decide which MPC to choose, a metric γ for each choice is calculated as

$$\gamma_\tau = \omega_\tau \left(\frac{\zeta_{\Delta\tau}}{|\tau_{i_{m,n}} - \tau_{n-1}(\mathcal{C})|} \right) + \omega_\alpha \left(\frac{\zeta_{\Delta\alpha}}{|\alpha_{i_{m,n}} - \alpha_{n-1}(\mathcal{C})|} \right), \tag{4.44}$$

and

$$\gamma_\alpha = \omega_\tau \left(\frac{\zeta_{\Delta\tau}}{|\tau_{i_{m,n}} - \tau_{n-1}(\mathcal{D})|} \right) + \omega_\alpha \left(\frac{\zeta_{\Delta\alpha}}{|\alpha_{i_{m,n}} - \alpha_{n-1}(\mathcal{D})|} \right), \tag{4.45}$$

where $\omega_\tau + \omega_\alpha = 1$, and $\omega_\tau > 0$, $\omega_\alpha > 0$ are the weight parameters of the delay and magnitude, respectively. Based on the values of γ_τ and γ_α, the matching MPC is then selected as

$$i_{m,n} = \begin{cases} \mathcal{C} & \text{if} \quad \gamma_\tau \geq \gamma_\alpha \\ \mathcal{D} & \text{if} \quad \gamma_\alpha > \gamma_\tau. \end{cases} \tag{4.46}$$

Which means that matching MPC is the one that satisfies the delay condition if $\gamma_\tau \geq \gamma_\alpha$, or it is the one that satisfies the magnitude condition if $\gamma_\alpha > \gamma_\tau$. However, the selection is final only if the index of the matching MPC is not already assigned to another MPC in the same snapshot n (step 8).

8. If the index of the matching MPC is already selected by another MPC with a delay $\tau_{i_{l,n}}$, then the delay of both MPCs will be compared with $\tau_{n-1}(\mathcal{C})$. The MPC with the least delay difference will be assigned the index $\mathcal{C}$ while the other MPC

will search for a match within the previous δ_p snapshots (step 10), where δ_p is a constant parameter corresponding to the length of the search region,

$$i_{m,n} = \begin{cases} \mathcal{C} & \text{if } |\tau_{i_{m,n}} - \tau_{n-1}(\mathcal{C})| < |\tau_{i_{l,n}} - \tau_{n-1}(\mathcal{C})|, \\ \text{Search back (step 10)} & \text{otherwise,} \end{cases} \quad (4.47)$$

and consequently,

$$i_{l,n} = \begin{cases} \mathcal{C} & \text{if } |\tau_{i_{l,n}} - \tau_{n-1}(\mathcal{C})| < |\tau_{i_{m,n}} - \tau_{n-1}(\mathcal{C})|, \\ \text{Search back (step 10)} & \text{otherwise.} \end{cases} \quad (4.48)$$

9. If $\boldsymbol{\mathcal{A}} = \emptyset$ or $\boldsymbol{\mathcal{B}} = \emptyset$, then there is no match in the previous snapshot. Therefore, the MPC will search for a match within the previous δ_p snapshots (step 10).

10. Search Back: When the MPC does not find a match from the previous snapshot, then it searches for a match within a window of length δ_p snapshots. For each MPC in each snapshot in the search window, the distance metric is calculated as,

$$S_{\tilde{m},n-p} = \sqrt{\omega_\tau \left(\frac{\tau_{i_{m,n}} - \tau_{i_{\tilde{m},n-p}}}{\tau_{i_{m,n}}} \right)^2 + \omega_\alpha \left(\frac{\alpha_{i_{m,n}} - \alpha_{i_{\tilde{m},n-p}}}{\alpha_{i_{m,n}}} \right)^2}, \quad (4.49)$$

where $\boldsymbol{\mathcal{S}}_p = \{S_{\tilde{m},n-p} \big| p = 2, 3, , \ldots, \delta_p + 1\}$ is a set of all distances $S_{\tilde{m},n-p}$, and $p = 2, 3, , \ldots, \delta_p + 1$. The matching MPC is selected as follows:

$$i_{m,n} = \begin{cases} i_{\tilde{m},n-p} & \text{if } \quad S_{\tilde{m},n-p} = \min(\boldsymbol{\mathcal{S}}_p) \\ \text{new path} & \text{otherwise,} \end{cases} \quad (4.50)$$

If a matching path is found go to (step 8), and if the path is considered as a new path, it will get a new index.

The parameters values used for tracking are summarized in Table 4.6.

The performance of the algorithm is subjected to the value of the parameters. The parameter tuning procedure could be long and time consuming. The proposed tracking algorithm will only require minimum offline tuning efforts. Seven parameters, listed in Table 4.6, need to be initialized, and two parameters, namely, the delay difference threshold $\zeta_{\Delta\tau}$ and the magnitude difference threshold $\zeta_{\Delta\alpha}$ are tuned automatically. The measured delay differences $|\tau_{i_{m,n}} - \tau_{i_{\tilde{m},n-1}}|$ and the updated delay threshold for the LoS path are shown in Figure 4.25a. The updated threshold is upper-bounded by the initial threshold $\zeta_{\Delta\tau_{\text{ini}}} = 10\,\text{ns}$ and its value for each MPC in each snapshot is updated as in step 5. Similarly, the measured magnitude differences $|\alpha_{i_{m,n}} - \alpha_{i_{\tilde{m},n-1}}|$ and the updated magnitude threshold for the LoS path are shown in Figure 4.25b

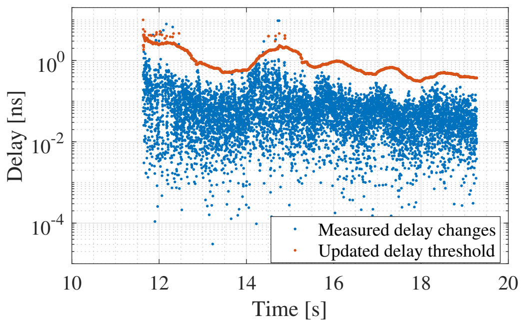

(a) Delay threshold update

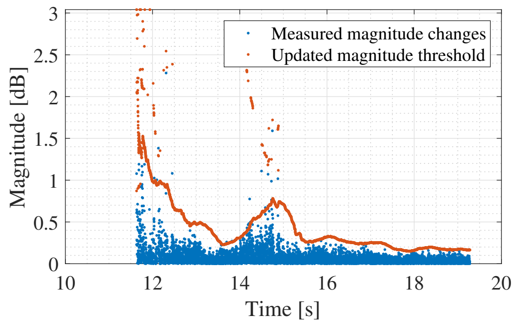

(b) Magnitude threshold update

Figure 4.25: The automated tuning of the delay and magnitude threshold for the LoS component.

The initial thresholds $\zeta_{\Delta\tau_{\text{ini}}}$ and $\zeta_{\Delta\alpha_{\text{ini}}}$ represent upper bounds on the delay and amplitude changes between two consecutive measurement snapshots. It is only important to choose values larger than the average delay and amplitude changes between two consecutive measurement snapshots. For example with average delay change of 0.5 ns, any value between $5 - 10\,\text{ns}$ is suitable. Similarly, with an average magnitude change of 0.15 dB, any value between 1.5 and 3 dB is suitable. The constants parameter κ_τ is used to update the delay threshold in Step 5b. In this initial tracking, the LoS can be easily tracked because of its high power and smooth delay evolution over time. Based on the delay changes within the tracked LoS path, the weighting constants are tuned to be large enough such that the updated threshold is larger than the delay difference of the tracked LoS and small enough to not exceed the initial threshold. Similar procedure is also applied to tune κ_α.

When the algorithm needs to decide between two MPCs, only one satisfies the delay condition while the other only satisfies the power condition, the weighting constants ω_τ and ω_α become useful. Higher delay weight means that the delay similarity is preferred over the power similarity. The selection of the weights values depends on the objective of the tracking and on the data. Due to the fact that paths with different delay may have similar power and the objective is to track the evolution of MPCs over time, larger delay weight is selected.

Parameter	Name	Value
$\zeta_{\Delta\tau\mathrm{ini}}$	Initial delay difference threshold	10 ns
$\zeta_{\Delta\alpha\mathrm{ini}}$	Initial magnitude difference threshold	3.04 dB
κ_τ	Tuning constant for delay difference threshold	10
κ_α	Tuning constant for magnitude difference threshold	5
ω_τ	Delay weight	0.9
ω_α	Magnitude weight	0.1
δ_p	Search range	100 snapshots

Table 4.6: Tracking parameters.

Figure 4.26 displays the results of the SMCs tracking for the urban environment of Figure 4.19b. In the first part of the measurements until 12.5 s where Tx and Rx were in NLoS condition, the algorithm succeeds in tracking the signal diffracted by the obstructing building (B7). However it is unable to find singular MPCs that can be tracked over longer periods of time inside the (B1) cloud. In the LoS situation, when stronger and more discrete MPCs appear, the algorithm is again able to track some strong MPCs, as for instance (B2, B3, and B5). These MPCs appear divided in different chunks. If they belong to the same or to different objects will be assessed in the next section. The accuracy of scatterer localization in the next section can be considered as an indication of the performance of the proposed tracking algorithm.

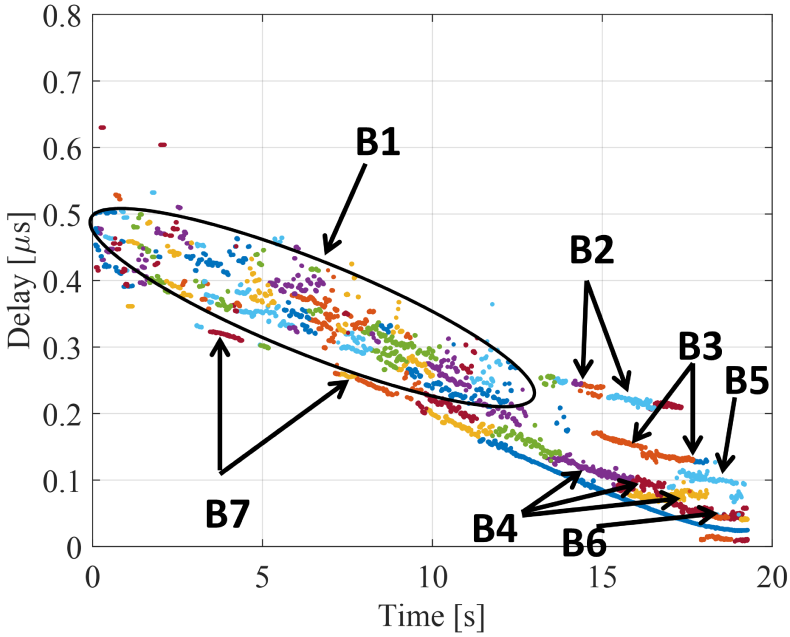

Figure 4.26: Tracked path over time for Scenario 1 in the urban environment as a results of the proposed tracking algorithm.

4.6 Scatterers Localization

The Doppler ν is estimated based on the phase of the estimated complex amplitude. The estimated delay τ and Doppler are used to localize scatterers in the propagation environment. For the sake of simplicity, a reflecting object is considered as a source of single bounce reflection. A two-dimensional Cartesian coordinate system is considered to describe the propagation scenario. The LoS and the scattered components are assumed to propagate horizontally. This means that the differences in antenna heights and the scattering point height are neglected and the scatterers are then located on a ground plane together with the Tx and Rx antennas. The delay τ of a MPC depends on the Tx position $\mathbf{T}$, the Rx position $\mathbf{R}$, and the scatterer position $\mathbf{S}$ as

$$\tau = \frac{1}{\mathrm{c}} \left(\|\mathbf{S} - \mathbf{T}\| + \|\mathbf{R} - \mathbf{S}\| \right), \tag{4.51}$$

where c is the speed of light.

When only Tx or Rx is moving, the Doppler frequency ν in the 2D Cartesian coordinate system has a shape of a hyperbola. However, if both Tx and Rx are moving, the Doppler frequency has no typical shape any more. The Doppler frequency is given by

$$\nu = \frac{f_\mathrm{c}}{\mathrm{c}} \left(\upsilon_\mathrm{T} \frac{\mathbf{S}-\mathbf{T}}{\|\mathbf{S}-\mathbf{T}\|} + \upsilon_\mathrm{R} \frac{\mathbf{R}-\mathbf{S}}{\|\mathbf{R}-\mathbf{S}\|} \right), \tag{4.52}$$

where υ_T and υ_R are the velocity of Tx and Rx, respectively. In this representation, the scatterer location is calculated by intersecting the curves represented by τ and ν. The intersection results in two points on the ellipse given by Equation (4.51). Only one of them is the true scattering point location while the other is an ambiguity. In this thesis, the localization algorithm from [77] is employed where scatterer location in each snapshot n and MPC m is calculated as a probability density function (PDF). τ and ν are jointly expressed as a bivariate normal distribution, i.e., $\mathbf{K}(\boldsymbol{\theta}) \sim \mathcal{N}(\boldsymbol{\mu}, \boldsymbol{\Sigma})$ in the parameter space $\boldsymbol{\theta}$

$$\boldsymbol{\theta} = \begin{bmatrix} \tau \\ \nu \end{bmatrix}, \tag{4.53}$$

where

$$\boldsymbol{\mu} = \begin{bmatrix} \mu_\tau \\ \mu_\nu \end{bmatrix}, \tag{4.54}$$

is the mean values, and

$$\boldsymbol{\Sigma} = \begin{bmatrix} \sigma_\tau^2 & 0 \\ 0 & \sigma_\nu^2 \end{bmatrix}, \tag{4.55}$$

is the covariance matrix, which is calculated from the estimated parameters in Section 4.5 assuming that τ and ν are independent. The joint PDF of the parameter $\boldsymbol{\theta}$ is given by

$$p(\boldsymbol{\theta}; \boldsymbol{\mu}, \boldsymbol{\Sigma}) = \frac{1}{2\pi\sigma_\tau\sigma_\nu} \exp\left(-\frac{(\tau-\mu_\tau)^2}{2\sigma_\tau^2} - \frac{(\nu-\mu_\nu)^2}{2\sigma_\nu^2} \right). \tag{4.56}$$

The next step is to transform the PDF $p(\boldsymbol{\theta}; \boldsymbol{\mu}, \boldsymbol{\Sigma})$ from the parameter domain into the Cartesian domain as

$$p(\boldsymbol{X}) = \frac{1}{N} p(\boldsymbol{\theta}) |\mathbf{J}|, \tag{4.57}$$

where N is the number of intersections between the shape defined by τ and the shape defined by ν, $\boldsymbol{X} = [x, y]^{\mathrm{T}}$, and $\mathbf{J}$ is the Jacobian of $\boldsymbol{\theta}$

$$\mathbf{J} = \det\left(\begin{bmatrix} \frac{\partial \tau}{\partial x} & \frac{\partial \tau}{\partial y} \\ \frac{\partial \nu}{\partial x} & \frac{\partial \nu}{\partial y} \end{bmatrix}\right). \tag{4.58}$$

The PDFs of the same MPC are then averaged over the lifetime of the MPC. During the movement of Tx and Rx, the ambiguities change their locations while the true locations remain fixed. As a result of the averaging, the ambiguities are partially or completely averaged out.

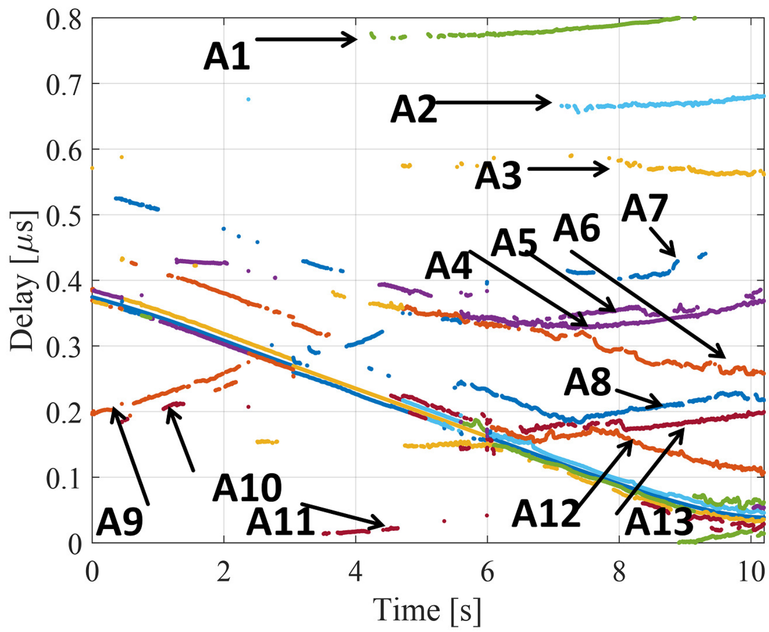

Figure 4.27: Tracked paths over time in the open-field environment as a results of KEST algorithm.

The CIR of Scenario 1 in the open-field environment is shown in Figure 4.27. Each MPC is tracked over time and then related to a physical scatterer in the propagation environment. Figure 4.28 shows the estimated locations of scatterers in the open-field environment, and the photos of the scatterers are shown in Figure 4.29. The purpose of showing the results of scatterers localization in the open-field environment is to show the performance of the localization algorithm in an controlled environment

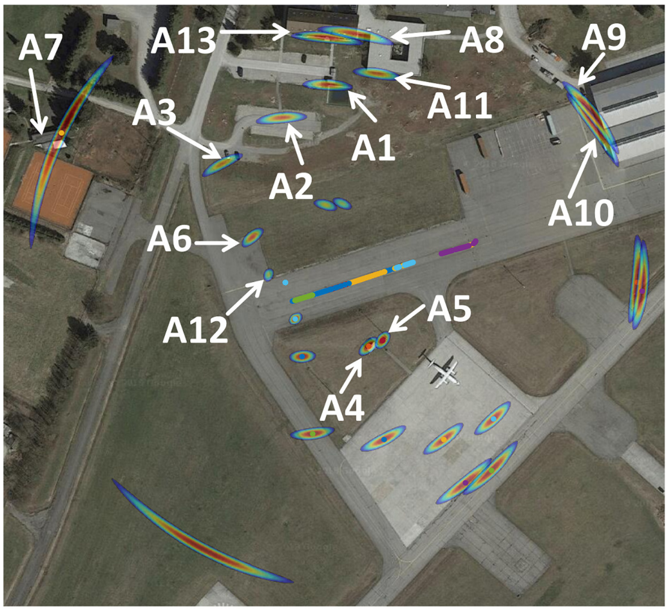

Figure 4.28: Estimated Locations of the scatterers in open-field scenario. The results not only show the true locations but also the ambiguities. The trajectories of the Tx and the Rx are shown © Google.

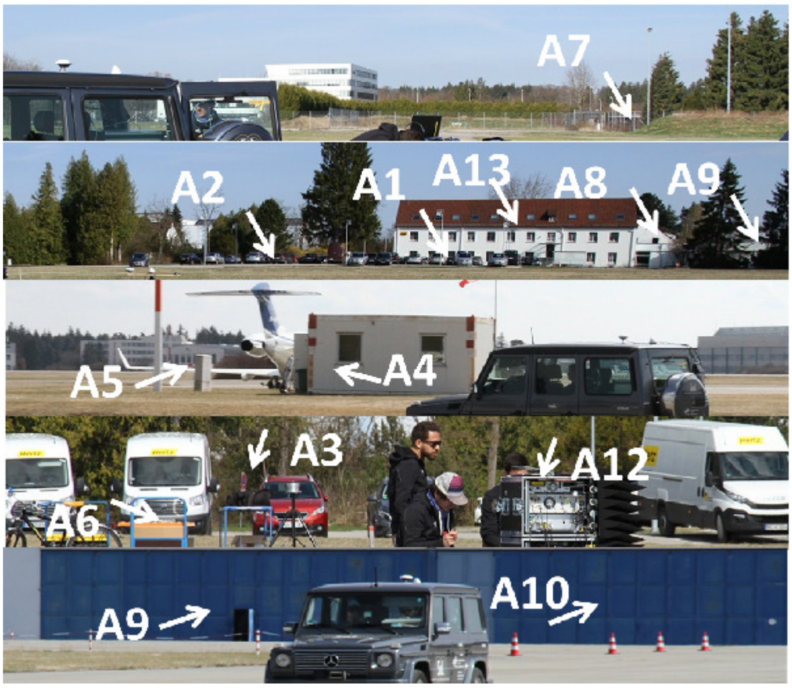

Figure 4.29: Photos of the localized scatterers in the open-field environment.

with perfect GNSS reception and low multipath interference. The results show that the localization algorithm is able to accurately localize the scatterers. The PDFs, which are marked by arrows, represent the PDFs of the true location. Other PDFs represent the ambiguities. Since only the Tx is moving, while the Rx is static, the ambiguities do not change their position and therefore do not average out. At large Tx-Rx separation distance, reflection occurs on the hangars (A9 and A10). As the vehicle approaches the collision point, other scatterers become active such as the parked vehicles in the parking lots (A1, A2, and A3), a small metal container (A4) and a nearby metal electric box (A5). Far office buildings (A8, A11, A13, and A7) are also identified as reflection sources. A12 and A6 are the positions of the channel sounder and the nearby trolleys, respectively.

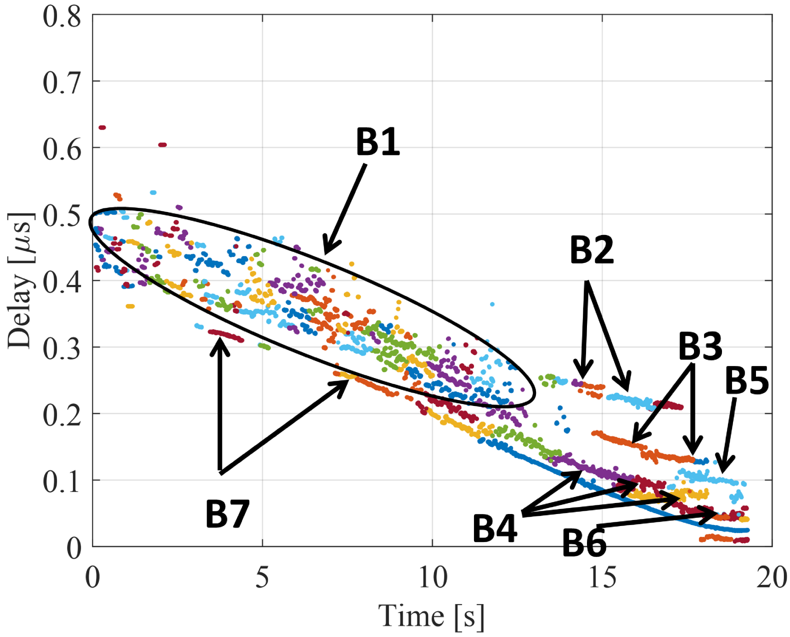

Figure 4.30: Tracked path over time for Scenario 1 in the urban environment as a results of the proposed tracking algorithm.

The locations of the scatterers for all scenarios are estimated. An example of the scatterers location is shown in Figure 4.31 for Scenario 1 in the urban environment. In NLoS situation, several short MPCs (B1) in Figure 4.30 reach the receiver after scattering from tree branches and leaves as shown in Figure 4.31a and Figure 4.32.

(a) NLoS

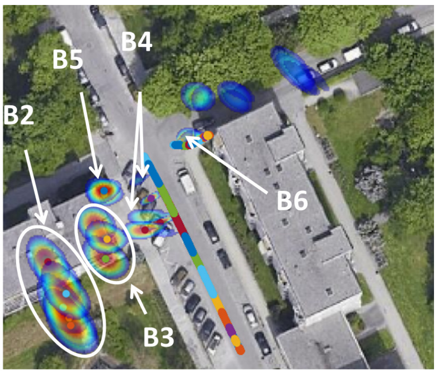

(b) LoS

Figure 4.31: Estimated Locations of the scatterers in the urban Scenario 1. The results not only show the true locations but also the ambiguities. The trajectories of the Tx and the Rx are shown © Google. At each time instant, the trajectories of the Tx and Rx together with the point in the center of the location PDF have the same color.

Figure 4.32: Photos of the localized scatterers in the urban Scenario 1.

The lampposts and the traffic signs under the trees canopy (B1) could also be sources of reflections during NLoS situation. It can be seen that the ambiguities are partially averaged. Despite the existence of several objects, such as parked cars, traffic signs, and the corner building, that have visibility to both the Tx and the Rx, no MPCs are received from these objects. Simply, in NLoS scenario the location of these objects and the position of Tx and Rx do not satisfy the law of reflection.

Single and double-bounce specular reflections from the surrounding objects in the environment in LoS situation are observed. The estimated locations of the single bounce reflections (B3) are not exactly on the facade of the building but rather $1-2$ m behind it as shown in Figure 4.31b. One reason could be the inaccuracy of GNSS data. Moreover, it is assumed that the reflection point together with the Tx and Rx antennas are located on the same horizontal plane. Therefore, when the actual height of the reflection point does not comply with the assumption, the estimated location will appear in front of or behind the facade of the reflectors. In this scenario, (B3) MPCs are most probably generated by reflections from the metallic balconies of the first floor. The estimated locations of the MPCs (B2) appear to be about 15 m behind the building facade. It has been found, by simple ray-tracing, that MPCs (B2) are generated by double bounce reflections from the right then the left buildings. In addition to the single and double-bounce reflections from the right and left building, reflections from several parked cars (B4) on the left side of the road and from a car (B6) at the corner near to the cyclist are also observed. Moreover, the metallic shop sign is found to be the source of reflections (B5).

The AoD and AoA of each MPC at each measurement snapshot are then calculated geometrically from the estimated position of the last-bounce scatterer with respect to the positions of the Tx and Rx.

4.7 Diffuse Multipath Components

When modeling the radio channel following the GSCM approach, it is often assumed that the channel is a collection of specular and discrete multipaths that can be associated with large and discrete objects with mirror-like reflecting surfaces. However, [78] shows that the propagation channel does not only consist of SMCs[2], but also DMCs. DMC is the part of the channel energy that cannot be associated with SMC disregarding its propagation mechanism, e.g., reflection, scattering, and diffraction. DMC consists of large number of weak MPCs and large portion of it is originated from diffuse scattering on rough surfaces, on small objects compared to the signal wavelength, and on surfaces with multiple layers of different materials [29]. DMCs could also contain SMCs that cannot be reliably detected due to their too weak signal-to-noise-ratio (SNR) or due to specular reflection model mismatch [79], [74]. In a propagation channel, there are relatively small number of SMC compared to the larger number of DMC. Although the power of a single SMC is much larger than the power of a single DMC, but due to the large number of DMCs, their contribution to the total received power can be significant and even dominant depending on the propagation environment. Neglecting the DMC in channel models may result in underestimating the received power and the channel capacity [80]. However, the contribution of the DMC is not considered in some standard channel models such as the 3GPP-SCM [81], ITU-R M.2135 channel model [82], and WINNER II channel model [83]. Therefore, it is of immense importance to analyze the contribution of the DMC to the total received power in order to decide whether or not to include the DMC in the channel model.

[2] SMCs also includes the LoS component.

It has been found in several studies that the DMC carries a significant fraction of the total measured channel power. Based on indoor measurements, the authors in [79] have found that DMC accounts for 10 %-95 % of the measured channel power. The fractional power of the DMC is up to 70 % in an industrial environment [84], and between 10 %-90 % in an outdoor environment [80]. In the following, the power contribution of the DMC for the three scenarios in the urban environment is calculated.

Having the SMCs identified and extracted in Section 4.5.1, the impulse response that corresponds to the LoS component and the SMC, $\mathbf{H}_{\mathrm{SMC}}$, is reconstructed based on the estimated parameters. The impulse response of the DMC, $\mathbf{H}_{\mathrm{DMC}}$, is then obtained by subtracting the SMC impulse response from the measured CIR, $\mathbf{H}_{\mathrm{meas}}$:

$$\mathbf{H}_{\mathrm{meas}} = \mathbf{H}_{\mathrm{SMC}} + \mathbf{H}_{\mathrm{DMC}} \quad . \tag{4.59}$$

The total received power together with the power carried by SMC and DMC as a function of distance are depicted in Figure 4.33 for the three scenarios. It is clear from Figure 4.33 that the overall power is decaying with Tx-Rx distance.

In the first scenario (Figure 4.33a), the LoS is blocked by buildings when the distance is larger than approximately 32 m. Therefore, the DMC power dominates the SMC power and it is up to 10 dB above the power of the SMC. As the vehicle and the cyclist approach the collision point, the SMC power increases significantly and reaches up to 16 dB above the power of the DMC. Note that this increase in the SMC power is due to the strong LoS and the reflections originated from nearby buildings and parked vehicles. It has also been found that an increase in the SMC power is often accompanied with an increase in the DMC power. This can be explained by the fact that when a specular reflection occurs, more DMC will be originated from the same reflecting object due to its roughness in agreement with the findings reported in [85].

In Scenario 2 (Figure 4.33b), the cyclist is moving in the same direction as the vehicle and the direct link between the vehicle and the cyclist repeatedly changes between LoS and OLoS situations due to obstruction by parked vehicles. Therefore, the total received power and the SMC power experience rapid variations. The power of the DMC is approximately up to 10 dB below SMC during the whole scenario.

Similar fluctuations are seen in Scenario 3 (Figure 4.33c). The DMC power is also up to 10 dB below the SMC power with an exception at distance between 10 − 25 m at which the power carried by the DMC is in the order of 2 − 4 dB above SMC. This can be explained by the fact that the LoS between the vehicle and the pedestrian as well as the SMC undergo strong attenuation due to obstruction by parked vehicles in the vicinity of the collision point.

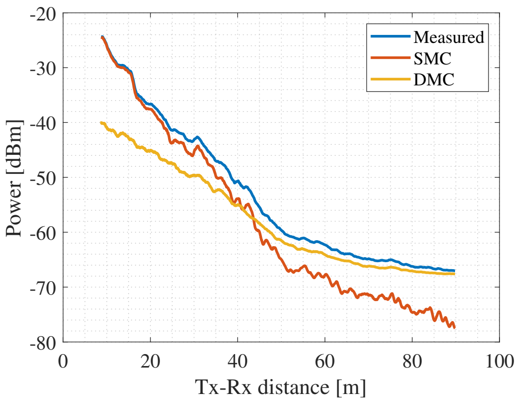

(a) Scenario 1

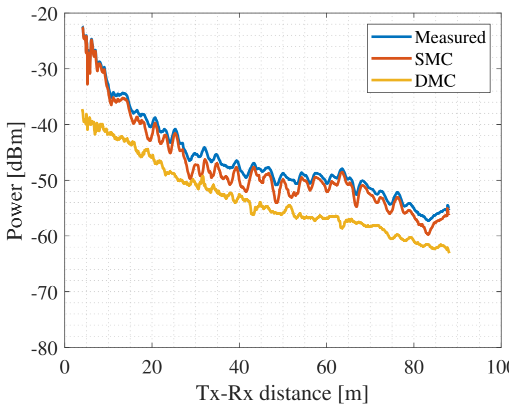

(b) Scenario 2

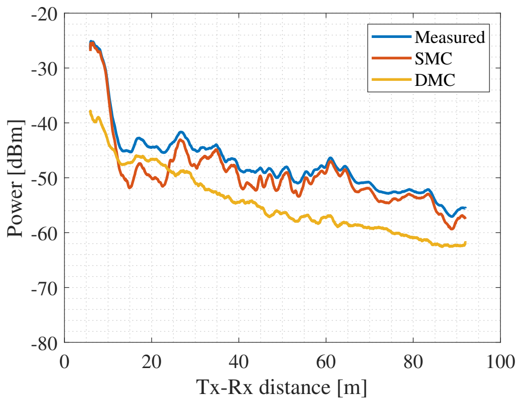

(c) Scenario 3

Figure 4.33: Total received power and power carried by the SMC and DMC as a function of Tx-Rx distance for the three scenarios in the urban environment.

An important aspect of modeling the DMC is the fractional DMC power $\hat{f}_{\mathrm{DMC}}$, i.e., the percentage of the DMC power contribution in the total received power:

$$\hat{f}_{\mathrm{DMC}} = \frac{P_{\mathrm{DMC}}}{P_{\mathrm{DMC}} + P_{\mathrm{SMC}}} \times 100\,\%, \tag{4.60}$$

where P_{DMC} and P_{SMC} are the average power carried by DMC and SMC respectively.

Figure 4.34 presents the fractional DMC power $\hat{f}_{\mathrm{DMC}}$ calculated with Equation (4.60) for the three scenarios. It can be seen in Figure 4.34 that the fractional DMC power in the first scenario exceeds 40 % and reaches up to 90 % of the total received power in NLoS situation at distances larger than approximately 32 m. As the vehicle and the cyclist are moving toward the intersection, the contribution of the DMC to the total received power decreases to reach approximately 5 % at the collision point.

In the second scenario, the fractional DMC power varies between 15 %-40 %. The variations are aligned with the variation of the SMC power in Figure 4.33b. The contribution of the DMC decreases to around 5 % at the collision point due to the strong LoS component, which usually carries most of the transmitted power.

Similar to the second scenario, the fractional DMC power in the third scenario represents from 15 % to 40 % of the total received power at distances larger than 25 m. A rapid increase to around 60 % shortly followed by a sudden drop to around 10 % prior to the collision is observed. Note that these results are in agreement with the results reported in [80].

From the results it becomes clear that the amount of the fractional DMC power depends on the link shadowing condition. Therefore, it is larger in NLoS than in OLoS and LoS situations. An increase of the fractional power can be mainly attributed to the decreased power of the LoS component due to obstruction by, e.g., buildings, parked and moving vehicles, etc. Similarly, the smaller amount of DMC power in LoS situation is probably due to the existence of a dominant LoS component and strong specular reflections.

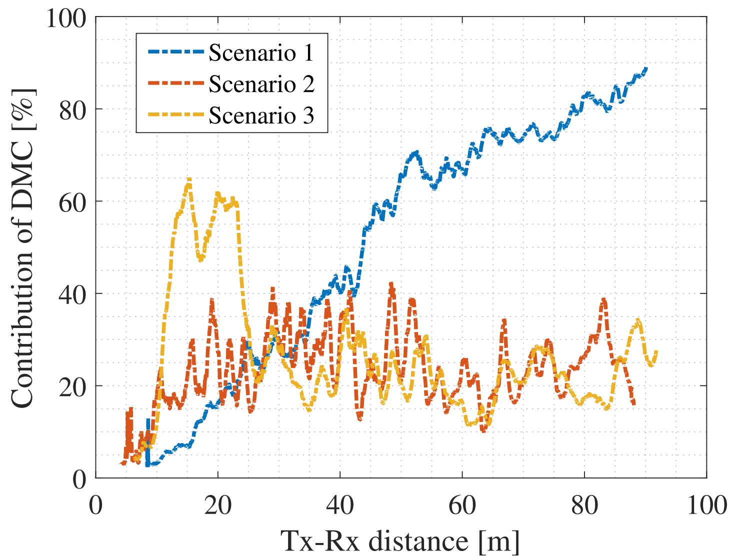

Figure 4.34: The fractional DMC power $\hat{f}_{DMC}$ as a function of Tx-Rx distance calculated by Equation (4.60) for the three scenarios in the urban environment.

4.8 Summary

This chapter addresses several aspects of channel modeling based on measurements in both open-field and urban environments. The presented results and methods in this chapter have been published in [16, 17, 22, 23, 24, 25].

Path loss models for the measured scenarios in open-field environments are proposed. The two-ray model is found to provide a good fit to the measured path loss in LoS scenario with static tripod. In Scenario 2, rapid fluctuations of the measured path loss are observed. These fluctuations are the result of the MPC originated by the human body. Further, the moving human body also results in dynamic antenna height and position. Due to the shadowing effect caused by the crowd around the Rx in Scenario 3, the measured path loss value is $5-10\,\text{dB}$ larger than the LoS case. In Scenario 4, the obstruction of the LoS by parked vehicles causes an extra loss between $10-20\,\text{dB}$ depending of the size of the parked vehicle. Log-distance path loss models are proposed for Scenario 2, Scenario 3, and Scenario 4. Further, the spatial correlation of shadow fading for Scenario 1 and Scenario

4 of the open-field environment is investigated. First, to prove the stationarity assumption, the SF is put under test, namely, the MRA test. After passing the stationarity test, the autocorrelation functions of the shadow fading are estimated and modeled by three different theoretical autocorrelation function models. The results show that the exponential decaying sinusoid model provides the best match to the empirical autocorrelation function in all scenarios. To study and model the aforementioned loss in the received power due to obstruction of LoS by parked vehicles in Scenario 4, a 3D ray tracing tool is developed. The measured path loss within the obstruction region is compared with the modeled path loss using the combined two-ray path loss model and the multiple knife-edge diffraction model. Despite its simplicity, the proposed model is able to provide a good match for the measured path loss.

From the measurements in the urban environment, single and dual-slope log-distance path loss models are proposed. From the results, it is noticed that due to the obstruction by buildings in Scenario 1, an extra loss of up to 25 dB is experienced when compared to the free space path loss. Moreover, due to obstruction of parked vehicles, a diffraction loss between 5 dB and 15 dB is observed in Scenario 2, and Scenario 3, respectively.

The non-stationarity of the V2VRU channel in the urban environment is assisted by estimating the generalized local scattering function and its collinearity based on the channel measurement data. It is found that in all scenarios, at the shortest Tx-Rx distance, i.e., at the collision point, the stationarity distance suddenly drops. This results from the sudden change in the Doppler domain because the LoS component shifts from positive to negative Doppler at the moment of passing the collision point. Furthermore, a pattern of consecutive highs and lows is observed, which can be explained by the appearance and disappearance of the LoS due to the blockage by the parked vehicles. Generally, a stronger LoS component leads to a large stationarity distance. Moreover, not only the power of the LoS but also its variation affects the stationarity distance. It is noticed that the that larger and more rapid the power variations of the LoS component the shorter the stationarity distance. The estimated average stationarity distances are 2.13 m, 5.25 m, and 3.58 m for Scenario 1, Scenario 2, and Scenario 3, respectively.

The KEST algorithm is employed to estimate the parameters of the MPCs. Unlike the open-field, in the urban measurements, the CIR is highly cluttered. It can be deduced based on the long lifetimes that all paths in the estimated CIR in the open-field are due to specular reflections. On the other hand, in the urban scenario, not only specular reflections but also DMCs can be seen. Therefore, the SMCs are extracted from the estimated time-variant CIR. For this purpose, a novel method to separate SMCs and DMCs based on their number of neighboring MPCs that have delay difference less or equal a specific threshold is proposed. Next, an MCD-based tracking algorithm that utilizes the estimated delay and magnitude for tracking the SMCs is proposed. Having the SMCs tracked over time, each SMC is related to a physical scatterer in the propagation environment. Localization of the scatterers in all scenarios is done using a joint delay-Doppler estimation algorithm. The estimated positions of the scatterers are then used to estimate the AoD and AoA.

Finally, the contribution of the DMC to the total received power is calculated. From the results it becomes clear that the amount of the fractional DMC power depends on the link shadowing condition. Therefore, it is larger in NLoS than in OLoS and LoS situations. An increase of the fractional power can be mainly attributed to the decreased power of the LoS component due to obstruction by, e.g., buildings, parked and moving vehicles, etc. Similarly, the smaller amount of DMC power in LoS situation is probably due to the existence of a dominant LoS component and strong specular reflections. It is found that the DMC carries up to 5 % of the total received power in LoS condition. However, in OLoS the fractional DMC power is approximately between 15 % and 40 % and it can reach 90 % in NLoS condition.

Having the SMCs extracted, tracked over time, and their scatterers localized, a full parameterization of the GSCM channel model becomes feasible. The next chapter will address the estimation of the model parameters based on the estimated amplitude, delay, and angles of the SMCs.

5 Channel Model Parameterization

For developing a GSCM for V2VRU communication following WINNER II channel model, the LSPs need to be estimated. In this chapter, the LSPs, introduced in Section 2.4.1, are estimated in the power and delay domain, i.e., SF, DS, and KF, and in the angular domain, i.e., ASD, and ASA. In order to maintain the spatial correlation of the LSPs observed in the measured channel, the autocorrelation of these LSPs is analyzed and the correlation distances are calculated. Furthermore, to ensure the spatial consistency, the cross-correlation coefficients among the LSPs are calculated. The model parameters are then used as an input to the channel simulator.

5.1 Large Scale Parameters

In this section, the estimation of the first- and second-order statistics of the LSPs are provided. The LSPs are estimated from the specular MPC parameters, i.e., the power, delay, and angles, that were previously estimated from the measurement data in Section 4.5 and from scatterer locations in Section 4.6. The LSPs are then fitted to log-normal distributions. These distributions control the behavior of the modeled channel. Table 5.1 summarizes the proposed LSPs of the channel model.

Due to the non-stationarity of the channel, the channel is divided into regions, within which the WSS assumption holds. The LSPs and their correlations are evaluated within these regions using a sliding average window of length of $15\,\lambda$ (0.86 m). The length of the window, i.e., the stationarity distance, is found to be valid for all scenarios based on the non-stationarity analysis in Section 4.4 (see Figure 4.15). Note that, this sliding averaging window is different from the sliding average window of length of $10\,\lambda$ used for removing the small scale fading in Sections 4.1 and 5.1.1.

The KF and DS are found to vary significantly when the propagation condition, i.e, LoS, OLoS, and NLoS, changes. Therefore, when estimating the KF and DS, the data set is divided into two parts based on the propagation condition. The appearance of the LoS starts at an average Tx-Rx distance of 15 m in Scenario 1, and at 9 m in both Scenario 2 and Scenario 3. Unlike the KF and DS, the SF, ASD, and ASA are estimated for the whole experiment with no distinction between LoS and OLoS/NLoS situations.

5.1.1 Shadow Fading

As explained in Section 4.1, the measured path loss is expressed in logarithmic scale as a sum of two components, namely, the the distance-dependent path loss model and the SF (see Equation (4.5)). To remove the effect of fast fading from the measured path loss, a sliding window of length $10\,\lambda$ is used. The SF is usually modeled as a normally-distributed random variable with zero mean and a standard deviation. In all three scenarios, the SF is estimated for the whole experiment, i.e., the data set is not divided based on the propagation condition.

Figure 5.1 shows the results for each scenario. Each plot depicts the CDF curves of the measured SF and its log-normal fit. Positive SF values indicate a larger overall path loss, while negative SF values mean a smaller overall path loss. Even though minor differences can be noticed in Scenario 3 between the CDF of the measured SF and its log-normal fit, it can be seen that the log-normal distribution perfectly fits the distribution of the measured SF with a zero mean and a standard deviation σ.

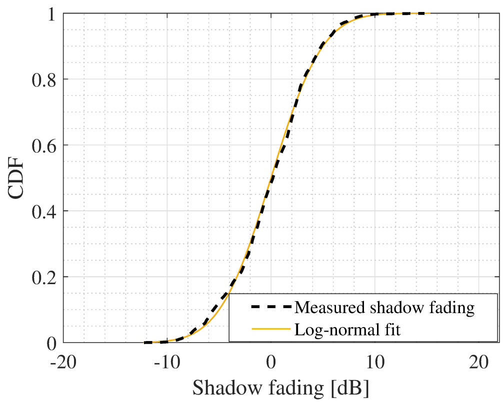

(a) Scenario 1

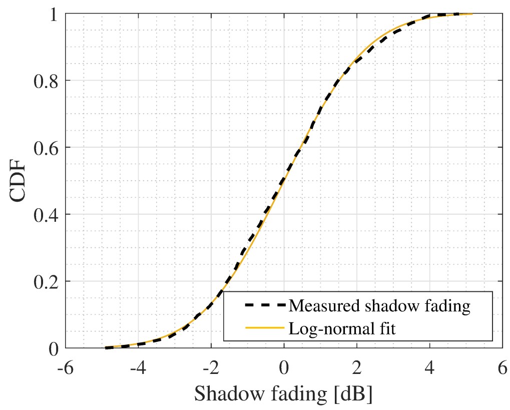

(b) Scenario 2

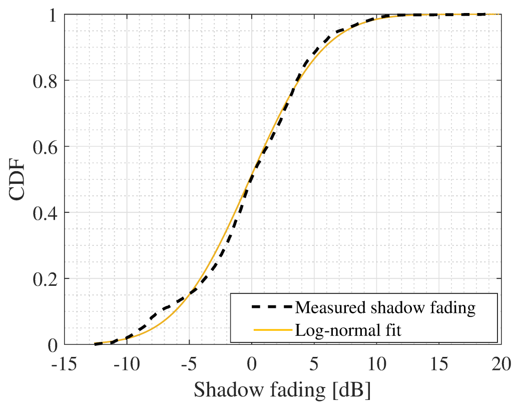

(c) Scenario 3

Figure 5.1: CDFs of measured SF and the log-normal fit for the three scenarios in urban environment.

5.1.2 Delay Spread

The DS is widely used to statistically describe delay characteristics of wireless channels. Due to the multipath propagation, the Rx receives several copies of the transmitted signal. Each copy arrives from different direction with different gain and delay. The delay dispersion of the propagation paths is described by the DS metric. The DS in the snapshot at time t is calculated from the estimated parameters of the SMCs described in Section 4.5 according to [86]

$$\sigma_\tau = \sqrt{\frac{\sum\limits_{i=0}^{N(t)-1} P_i \tau_i^2}{\sum\limits_{i=0}^{N(t)-1} P_i} - \bar{\tau}^2}, \tag{5.1}$$

where $\bar{\tau}$ is the mean excess delay calculated as in [86]

$$\bar{\tau} = \frac{\sum\limits_{i=0}^{N(t)-1} P_i \tau_i}{\sum\limits_{i=0}^{N(t)-1} P_i}, \tag{5.2}$$

and where P_i and τ_i are the power and delay of the i-th MPC, and $N(t)$ is the number of MPCs at time t. The DS is calculated for each scenario from all measurement runs and then fitted to a log-normal distribution with a unit of $\log_{10}(s)$.

Figure 5.2 shows the CDF of the measured DS alongside the log-normal fit for the three scenarios. Each scenario is divided into two parts according to the propagation condition. Therefore, each plot includes CDFs for two propagation conditions. In Scenario 1, the DS has a mean value of 36 ns in NLoS case. As the vehicle and the cyclist are approaching the intersection, the mean value drops to 7.4 ns. In Scenario 2, the mean value of the DS decreases from 25 ns to 6.4 ns when moving from OLoS case to LoS case. Similarly, in Scenario 3, the mean values are 24 ns and 8.1 ns in OLoS and LoS cases, respectively. Generally, the DS tends to decrease when the power of LoS path increases. It can be observed, in all scenarios, that the CDF of

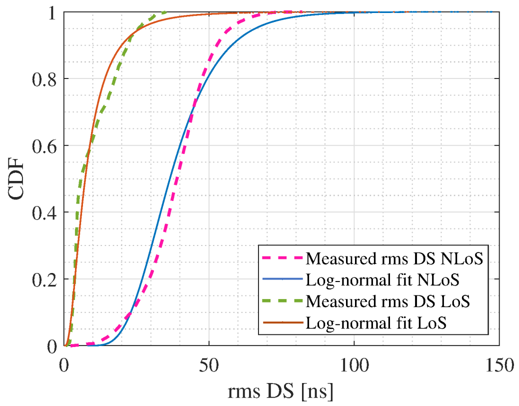

(a) Scenario 1

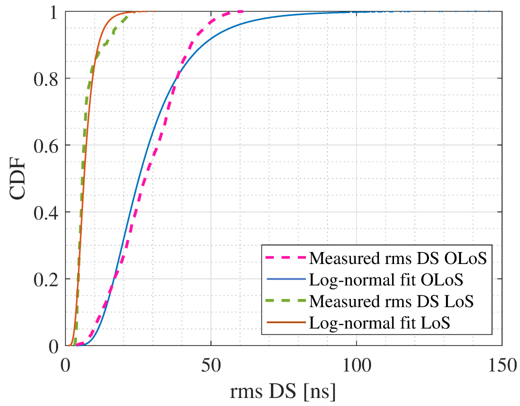

(b) Scenario 2

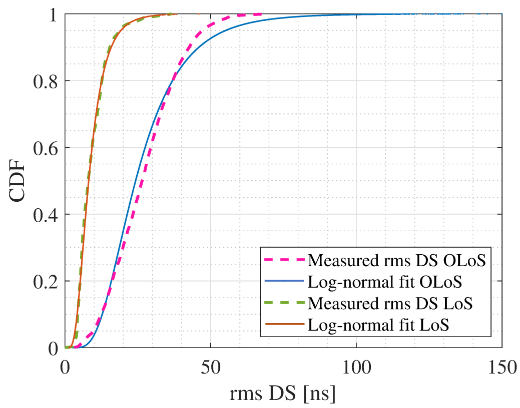

(c) Scenario 3

Figure 5.2: CDFs of measured DS and the log-normal fit for the three scenarios in urban environment.

the log-normal fit in OLoS and NLoS has a tail with larger DS than that of the measured one. Nevertheless, the log-normal distribution provides a good fit to the measured DS.

5.1.3 Narrowband K-factor

The KF is an important parameter that provides an indication of the energy proportion of the MPCs and hence quantifies the multipath richness of the communication channel. The KF is defined as the ratio of the energy of the dominant component that consists of the LoS component and the unresolved ground reflection to the energy of all other components. In literature, several approaches are proposed to estimate the KF. A widely used technique to estimate the KF from the measured CIR is introduced in [87] based on the method of moments (MoM). However, as stated earlier, the narrowband KF in this thesis is calculated for each measurement snapshot from the estimated parameters of the SMCs and it is calculated according to [86]

$$K = \frac{P_{\mathrm{LoS}}}{P - P_{\mathrm{LoS}}} \quad , \tag{5.3}$$

where P_{LoS} is the power of the LoS path, and P is the total power. Typically the KF is in dB and it is modeled by a log-normal distribution.

Figure 5.3 shows the CDFs of the measured KF and its log-normal fit for the three scenarios. Note that, the KF is not estimated for NLoS condition in Scenario 1. It can be seen that the log-normal distribution provides a perfect fit for the measured KF. The KF in LoS case for the three scenarios has comparable mean values with 15.02 dB, 16.22 dB, and 17.32 dB for Scenarios 1, 2, and 3, respectively. Similarly, in OLoS case the mean values of the KF are 5.34 dB and 6.44 dB for Scenario 2 and Scenario 3, respectively. The main reason for the larger KF in during the LoS compared to the OLoS case is the the existence of a unobstructed strong LoS path. In OLoS case, the LoS path is obstructed by parked vehicles and therefore suffers from an attenuation due to the diffraction loss, as explained in Section 4.3.

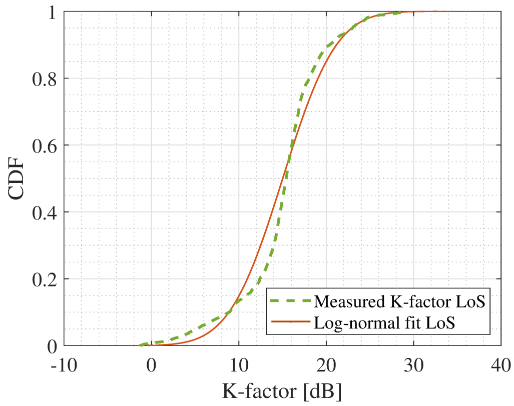

(a) Scenario 1

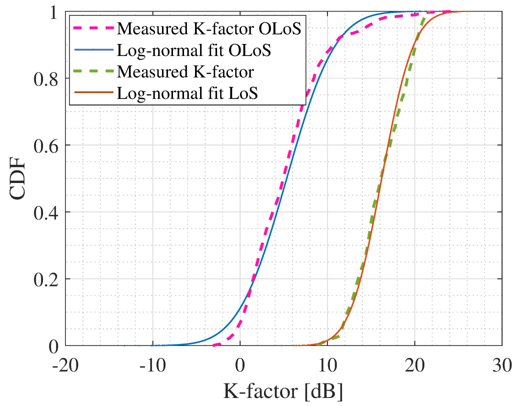

(b) Scenario 2

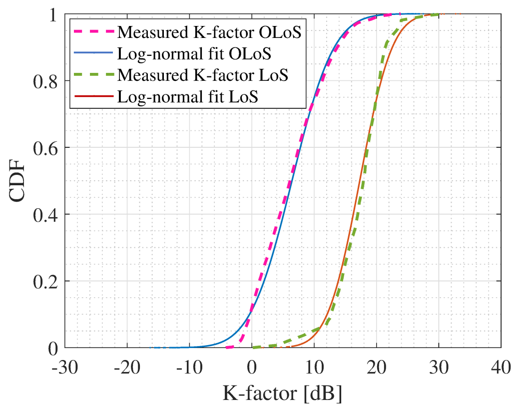

(c) Scenario 3

Figure 5.3: CDFs of measured KF and the log-normal fit for the three scenarios in urban environment.

5.1.4 Angular Spread

The AS is the parameter that describes the dispersion of propagation paths in the angular domain, i.e., it measures how the multipath power is spread out in the spatial domain. The AS is calculated utilizing the paths angles, i.e., AoD and AoA, and the path gains. The AoA and AoD are calculated from the scatterers locations, which were estimated in Section 4.6. The reference angle, i.e., the angle 0° is set to be the angle between the Tx and the Rx. The ASD and ASA are calculated in each measurement snapshot as in [88]

$$\sigma_\phi = \sqrt{\frac{\sum\limits_{i=0}^{N(t)-1} \left(\xi\left(\phi_i - \bar{\phi}\right)\right)^2 P_i}{\sum\limits_{i=0}^{N(t)-1} P_i}}\,, \tag{5.4}$$

where P_i and ϕ_i are the power and angle of the i-th MPC, function $\xi\,(.)$ maps angles to (-180, 180) degree, and the power weighted mean angle $\bar{\phi}$ is given by

$$\bar{\phi} = \frac{\sum\limits_{i=0}^{N(t)-1} \xi\left(\phi_i\right) P_i}{\sum\limits_{i=0}^{N(t)-1} P_i}\,. \tag{5.5}$$

The ASD and the ASA are estimated for the whole experiment because, unlike the DS and KF, the difference in angle spread in different propagation cases, i.e., LoS, OLoS, and NLoS is found to be insignificant. Figure 5.4 presents the CDFs of the measured ASD together with its log-normal fit. The measured ASD follows the log-normal fit in all three scenarios with minor mismatch. The mean ASD values are 5.49°, 7.24°, and 10.96° for Scenarios 1, 2, and 3, respectively. The CDFs of the ASA are plotted in Figure 5.5 which also perfectly follow the log-normal distribution with mean values of 10.47°, 10.72°, and 12.88° for Scenarios 1, 2, and 3, respectively.

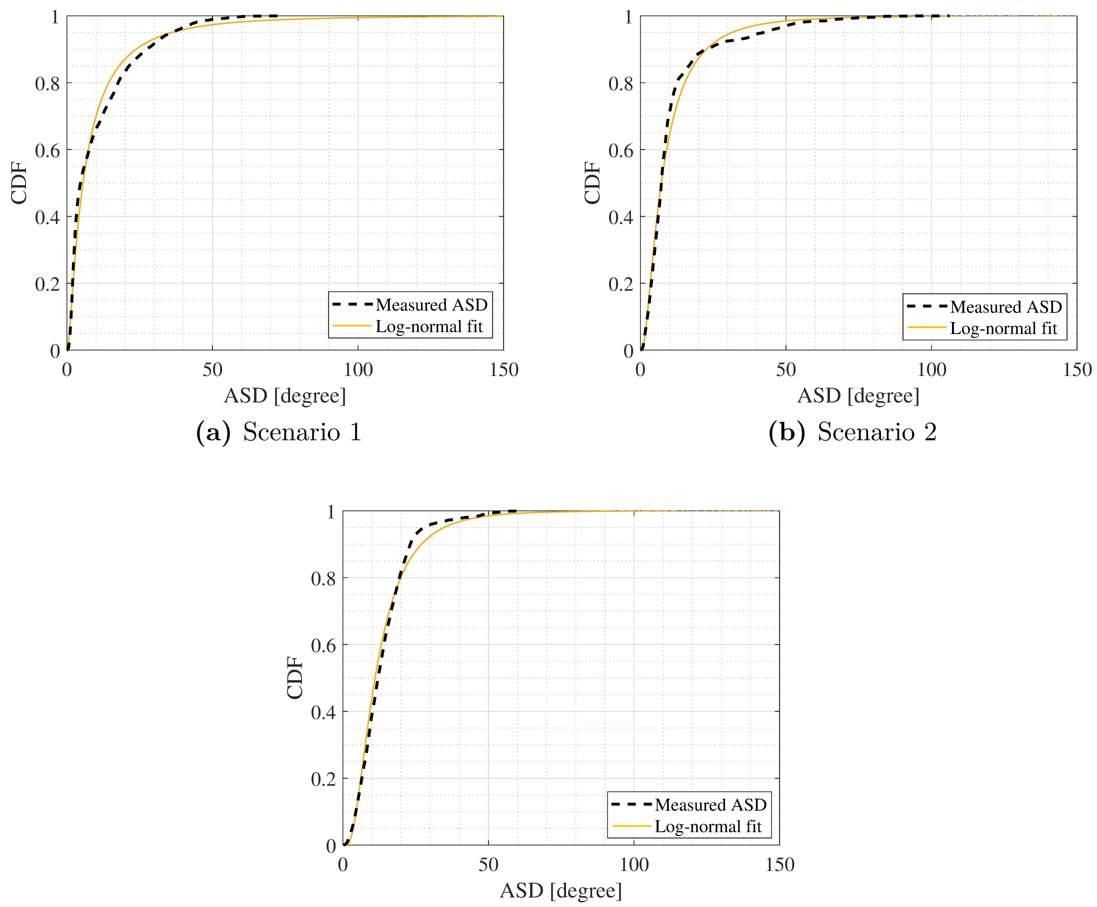

(a) Scenario 1

(b) Scenario 2

(c) Scenario 3

Figure 5.4: CDFs of measured ASD and the log-normal fit for the three scenarios in urban environment.

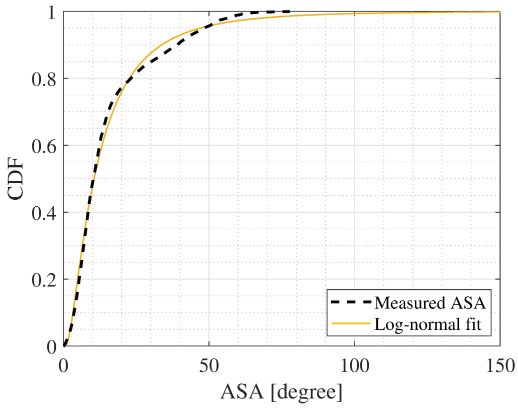

(a) Scenario 1

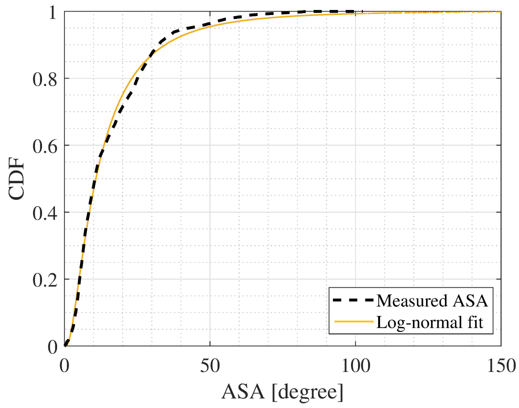

(b) Scenario 2

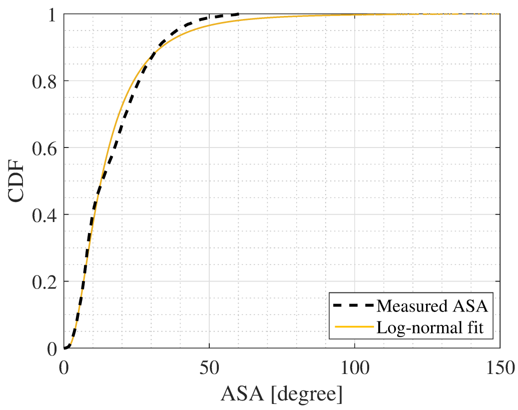

(c) Scenario 3

Figure 5.5: CDFs of measured ASA and the log-normal fit for the three scenarios in urban environment.

5.2 Correlation Distances

The correlation distance of a LSP indicates how long the channel can be assumed stationary for this specific LSP. The correlation distance is used as a model parameter to maintain the spatial correlation of the LSP observed in the measured channel. It is employed in the generation the correlated 2D map of the LSP by determining the length of the channel segment, or the length of the traveled distance, in these maps as discussed in Section 2.4.2. The correlation distance is calculated from the autocorrelation function of the evaluated LSP as follows

$$r(\Delta d) = \mathrm{E}\left[x(d)x(d+\Delta d)\right], \tag{5.6}$$

where $\mathrm{E}[.]$ denotes the expected value, d is the distance between Tx and Rx, Δd is the change of the Tx-Rx distance, and x is the LSP under evaluation in log domain. The correlation distance d_c is defined as the value of Δd at which the value of the normalized autocorrelation function drops to e^{-1}. Note that, in case the normalized autocorrelation function has a value of e^{-1} at different values of Δd, the shortest Δd is the correlation distance (see Figure 5.6). Table 5.1 summarizes the correlation distances of the LSPs in all scenarios.

The results show that the correlation distances of the KF and DS during LoS part are much shorter than in NLoS/OLoS part. This is attributed to the fact that the length of the LoS part, within which the autocorrelation function is evaluated, is limited to only few meters prior to the collision point, i.e., less than 10 m in Scenario 1 and less than 5 m in Scenario 2 and Scenario 3. Figure 5.6 shows an example of the normalized autocorrelation function of the KF in Scenario 3 for both LoS and OLoS parts. It can be noticed that the autocorrelation function within this distance approximately matches the autocorrelation function during OLoS part. Similar agreement is also found for DS in all scenarios. The findings show that the smaller correlation distance in LoS part is only due to the shorter distance within which the autocorrelation function is evaluated and, hence, it does not imply less correlation.

As can be seen from Table 5.1, on the one hand, the KF, DS, ASD, and ASA show relatively high spatial correlation which implies slow change in their values

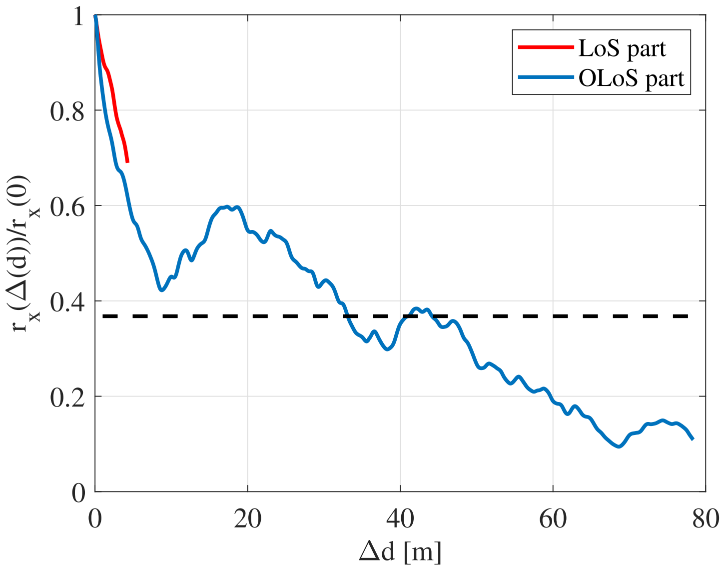

Figure 5.6: Example of the normalized autocorrelation function of the KF in Scenario 3 for both LoS and OLoS parts. The black dashed line marks the value of e^{-1} at which the correlation distance is calculated.

over time. On the other hand, the SF experiences less spatial correlation which can be explained by the intermittent blockage of the LoS by parked vehicles.

Parameters		**Scenario 1**		**Scenario 2**		**Scenario 3**	
		LoS	**NLoS**	**LoS**	**OLoS**	**LoS**	**OLoS**
SF [dB]	μ	0	0	0	0	0	0
	σ	3.90	3.90	1.80	1.80	4.69	4.69
Corr.distance [m]	d_c	8.20	8.20	2.27	2.27	7.60	7.60
K-factor [dB]	μ	15.02	N/A	16.22	5.34	17.32	6.44
	σ	4.81	N/A	2.88	4.38	4.09	5.31
Corr.distance [m]	d_c	8.01	N/A	4.42	30.58	4.23	26.97
DS [$\log_{10} s$]	μ	-8.13	-7.44	-8.19	-7.60	-8.09	-7.62
	σ	0.34	0.16	0.19	0.21	0.23	0.22
Corr.distance [m]	d_c	8.97	49.69	4.42	70	4.64	57.88
ASD [$\log_{10}$ °]	μ	0.74	0.74	0.86	0.86	1.04	1.04
	σ	0.50	0.50	0.39	0.39	0.30	0.30
Corr.distance [m]	d_c	37.11	37.11	63.23	63.23	55.61	55.61
ASA [$\log_{10}$ °]	μ	1.02	1.02	1.03	1.03	1.11	1.11
	σ	0.4	0.4	0.39	0.39	0.33	0.33
Corr.distance [m]	d_c	48.95	48.95	66.17	66.17	54.48	54.48

Table 5.1: Large scale parameter distributions and correlation distances.

5.3 Cross-correlation Parameters

In order to ensure channel spatial consistency, the cross-correlations between all LSP pairs are needed. This metric describes the linear dependency between the LSPs. The cross-correlation coefficient is given by

$$\rho_{x,y} = \frac{\sum\limits_{m=1}^{M} \left(x(m) - \bar{x}\right) \left(y(m) - \bar{y}\right)}{\sqrt{\sum\limits_{m=1}^{M} \left(x(m) - \bar{x}\right)^2 \sum\limits_{m=1}^{M} \left(y(m) - \bar{y}\right)^2}} \quad , \tag{5.7}$$

where x and y are the measured sequences of the two LSPs pairs with length M, and $\bar{x}$ and $\bar{y}$ are the sample means of x and y, respectively.

Cross-correlation coefficients take values from -1 to 1. A negative coefficient indicates a decrease in parameter x if parameter y increases and vice versa. Positive coefficient means that x and y increase and decrease simultaneously. When the coefficient is zero there is no dependency between the two parameters. Table 5.2 shows the cross-correlation coefficients between all pairs of LSPs for all scenarios in the urban environment.

The SF is found to be positively correlated with the KF while negatively correlated with the DS, i.e., when the SF increase, the K-factor increases and the DS decreases. In all scenarios, the DS and KF have a strong negative correlation as expected. A positive correlation in all scenarios between the ASD and ASA is also observed. The ASD cross-correlations with SF, KF, and DS in the three scenarios are not consistent. For example, the ASD has positive correlation of 0.28 with the SF in Scenario 1, negative correlation of -0.21 in Scenario 2, and no correlation in Scenario 3. Nevertheless, the ASD shows weak or no dependency on the SF, KF and DS. Similarly, the ASA shows no correlation with the KF and DS in all scenarios, while it has a weak dependency on the SF in Scenarios 2 and 3.

Cross-correlation		SF	KF	DS	ASD	ASA
Scenario 1	SF	1	0.5	-0.42	0.28	-0.07
	KF		1	-0.86	0	-0.01
	DS			1	-0.33	-0.04
	ASD				1	0.58
	ASA					1
Scenario 2	SF	1	0.35	-0.3	-0.21	-0.36
	KF		1	-0.87	0.25	-0.01
	DS			1	-0.13	0.07
	ASD				1	0.63
	ASA					1
Scenario 3	SF	1	0.63	-0.51	-0.07	-0.26
	KF		1	-0.85	0	-0.1
	DS			1	0.02	-0.07
	ASD				1	0.5
	ASA					1

Table 5.2: Estimated cross-correlation coefficients.

5.4 Scaling Coefficients and Number of MPCs

As stated in Section 2.4.1 and Section 2.4.2 (Step C.), the scaling coefficients, also called the proportionality factors, are used to scale path delays and angles to insure that the differences in the spreads are reflected in the powers. The scaling coefficient of the delay g^{DS} is defined as the ratio between the standard deviation of the path delays and the RMS DS. Similarly, the scaling coefficients of the angles, g^{ASD} and g^{ASA}, are defined as the ratio between the standard deviation of the path angles and the AS [15]. Table 5.3 summarizes the mean values of scaling coefficients estimated from the measurement data in all scenarios.

Scaling coefficient	**Scenario 1**	**Scenario 2**	**Scenario 3**
g^{DS}	1.97	2.71	3.48
g^{ASD}	2.57	2.35	1.82
g^{ASA}	1.98	2.38	2.18

Table 5.3: Estimated scaling factors in all scenarios.

Based on the measurement data, the number of MPCs used in the channel simulations for all scenarios is set to 8 MPCs. However, we noticed that changing the number of MPCs has an insignificant impact on the simulated channels.

5.5 Summary

In this chapter, a full parametrization for the WINNER-type GSCM is proposed. The LSPs are estimated in log domain and fitted to the log-normal distribution. The results show that the log-normal distribution provides a good fit to the measured LSPs in all scenarios. Furthermore, the spatial correlation of the LSPs are evaluated and their correlation distances are calculated. It can be noted that the SF experiences relatively low correlation. However, all other LSPs show high correlation indicating slow change in their statistics over time. Moreover, to include the inter-dependency between all pairs of LSPs, the cross-correlation coefficients are provided.

The parameters estimated in this chapter together with the path loss models are used to generate synthetic channels. The proposed channel model is then validated by comparing the measured channels with the simulated synthetic channels in the next chapter.

6 Model Validation

This chapter presents the validation of the proposed channel model. The GSCM for V2VRU communications is validated by comparing the simulated channels with the measured channels. The simulated channels are generated by the WINNER-type QuaDRiGa simulator [40] described in Section 2.4.2. The model parameters are extracted from the measured channels and used as an input to the simulator. These parameters are, mainly, the path loss presented in Chapter 4, and the LSPs estimated in Chapter 5. The channel model is validated by comparing the distributions of the model parameters, extracted from the simulated channels, with their counterparts extracted from the measured channels and used as input to the proposed model. The model parameters extracted from the measurement are referred to as the model input. In addition to the distributions of the LSPs, the correlation distance of each LSP as well as the cross-correlation between each LSPs pair are also considered in the validation process.

The validation is performed using a group of 100 simulated channels produced by 100 simulation runs for each scenario. These simulation runs are carried out using Tx and Rx routes similar to the routes during the channel measurements. Therefore, the resulting simulated channel in each run has a similar number of snapshots as the measured channel. Furthermore, the channels are generated for a center frequency

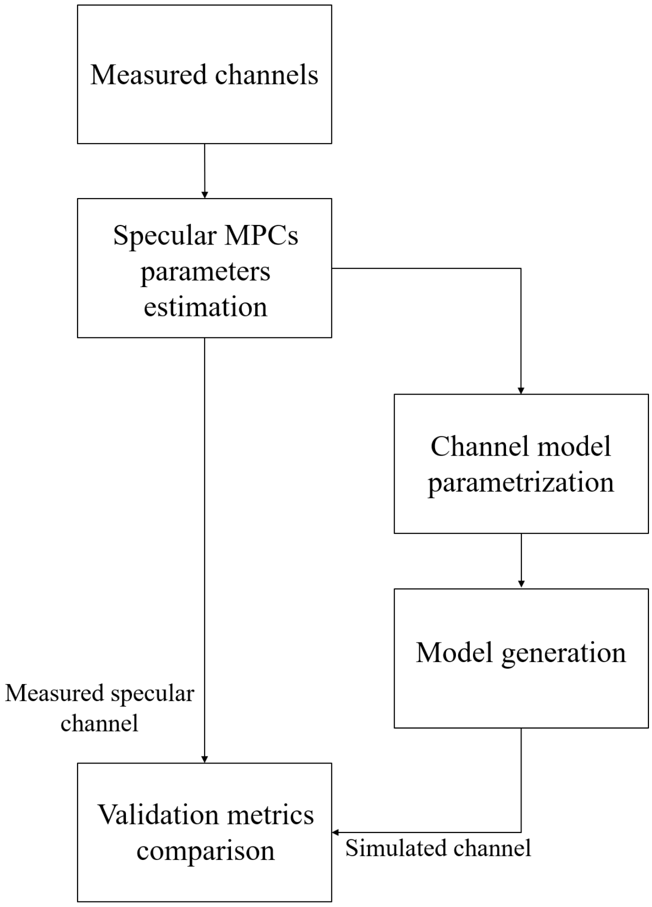

Figure 6.1: Channel model validation process.

of 5.2 GHz and a bandwidth of 120 MHz. It must be also noted that only specular MPCs are taken into account when estimating the model parameters and generating the simulated channels. The diffuse multipath are not taken into account in this model. Figure 6.1 shows the procedure for the channel model validation.

6.1 Simulated Channels and Path Loss

Figure 6.2 shows examples of measured and simulated CIRs for the three scenarios in urban environment. In all scenarios the Tx-Rx separation distance is approximately 100 m. In Scenario 1 (Figure 6.2a and 6.2b), the vehicle and the cyclist are approaching the collision point at the intersection while the LoS is completely obstructed by buildings. It can be seen that the LoS path starts to appear at approximately 23 m or 6.5 s in the measured CIR and at approximately 15 m or 7 s in the simulated channel. This difference is due to setting the Tx-Rx distance of the LoS appearance in the simulations to 15 m, which is the average distance extracted from all measurement runs in Scenario 1. As shown in both measured and simulated CIRs, the LoS path is accompanied by a group of strong MPCs. During NLoS, a weak path appears as a tail of the LoS path with a slightly larger delay than the geometric LoS (GLoS). A group of weak paths can also be recognized.

In Scenario 2 (Figure 6.2c and 6.2d), the cyclist is approaching the collision point while driving parallel to the vehicle. The LoS in both measured and simulated channels is partially obstructed by parked vehicles except at distances less than 9 m where a strong LoS can be noticed. In contrary to the LoS path, which has a propagation delay calculated in a deterministic manner from the positions of the Tx and Rx, the propagation delays of the SMCs depend on the locations of the scatterers which are randomly placed based on the the distributions of the AS. Therefore, we can not expect to generate simulated channels with SMCs identical to the measured ones.

In Scenario 3 (Figure 6.2e and 6.2f), the pedestrian is crossing the street while the vehicle is approaching the collision point. Similar to Scenario 2, the LoS path is partially obstructed by parked vehicles. A strong LoS appears prior to the collision accompanied with strong MPCs generated by scatterers located in the vicinity of the collision point. In all scenarios, it can be noticed that the SMCs during the LoS condition are more closely located nearby the LoS path than in the OLoS and NLoS conditions.

In order to validate that the proposed channel model produces accurate path loss or received power, the local mean path loss, calculated from all simulated channels, is compared with the path loss model presented in Figure 4.2 for each scenario. These proposed log-distance path loss models are used as an input to the channel simulator. As can be seen in Figure 6.3, in Scenario 1, the measured path loss is modeled by a single slope in LoS propagation condition with path loss exponent of 1.4 for distances up to 15 m from the collision point. At longer distances, up to 100 m, the propagation condition is NLoS and the path loss is modeled by a dual-slope path

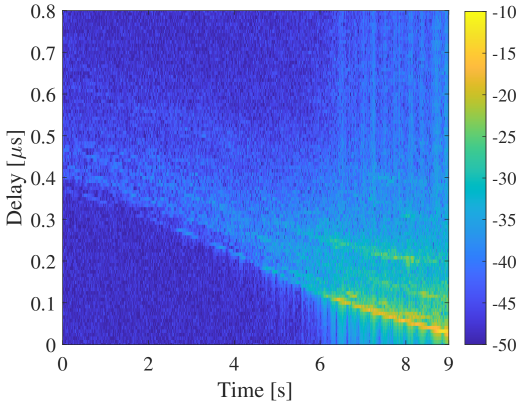

(a) Scenario 1 - measured

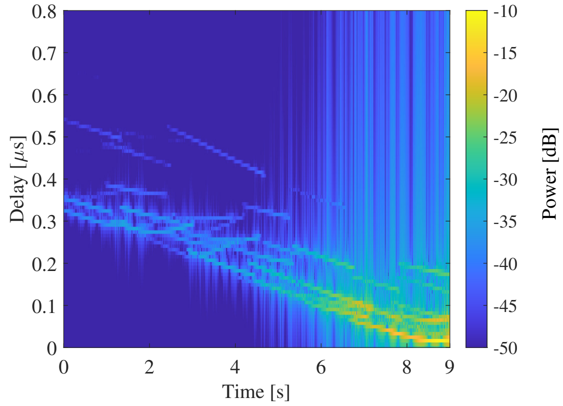

(b) Scenario 1 - simulated

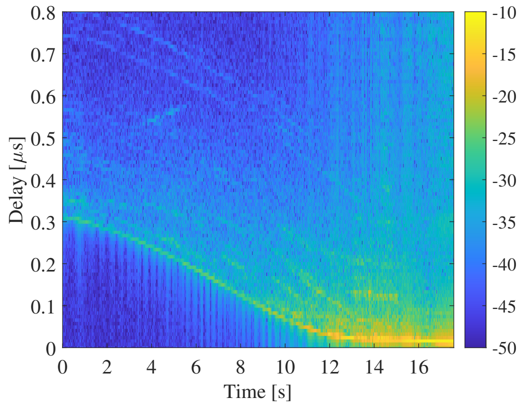

(c) Scenario 2 - measured

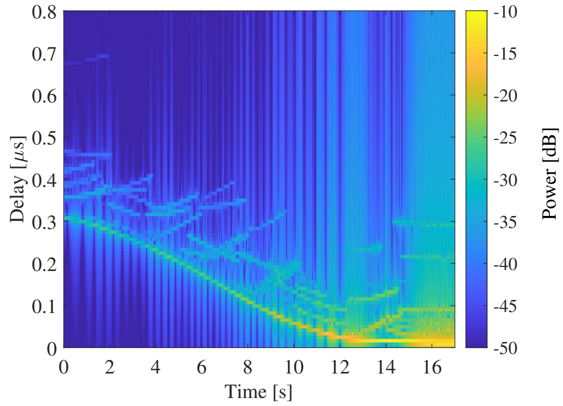

(d) Scenario 2 - simulated

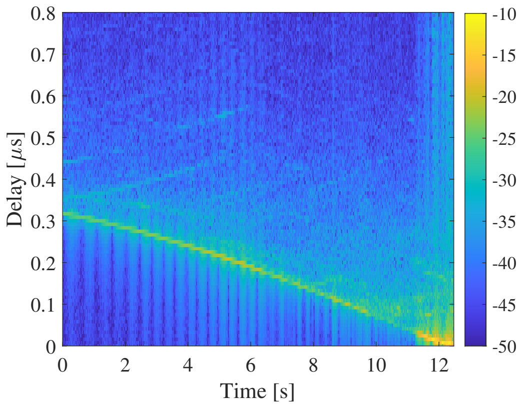

(e) Scenario 3 - measured

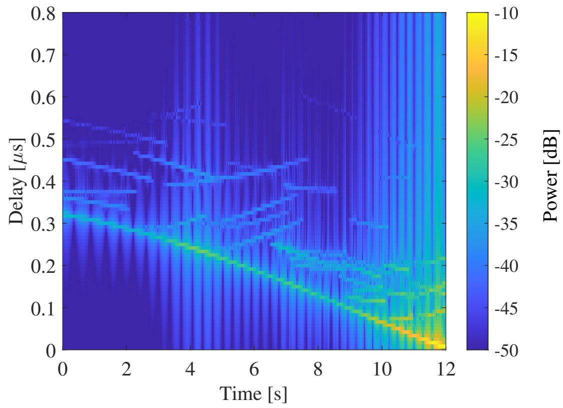

(f) Scenario 3 - simulated

Figure 6.2: Examples of measured and simulated channel impulse responses for the three scenarios in urban environment.

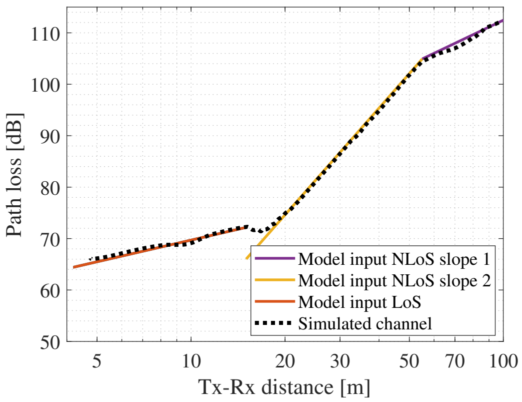

(a) Scenario 1

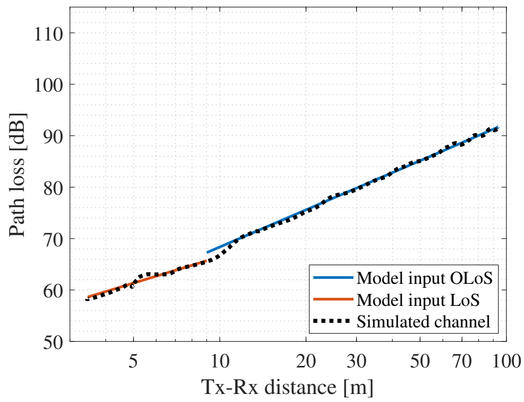

(b) Scenario 2

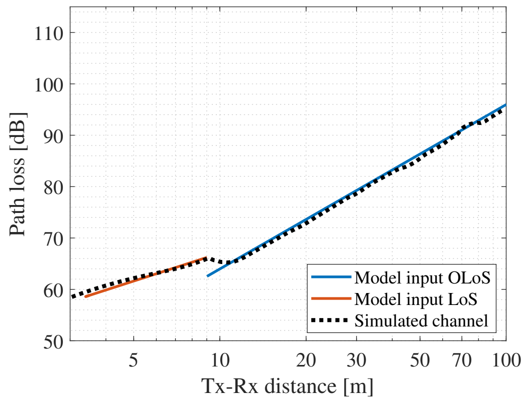

(c) Scenario 3

Figure 6.3: Comparison of the path loss for the three scenarios in urban environment.

loss with exponents of 6.9 and 2.9. In Scenario 2, path loss exponents of 1.7 and 2.4 were obtained in LoS and OLoS propagation conditions, respectively. Similar to Scenario 2, the path loss exponents in Scenario 3 are found to be 1.8 and 3.2 in LoS and OLoS conditions. For more details on the proposed model parameters (see Table 4.2).

Figure 6.3 depicts the results for the path loss validation in the three measured scenarios. Each plot includes two or three solid colored lines and a black dashed curve. The solid colored lines represent the model input of the path loss extracted from the measured channels with Tx-Rx distance (see Figure 4.2), while the dashed black curve is the local mean of the path loss obtained from the 100 simulated channels. It can be noted that the channel model clearly provides an almost perfect match in terms of path loss and received power in all three measured scenarios.

6.2 Large Scale Parameters

In this section, the distributions of the LSPs from the model input and the simulated channels are compared. The LSPs are estimated from the simulated channels in the same way they were estimated from the measured channels, as presented in Chapter 5, and then fitted to log-normal distributions. The mean and standard deviation values of the LSPs are summarized in Tables 6.1, 6.2, and 6.3.

6.2.1 Shadow Fading

Figure 6.4 depicts the results for the SF validation in the three measured scenarios. Each plot includes two CDF curves. The solid orange line represents the model input of the SF extracted from the measured channels, while the dotted black line shows the SF obtained from the simulated channels.

It can be noted that the match between the simulations and the model input is good for Scenario 1. The standard deviation values of the SF are 3.9 dB and 3.35 dB for the model input and simulated channels, respectively. In Scenario 2, some mismatch can be seen. The estimated standard deviation from the simulated channels is 1 dB larger than the SF of the model input. Similar mismatch is observed in Scenario 3. The simulated channels produce larger SF with a standard deviation of 6.31 dB compared to 4.69 dB in the model input. It has been found that the observed mismatch occurs due the final scaling of the path powers by the KF in Equation (2.26). In Scenario 1, the impact of the KF on the SF is less than in

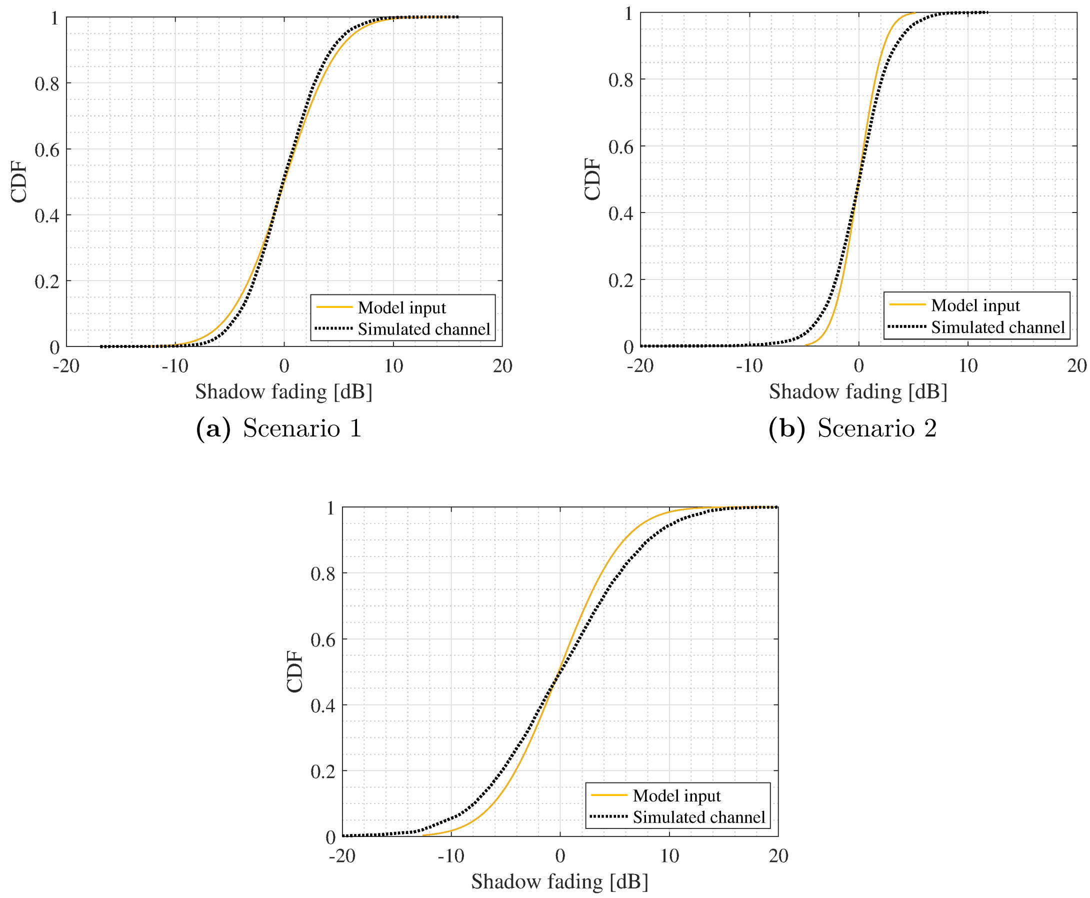

(a) Scenario 1 **(b)** Scenario 2 **(c)** Scenario 3

Figure 6.4: Comparison of the distribution of the shadow fading for the three scenarios in urban environment.

Scenario 2 and Scenario 3 because the path powers are only scaled by the KF in the channel segments with a LoS condition. However, in Scenario 2 and Scenario 3 the path powers are scaled by the KF in all channel segments which may explain the larger mismatch.

6.2.2 Delay Spread

The RMS DS is widely used to statistically describe delay characteristics of wireless channels. The DS is modeled as a log-normal distribution with unit of $\log_{10}(s)$. It is evaluated with distinction between LoS, OLoS, and NLoS propagation conditions.

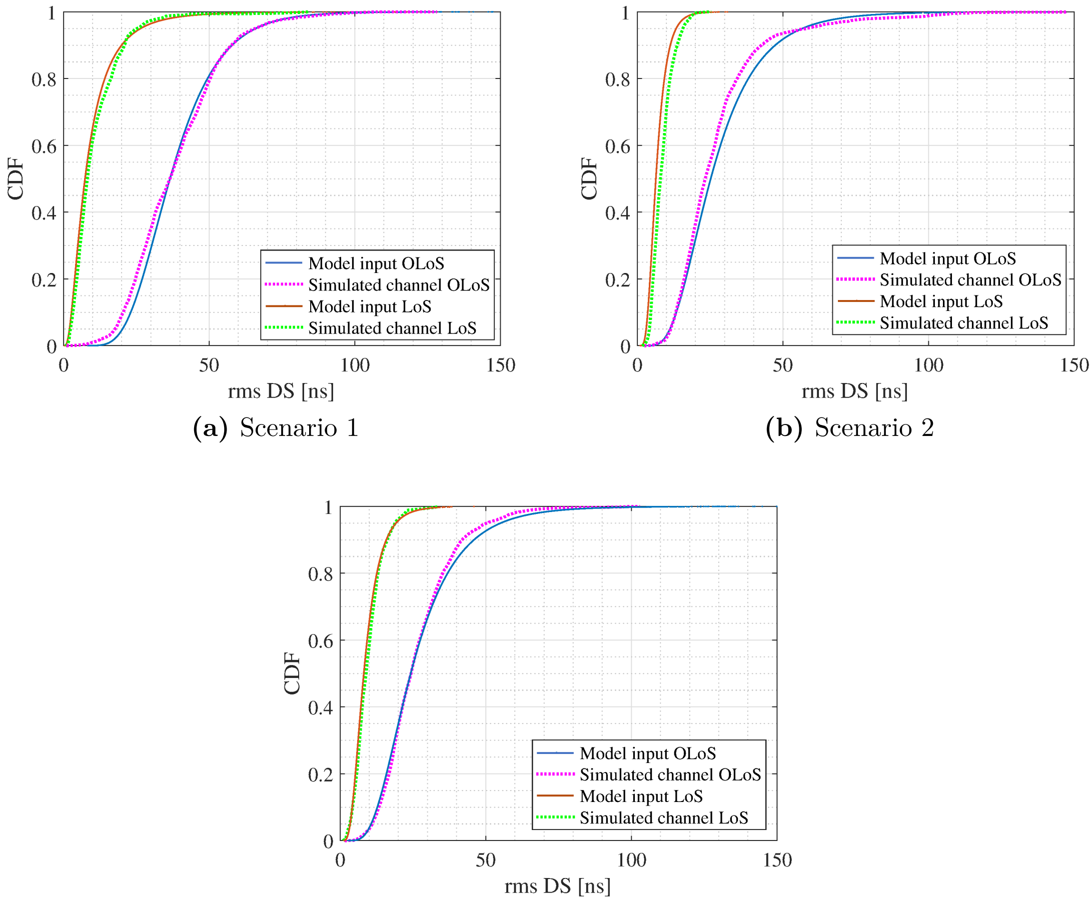

(a) Scenario 1

(b) Scenario 2

(c) Scenario 3

Figure 6.5: Comparison of the distribution of the RMS delay spread for the three scenarios in urban environment.

The LoS only corresponds to the part of the channel prior to the collision in which the Tx-Rx distance is shorter than 15 m in Scenario 1 and 9 m in Scenario 2 and Scenario 3. The results from the DS are presented in Figure 6.5. As expected, the DS in LoS condition is smaller than the DS in NLoS condition in all scenarios. It can be seen that the results from the simulated channels and the model input have almost perfect match in all scenarios in both the LoS and OLoS propagation conditions. In Scenario 1, the measured mean values of the DS are 7.41 ns and 36.31 ns for the LoS and NLoS, respectively. The DS mean values from the simulated channels follow the measured ones with 8.32 ns and 34.67 ns for the LoS and NLoS, respectively. Similar agreement is also observed between the model input and the simulated channels in terms of the mean and the standard deviation values of the DS in all scenarios as summarized in Tables 6.1-6.3.

6.2.3 Narrowband K-factor

The KF provides an indication of the energy proportion of the MPCs and hence quantifies the multipath richness of the communication channel. The KF is defined in Equation (5.3) as the ratio of the energy of the dominant component that consists of the LoS component and the unresolved ground reflection to the energy of all other components. Similar to the DS, the KF is also validated with distinction between LoS, OLoS, and NLoS propagation conditions, as shown in Figure 6.6. The KF is calculated only for the LoS part of the channel in Scenario 1. In Scenario 2 and Scenario 3, the KF is calculated for both the LoS and the OLoS parts of the channel. In Scenario 1, the mean and standard deviation values of the KF in the model input are 15.02 dB and 4.81 dB, respectively. The simulated channels show almost perfect agreement in terms of the KF with mean of 14.44 dB and standard deviation of 4.98 dB.

It can also be observed that the KF values extracted from the simulated channels in Scenario 2 and Scenario 3 almost perfectly follow the KF in the model input in both LoS and OLoS propagation conditions.

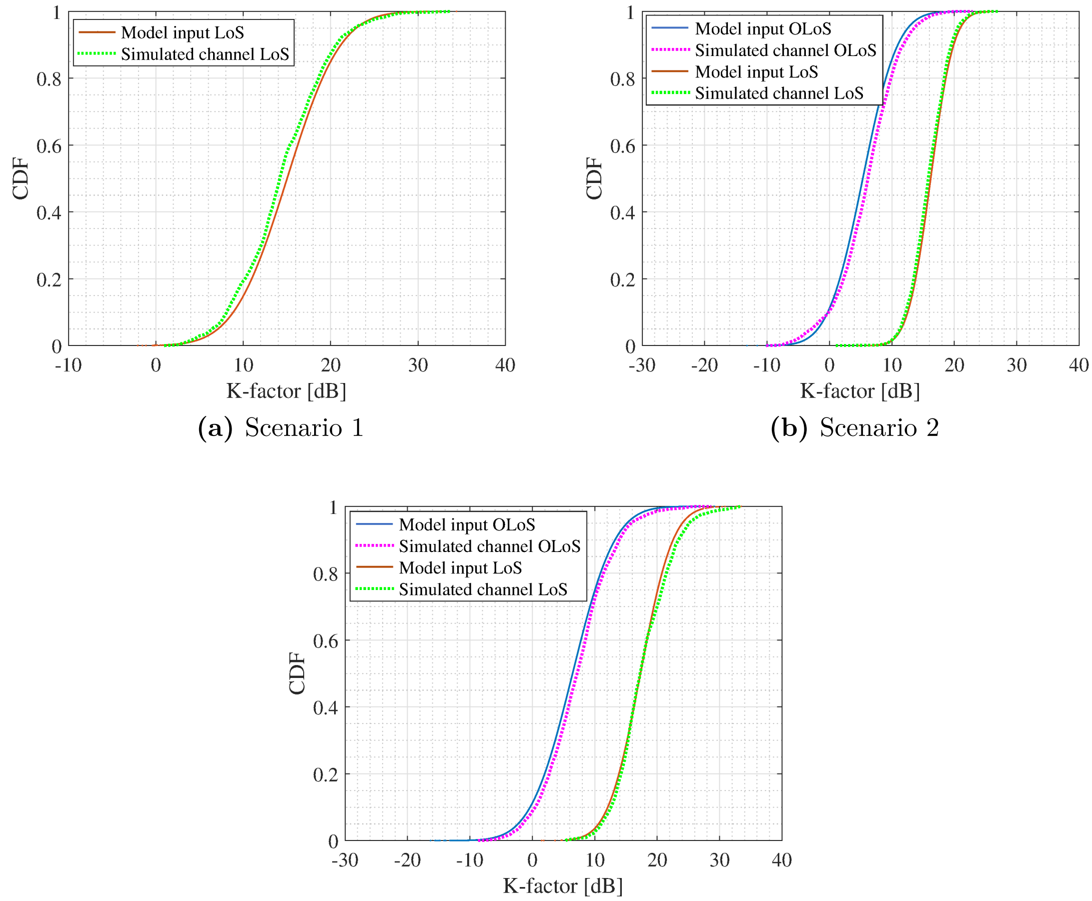

(a) Scenario 1 (b) Scenario 2 (c) Scenario 3

Figure 6.6: Comparison of the distribution of the narrowband K-factor for the three scenarios in urban environment.

6.2.4 Angular Spread

In contrary to the KF and DS, the angular spreads are evaluated with no distinction between LoS, OLoS, and NLoS propagation conditions. The complete data set is used to estimate the ASD and ASA. Figure 6.7 depicts the comparison between the simulated channels and the model input in terms of the ASD. It can be observed that the CDFs from the model input have tails with significantly larger ASD than those of the simulated channels.

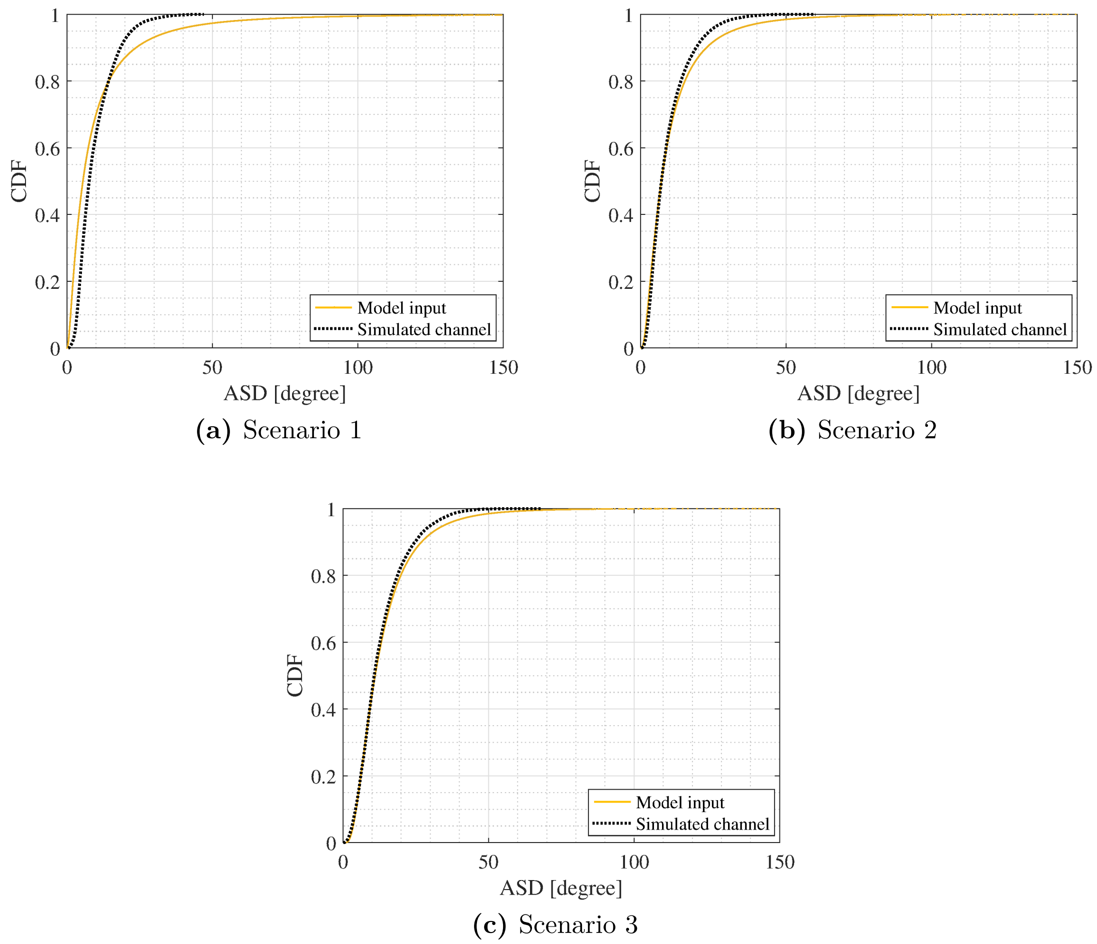

Figure 6.7: Comparison of the distribution of the azimuth spread of departure for the three scenarios in urban environment.

The simulated channels in Scenario 1 result in larger ASD with mean of 7.76° in comparison to 5.50° in the model input. However, better agreement can be seen in Scenario 2 and Scenario 3. The mismatch in Scenario 1 could be attributed to the errors in estimating path angles in NLoS. As discussed in Chapter 4, the locations of scatterers are estimated using the delay and Doppler of the MPCs. These locations

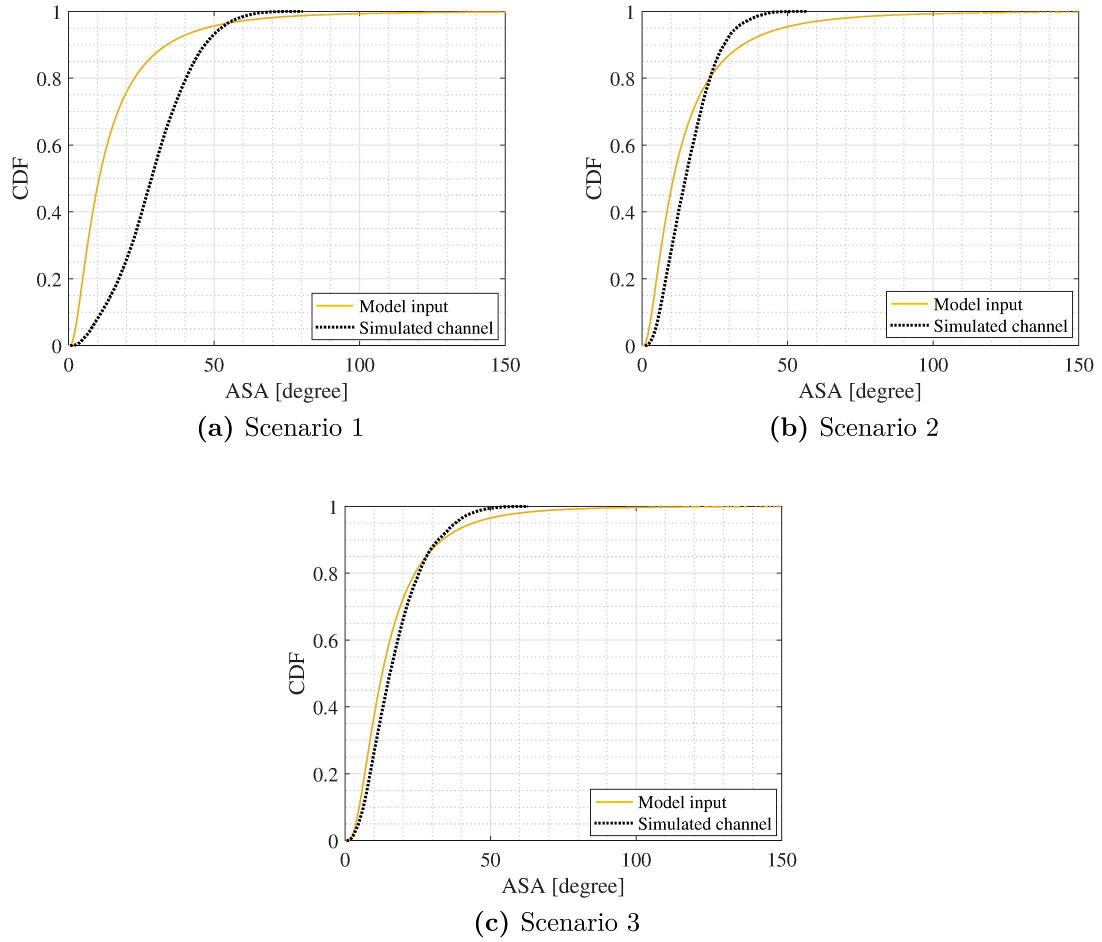

Figure 6.8: Comparison of the distribution of the azimuth spread of arrival for the three scenarios in urban environment.

together with the position of the Tx and the Rx are employed to estimate the AoD and AoA. However, during NLoS in Scenario 1, the MPCs have a short lifetime and a weak power which results in significant phase estimation errors and consequently cause less reliable scatterers locations estimation which may explain the errors in the estimated path angles and angular spreads.

The results for the ASA are shown in Figure 6.8. In Scenario 1, the simulated channels produce much larger ASA than the model input with a mean of 25.12° compared to 10.47° in the model input. The results for Scenario 2 and Scenario

3, however, show better match. As summarized in Tables 6.1-6.3, the standard deviation values in the model input are smaller than those of the simulated channels. As a result, the CDFs from the model input have tails with significantly larger ASA.

Parameters		**Model input**		**Simulated channels**	
		LoS	**NLoS**	**LoS**	**NLoS**
SF [dB]	μ	0	0	0	0
	σ	3.90	3.90	3.35	3.35
Corr.distance [m]	d_c	8.20	8.20	10.33	10.33
K-factor [dB]	μ	15.02	N/A	14.44	N/A
	σ	4.81	N/A	4.98	N/A
Corr.distance [m]	d_c	8.01	N/A	8.83	N/A
DS [$\log_{10}(s)$]	μ	-8.13	-7.44	-8.08	-7.46
	σ	0.34	0.16	0.31	0.19
Corr.distance [m]	d_c	8.97	49.69	9.08	50.16
ASD [$\log_{10}$ (°)]	μ	0.74	0.74	0.89	0.89
	σ	0.50	0.50	0.29	0.29
Corr.distance [m]	d_c	37.11	37.11	52.04	52.04
ASA [$\log_{10}$ (°)]	μ	1.02	1.02	1.40	1.40
	σ	0.40	0.40	0.25	0.25
Corr.distance [m]	d_c	48.95	48.95	55.71	55.71

Table 6.1: Comparison of LSPs for Scenario 1.

Another possible reason that could contribute to the observed deviations between the model input and simulated channels in terms of angular spreads is the scattering model used in the channel model implementation. As explained in Section 2.4.2, during the procedure of the channel generation, a double-bounce model is considered. During a channel segment, the positions of the scatterers stay fixed and are used to update the path delays and angles at each measurement snapshot. However, due to the limitation of the SISO measurements, a single-bounce model is considered in the parameterization of the channel model where only the last-bounce scatterers are localized.

Parameters		Model input LoS	Model input OLoS	Simulated channels LoS	Simulated channels OLoS
SF [dB]	μ	0	0	0	0
	σ	1.80	1.80	2.82	2.82
Corr.distance [m]	d_c	2.27	2.27	5.54	5.54
K-factor [dB]	μ	16.22	5.34	15.90	5.93
	σ	2.88	4.38	2.87	4.80
Corr.distance [m]	d_c	4.42	30.58	4.57	46.05
DS [$\log_{10}(s)$]	μ	-8.19	-7.60	-8.10	-7.62
	σ	0.19	0.21	0.18	0.21
Corr.distance [m]	d_c	4.42	70	4.57	59.45
ASD [$\log_{10}$ (°)]	μ	0.86	0.86	0.86	0.86
	σ	0.39	0.39	0.32	0.32
Corr.distance [m]	d_c	63.23	63.23	66.03	66.03
ASA [$\log_{10}$ (°)]	μ	1.03	1.03	1.14	1.14
	σ	0.39	0.39	0.26	0.26
Corr.distance [m]	d_c	66.17	66.17	71.48	71.48

Table 6.2: Comparison of LSPs for Scenario 2.

6.3 Correlation Distances

Th correlation distances of the LSPs are summarized in Tables 6.1, 6.2, and6.3. As discussed in Section 5.2, the correlation distance is calculated from the autocorrelation function of the evaluated LSP and used as a model input to simulate channels that maintain the spatial correlation observed in the measured channels. It must be noted that when the 2D correlated maps of the LSPs are generated during channel simulation, the cross-correlations between LSP pairs are applied to the correlated maps (see Step A. in Section 2.4.2). Therefore, correlation distances of LSPs are distorted and not anymore independent from each other. It can be noticed that the simulated channels in all scenarios show an increase in the correlation distances of most LSPs. This mismatch between the model input and the simulated channels in terms of correlation distance, due to the aforementioned cross-correlation, is inevitable. On the other hand, when a LSP shows insignificant correlation with the other LSP, the change in its correlation distance will be small. For example, in Scenario 3 the ASD has almost no correlation with the other LSPs in the model input. As a result, the correlation distance calculated from the simulated channels has an almost perfect agreement with the model input.

Parameters		**Model input**		**Simulated channels**	
		LoS	**OLoS**	**LoS**	**OLoS**
SF [dB]	μ	0	0	0	0
	σ	4.69	4.69	6.31	6.31
Corr.distance [m]	d_c	7.60	7.60	16.43	16.43
K-factor [dB]	μ	17.32	6.44	16.76	7.18
	σ	4.09	5.31	4.42	5.36
Corr.distance [m]	d_c	4.23	26.97	3.07	40.89
DS [$\log_{10}(s)$]	μ	-8.09	-7.62	-8.07	-7.62
	σ	0.23	0.22	0.23	0.20
Corr.distance [m]	d_c	4.64	57.88	3.19	54.60
ASD [$\log_{10}$ (°)]	μ	1.04	1.04	1.02	1.02
	σ	0.30	0.30	0.30	0.30
Corr.distance [m]	d_c	55.61	55.61	56.24	56.24
ASA [$\log_{10}$ (°)]	μ	1.11	1.11	1.16	1.16
	σ	0.33	0.33	0.28	0.28
Corr.distance [m]	d_c	54.48	54.48	58.12	58.12

Table 6.3: Comparison of LSPs for Scenario 3.

6.4 Cross-correlation Parameters

Table 6.4 summarizes the mean cross-correlation values of LSPs pairs that were set to the model input in comparison with the values that are calculated from the simulated channels. These values, which correspond to the model input, are the same as in Table 5.2. Note that, all cross-correlation matrices are positive definite. There are 5 different LSPs which result in 10 cross-correlation values. For each scenario, 10 values are obtained from the measurements and 10 values from the simulated channels. The cross-correlation values measure the inter-dependency between each pair of the LSPs and no distinction between different propagation conditions is made for the calculation of the cross-correlation, i.e., the complete data set of each measurement run is considered. Cross-correlation coefficients take values from -1 to 1. A negative coefficient indicates a decrease in parameter x if parameter y increases and vice versa. Positive coefficient means that x and y increase and decrease simultaneously. When the coefficient is zero there is no dependency between the two parameters.

In all scenarios, the cross-correlations between SF, KF, and DS calculated from the simulated channels are in good agreement with the model input. The SF is positively correlated with the KF while negatively correlated with the DS, i.e., when the SF increases, the K-factor increases and the DS decreases. In all scenarios, the DS and the KF have a strong negative correlation, as expected. A positive correlation in all scenarios between the ASD and ASA is also observed in both the model input and the simulated channels, however, a mismatch is noticed. The ASD corss-correlations with SF, KF, and DS obtained from the measurements, i.e., model input, in the three scenarios are not consistent. For example, the ASD has positive correlation of 0.28 with the SF in Scenario 1, negative correlation of -0.21 in Scenario 2, and no correlation in Scenario 3. Nevertheless, the ASD shows weak or no dependency on the SF, KF and DS. Similarly, the ASA shows no correlation with the KF and DS in all scenarios, while it has weak dependency on the SF in Scenarios 2 and 3. On the other hand, the results from the simulated channels do not show inconsistency. In all scenarios, both ASD and ASA are negatively correlated with the SF and KF and positively correlated with the DS. However, in most cases, a significant mismatch between the model input and the simulated channels is noticed. For example, the ASD shows no dependency on the KF in the model input in Scenario 1 and Scenario 3 and has a positive correlation of 0.25 in Scenario 2. However, the values calculated from the simulated channels show a strong positive correlation in all scenarios. Similar low agreement is noticed in ASD-SF and ASD-DS correlation values. The difference in scattering model and the estimation error of the angular spreads discussed in Section 6.2.4 can be partially explained by the aforementioned mismatch.

Cross-correlation		**Model input**					**Simulated channels**				
		SF	KF	DS	ASD	ASA	SF	KF	DS	ASD	ASA
Scenario 1	SF	1	0.50	-0.42	0.28	-0.07	1	0.61	-0.34	-0.07	-0.01
	KF		1	-0.86	0	-0.01		1	-0.78	-0.44	-0.35
	DS			1	-0.33	-0.04			1	0.09	0.48
	ASD				1	0.58				1	0.31
	ASA					1					1
Scenario 2	SF	1	0.35	-0.30	-0.21	-0.36	1	0.35	-0.30	-0.01	-0.11
	KF		1	-0.87	0.25	-0.01		1	-0.91	-0.50	-0.63
	DS			1	-0.13	0.07			1	0.47	0.58
	ASD				1	0.63				1	0.28
	ASA					1					1
Scenario 3	SF	1	0.63	-0.51	-0.07	-0.26	1	0.49	-0.49	-0.21	-0.26
	KF		1	-0.85	0	-0.1		1	-0.82	-0.48	-0.55
	DS			1	0.02	-0.07			1	0.44	0.45
	ASD				1	0.5				1	0.16
	ASA					1					1

Table 6.4: Comparison of cross-correlation coefficients for the three scenarios in urban environment.

6.5 Summary

In this chapter, The WINNER-type channel model for V2VRU communications in critical accident scenarios is validated. The measured channels are simulated using QuaDRiGa implementation based on the proposed model parametrization. In addition to the path loss, the distributions of the LSPs, their correlation distances, and the cross-correlation coefficients between all LSPs pairs are selected as validation metrics. The LSPs are estimated from the simulated channels in the same way they were estimated from the measured channels and then fitted to a log-normal distribution.

It can be noted that the channel model clearly provides an almost perfect match in terms of path loss in all three measured scenarios. Moreover, the results show that the proposed model has a good agreement with the measurements in terms of shadow fading in Scenario 1. However, some mismatch is observed in Scenario 2 and Scenario 3, in which the SF extracted from the simulated channels has larger standard deviation compared to the measured channels. The findings for the DS and the KF show almost perfect agreements between the simulated and measured channels. In terms of the ASD and ASA, the proposed channel model in Scenario 1 shows some mismatch. However, better agreement can be seen in Scenario 2 and Scenario 3. Furthermore, based on the correlation distance results, it is concluded that due to applying the cross-correlations between LSPs pairs, the correlation distances of LSPs are not independent anymore. Therefore, LSPs, which have high correlation values with other LSPs, experience an increase in their correlation distances. From the cross-correlation results, it is noticed that the cross-correlations between SF, KF, and DS calculated from the simulated channels are in good agreement with the measured channels in all scenarios. However, the cross-correlations related to ASD and ASA show a mismatch.

Generally, it can be concluded that the GSCM with the proposed model parameters is able to produce fairly similar statistics as the measured channels. The proposed model provides a good representation for the propagation channel in V2VRU communications in the considered scenarios.

7

Summary and Future Work

Vehicle-to-vulnerable road users (V2VRUs) communication overcomes the limitations of sensor-based collision avoidance systems and provides 360° of awareness. In order to develop a reliable communication system, realistic channel model in relevant accident scenarios are of immense importance, but had yet not been thoroughly investigated or modeled. The primary target of this thesis is to develop a geometry-based stochastic channel model (GSCM) for V2VRUs communication.

For this purpose, two SISO channel measurement campaigns were conducted. Both campaigns were executed using the RUSK-DLR channel sounder at a carrier frequency of $f_\mathrm{c} = 5.2\,\mathrm{GHz}$ and a bandwidth of $B = 120\,\mathrm{MHz}$. The first campaign was executed in open-field controlled environment considering an accident scenario between a vehicle and a pedestrian. This location made it possible to isolate and study the impact on the received power by the different elements in the propagation environment as well as by the mobility of the Tx and Rx. The second measurement campaign was conducted in urban environment. The three most critical accident scenarios involving pedestrians and cyclists were considered. The proposed channel model in this thesis is based on data collected during this campaign.

Based on the measurement data in open-field scenarios, path loss models were proposed. The two-ray model was found to provide a good fit to the measured path loss in the LoS scenario with a static tripod as a receiver. By replacing the static tripod with a moving pedestrian, rapid fluctuations of the measured path loss were observed. These fluctuations were found to be the result of reflections from the body of pedestrian and the change in the antenna height due to the pedestrian movement. The losses in power due to crowd shadowing and blockage of the LoS by parked vehicles were also investigated and quantified. Based on the path loss models, the shadow fading was then extracted to study its spatial correlation. The autocorrelation functions of the measured shadow fading were calculated and modeled. Furthermore, it is found that the most critical accident scenarios that involve pedestrians and cyclists occur when the visibility is blocked by parked vehicles. Therefore, motivated by this fact, a 3D ray tracing tool was developed to detect the diffraction edges on the parked vehicles. The Fresnel-Kirchoff parameter was then used to calculate the knife-edge diffraction loss. Moreover, based on the measurement data in urban scenarios, the path loss was calculated and a multi-slope log-distance path loss model was proposed for each scenario to later be used as a channel model parameter.

Due to the non-stationarity nature of the vehicular channels, the large scale parameters (LSPs) need to be evaluated within regions, i.e. where the wide-sense stationary (WSS) assumption holds. Therefore, based on the measurement data in the urban environment, the non-stationarity of the V2VRU channel was investigated. The length of the WSS regions, i.e., stationarity distance, was obtained by estimating the generalized local scattering function and its collinearity.

In order to estimate the LSPs, the multipath parameters were estimated using the KEST algorithm. The time-variant CIR in the urban environment was found to be highly cluttered by diffuse MPCs (DMCs). Therefore, a novel method to separate specular MPCs (SMCs) and DMCs based on the density of their neighboring MPCs was proposed. Furthermore, an algorithm for SMCs tracking based on their delay and magnitude was presented. Having the SMCs tracked over time, each SMC is then related to a physical scatterer in the propagation environment. Localization of the scatterers was done using a joint delay-Doppler estimation algorithm. The estimated positions of the scatterers were then used to estimate the AoD and AoA.

A full parametrization for the WINNER-type GSCM was proposed. The LSPs were estimated in the power and delay domain, i.e., shadow fading (SF), delay spread (DS), narrowband K-factor (KF), and in the angular domain, i.e., azimuth angle of departure (AoD), azimuth angle of arrival (AoA). The log-normal distribution was found to provide a good fit to the distributions of the LSPs. Furthermore, the spatial correlations of the LSPs were analyzed and their correlation distances were calculated. In order to ensure the channel spatial consistency, the cross-correlation coefficients among the LSPs were also calculated. The model parameters were then used as an input to the QuaDRiGa channel simulator.

Finally, the proposed channel model was validated by comparing the simulated channels with the measured channels. In addition to the path loss, the distributions of the LSPs, their correlation distances, and the cross-correlation coefficients between all LSPs pairs were selected as validation metrics. It can be concluded that the GSCM with the proposed model parameters is able to produce fairly similar statistics as the measured channels. The proposed model provides good representation for the V2VRU propagation channel in the considered scenarios.

Future work related to this research could begin with including the DMC in the channel model to account for their contribution to the received power. Due to time constraints, only the measured data in one location has been analyzed and used to model the channel. Further work is needed to analyze the measured data collected in the other two locations in order to improve the channel model. Moreover, additional measurement campaigns are required to cover other interesting accidents scenarios. MIMO measurement campaigns would be valuable to improve the estimation of angular spreads and scatterer locations.

Bibliography

[1] *Road traffic injuries.* URL: http://www.who.int/violence_injury_prevention/road_traffic/en/ (visited on 09/25/2018).

[2] M. DaSilva, J. Smith, and W. Najm. *Analysis of pedestrian crashes.* Tech. rep. 2003.

[3] M. Kuehn, T. Hummel, and A. Lang. “Cyclist-car accidents–their consequences for cyclists and typical accident scenarios”. In: *Proceedings of the 24th International Conference on the Enhanced Safety of Vehicles.* 2015.

[4] F. de Ponte Müller. “Survey on ranging sensors and cooperative techniques for relative positioning of vehicles”. In: *Sensors* 17.2 (2017), p. 271.

[5] D. Geronimo et al. “Survey of pedestrian detection for advanced driver assistance systems”. In: *IEEE transactions on pattern analysis and machine intelligence* 32.7 (2010), pp. 1239–1258.

[6] P. Hurney et al. “Review of pedestrian detection techniques in automotive far-infrared video”. In: *IET intelligent transport systems* 9.8 (2015), pp. 824–832.

[7] X. Wu et al. “Cars talk to phones: A DSRC based vehicle-pedestrian safety system”. In: *Vehicular Technology Conference (VTC Fall), 2014 IEEE 80th.* IEEE. 2014, pp. 1–7.

[8] M. Jutila et al. “ITS-G5 performance improvement and evaluation for vulnerable road user safety services”. In: *IET Intelligent Transport Systems* 11.3 (2017), pp. 126–133.

[9] W. Viriyasitavat et al. “Vehicular Communications: Survey and Challenges of Channel and Propagation Models”. In: *IEEE Vehicular Technology Magazine* 10.2 (June 2015), pp. 55–66. ISSN: 1556-6072. DOI: 10.1109/MVT.2015.2410341.

[10] D. W. Matolak. “Modeling the vehicle-to-vehicle propagation channel: A review”. In: *Radio Science* 49.9 (2014), pp. 721–736.

[11] A. F. Molisch et al. “A survey on vehicle-to-vehicle propagation channels”. In: *IEEE Wireless Communications* 16.6 (Dec. 2009), pp. 12–22. ISSN: 1536-1284. DOI: 10.1109/MWC.2009.5361174.

[12] L. Bernado et al. “Delay and Doppler spreads of nonstationary vehicular channels for safety-relevant scenarios”. In: *IEEE Transactions on Vehicular Technology* 63.1 (2014), pp. 82–93.

[13] A. Paier. “The vehicular radio channel in the 5 GHz band”. PhD thesis. 2010.

[14] R. Verdone and A. Zanella. *Pervasive mobile and ambient wireless communications: COST action 2100*. Springer Science & Business Media, 2012.

[15] Y. d. J. Bultitude and T. Rautiainen. “IST-4-027756 WINNER II D1. 1.2 V1. 2 WINNER II Channel Models”. In: *EBITG, TUI, UOULU, CU/CRC, NOKIA, Tech. Rep* (2007).

[16] I. Rashdan et al. “Large-Scale Fading Characteristics and Models for Vehicle-to-Pedestrian Channel at 5-GHz”. In: *IEEE Access* 7 (2019), pp. 107648–107658.

[17] I. Rashdan et al. “Measurement-based geometrical characterisation of the vehicle-to-vulnerable-road-user communication channel”. In: *IET Microwaves, Antennas & Propagation* (2020).

[18] I. Rashdan, F. de Ponte Muller, and S. Sand. “Analysis of Communication Requirements for CACC in Stop-and-Go Behavior for Energy Efficient Driving”. In: *2016 IEEE 84th Vehicular Technology Conference (VTC-Fall)*. 2016, pp. 1–5. DOI: 10.1109/VTCFall.2016.7880905.

[19] I. Rashdan, F. de Ponte Muller, and S. Sand. “Performance Evaluation of Traffic Information Dissemination Protocols for Dynamic Route Planning Application in VANETs”. In: *2016 IEEE 84th Vehicular Technology Conference (VTC-Fall)*. 2016, pp. 1–5. DOI: 10.1109/VTCFall.2016.7881161.

[20] I. Rashdan, S. Sand, and F. de Ponte Müller. “ITS-G5 Challenges and 5G Solutions for Vehicular Platooning”. In: *WWRF37, Kassel, Germany*. Jan. 2016.

[21] I. Rashdan et al. “Performance Evaluation of Vehicle-to-Vehicle Communication for Cooperative Collision Avoidance at Urban Intersections”. In: *2017 IEEE 86th Vehicular Technology Conference (VTC-Fall)*. Sept. 2017, pp. 1–5. DOI: 10.1109/VTCFall.2017.8288274.

[22] I. Rashdan et al. “Vehicle-to-Pedestrian Channel Characterization: Wideband Measurement Campaign and First Results”. In: *IEEE 12th European Conference on Antennas and Propagation (EuCAP)*. London, UK, Apr. 2018.

[23] I. Rashdan et al. “Large Scale Fading Characteristics for Vehicle-to-Cyclist Channel in Urban Environment at 5 GHz”. In: *2020 14th European Conference on Antennas and Propagation (EuCAP)*. 2020, pp. 1–5. DOI: 10.23919/EuCAP48036.2020.9135985.

[24] I. Rashdan et al. “Measurement-based Geometrical Characterization of the Vehicle-to-Pedestrian Channel”. In: *2019 13th European Conference on Antennas and Propagation (EuCAP)*. IEEE. 2019, pp. 1–5.

[25] I. Rashdan et al. “Diffuse Multipath Analysis of Vehicle-to-Vulnerable Road User Channel in Urban Environment”. In: *2021 15th European Conference on Antennas and Propagation (EuCAP)*. 2021, pp. 1–5. DOI: 10.23919/EuCAP51087.2021.9411391.

[26] M. F. Iskander and Z. Yun. “Propagation prediction models for wireless communication systems”. In: *IEEE Transactions on microwave theory and techniques* 50.3 (2002), pp. 662–673.

[27] J. D. Parsons and P. J. D. Parsons. *The mobile radio propagation channel*. Vol. 2. Wiley New York, 2000.

[28] O. Landron, M. J. Feuerstein, and T. S. Rappaport. “A comparison of theoretical and empirical reflection coefficients for typical exterior wall surfaces in a mobile radio environment”. In: *IEEE Transactions on Antennas and Propagation* 44.3 (1996), pp. 341–351.

[29] P. Beckmann and A. Spizzichino. “The scattering of electromagnetic waves from rough surfaces”. In: *ah* (1987).

[30] S. Salous. *Radio propagation measurement and channel modelling*. John Wiley & Sons, 2013.

[31] P. Series. “Propagation by diffraction”. In: *Recommendation ITU-R P. 526-13* (2013).

[32] S. Priebe, M. Jacob, and T. Kürner. “Calibrated broadband ray tracing for the simulation of wave propagation in mm and sub-mm wave indoor communication channels”. In: *European Wireless 2012; 18th European Wireless Conference 2012*. VDE. 2012, pp. 1–10.

[33] H. C. Nguyen et al. “Evaluation of empirical ray-tracing model for an urban outdoor scenario at 73 GHz E-band”. In: *2014 IEEE 80th Vehicular Technology Conference (VTC2014-Fall)*. IEEE. 2014, pp. 1–6.

[34] T. Huschka. “Ray tracing models for indoor environments and their computational complexity”. In: *5th IEEE International Symposium on Personal, Indoor and Mobile Radio Communications, Wireless Networks-Catching the Mobile Future*. Vol. 2. IEEE. 1994, pp. 486–490.

[35] T. Fugen et al. “Capability of 3-D ray tracing for defining parameter sets for the specification of future mobile communications systems”. In: *IEEE Transactions on antennas and propagation* 54.11 (2006), pp. 3125–3137.

[36] G. Acosta-Marum. “Measurement, modeling, and OFDM synchronization for the wideband mobile-to-mobile channel”. PhD thesis. Georgia Institute of Technology, 2007.

[37] I. S. Association et al. “Wireless lan medium access control (mac) and physical layer (phy) specifications amendment 6: Wireless access in vehicular environments”. In: *Standard IEEE* 802.11 (2010).

[38] P. Heino et al. *WINNER+ final channel models*. Tech. rep. Tech. Rep, 2010.

[39] 3. T. 3. v12.2.0. *Study on 3D channel model for LTE*. Tech. rep. Tech. Rep, 2015.

[40] S. Jaeckel. “Quasi-deterministic channel modeling and experimental validation in cooperative and massive MIMO deployment topologies”. PhD thesis. Dissertation, Ilmenau, TU Ilmenau, 2017, 2017.

[41] C. Gustafson et al. “The COST IRACON Geometry-Based Stochastic Channel Model for Vehicle-to-Vehicle Communication in Intersections”. In: *IEEE Transactions on Vehicular Technology* 69.3 (2020), pp. 2365–2375. DOI: 10.1109/TVT.2020.2964277.

[42] H. Yi et al. “Characterization for the Vehicle-to-Infrastructure Channel in Urban and Highway Scenarios at the Terahertz Band”. In: *IEEE Access* 7 (2019), pp. 166984–166996. DOI: 10.1109/ACCESS.2019.2953890.

[43] G. Makhoul, R. D’Errico, and C. Oestges. “Wideband Vehicle to Pedestrian Propagation Channel Characterization and Modeling”. In: *IEEE 12th European Conference on Antennas and Propagation (EuCAP)*. London, UK, Apr. 2018.

[44] G. Makhoul, R. D’Errico, and C. Oestges. “Wideband Measurement-Based Vehicle-to-Pedestrian Channel Models”. In: *IEEE Transactions on Vehicular Technology* 68.10 (2019), pp. 9339–9347. DOI: 10.1109/TVT.2019.2936629.

[45] G. Makhoul, R. D’Errico, and C. Oestges. “Characterization of Vehicle to Pedestrian Correlation Properties”. In: *2020 IEEE International Symposium on Antennas and Propagation and North American Radio Science Meeting*. 2020, pp. 1113–1114. DOI: 10.1109/IEEECONF35879.2020.9330040.

[46] M. G. Doone and S. L. Cotton. “First-order characteristics of the person-to-vehicle channel at 5.8 GHz”. In: *Antennas and Propagation (EuCAP), 2014 8th European Conference on*. IEEE. 2014, pp. 848–851.

[47] M. G. Doone et al. “Pedestrian-to-vehicle communications in an urban environment: Channel measurements and modeling”. In: *IEEE Transactions on Antennas and Propagation* 67.3 (2018), pp. 1790–1803.

[48] J. J. Anaya et al. "Vehicle to pedestrian communications for protection of vulnerable road users". In: *2014 IEEE Intelligent Vehicles Symposium Proceedings*. June 2014, pp. 1037–1042. DOI: 10.1109/IVS.2014.6856553.

[49] Z. Liu et al. "Implementation and performance measurement of a V2X communication system for vehicle and pedestrian safety". In: *International Journal of Distributed Sensor Networks* 12.9 (2016), p. 1550147716671267.

[50] P. Sewalkar, S. Krug, and J. Seitz. "Towards 802.11 p-based vehicle-to-pedestrian communication for crash prevention systems". In: *Ultra Modern Telecommunications and Control Systems and Workshops (ICUMT), 2017 9th International Congress on*. IEEE. 2017, pp. 404–409.

[51] M. Bagheri, M. Siekkinen, and J. K. Nurminen. "Cloud-based pedestrian road-safety with situation-adaptive energy-efficient communication". In: *IEEE Intelligent transportation systems magazine* 8.3 (2016), pp. 45–62.

[52] M. Bagheri, M. Siekkinen, and J. K. Nurminen. "Cellular-based vehicle to pedestrian (V2P) adaptive communication for collision avoidance". In: *Connected Vehicles and Expo (ICCVE), 2014 International Conference on*. IEEE. 2014, pp. 450–456.

[53] D. S. Baum et al. "An interim channel model for beyond-3G systems: extending the 3GPP spatial channel model (SCM)". In: *2005 IEEE 61st Vehicular Technology Conference*. Vol. 5. IEEE. 2005, pp. 3132–3136.

[54] K. Bakowski and K. Wesolowski. "Change the channel". In: *IEEE Vehicular Technology Magazine* 6.2 (2011), pp. 82–91.

[55] G. L. Turin et al. "A statistical model of urban multipath propagation". In: *IEEE Transactions on Vehicular Technology* 21.1 (1972), pp. 1–9.

[56] T. S. Rappaport et al. *Wireless communications: principles and practice*. Vol. 2. prentice hall PTR New Jersey, 1996.

[57] H. Fernández et al. "Path loss characterization for vehicular communications at 700 MHz and 5.9 GHz under LOS and NLOS conditions". In: *IEEE Antennas and Wireless Propagation Letters* 13 (2014), pp. 931–934.

[58] M. Luo, G. Villemaud, and J.-M. Gorce. "Generation of 2D correlated random shadowing based on the deterministic MR-FDPF model". In: *EURASIP Journal on Wireless Communications and Networking* 2015.1 (2015), p. 208.

[59] I. Forkel, M. Schinnenburg, and M. Ang. "Generation of two-dimensional correlated shadowing for mobile radio network simulation". In: *WPMC, sep* 21 (2004), p. 43.

[60] T. Abbas et al. "A measurement based shadow fading model for vehicle-to-vehicle network simulations". In: *International Journal of Antennas and Propagation* 2015 (2015).

[61] T. W. Beck et al. "An examination of the runs test, reverse arrangements test, and modified reverse arrangements test for assessing surface EMG signal stationarity". In: *Journal of neuroscience methods* 156.1-2 (2006), pp. 242–248.

[62] M. Gudmundson. "Correlation model for shadow fading in mobile radio systems". In: *Electronics letters* 27.23 (1991), pp. 2145–2146.

[63] T. B. Sorensen. "Correlation model for slow fading in a small urban macro cell". In: *Personal, Indoor and Mobile Radio Communications, 1998. The Ninth IEEE International Symposium on.* Vol. 3. IEEE. 1998, pp. 1161–1165.

[64] Y. Zhang et al. "A novel spatial autocorrelation model of shadow fading in urban macro environments". In: *Global Telecommunications Conference, 2008. IEEE GLOBECOM 2008. IEEE.* IEEE. 2008, pp. 1–5.

[65] K. D. Mielenz. "Computation of Fresnel integrals. II". In: *Journal of research of the National Institute of Standards and Technology* 105.4 (2000), p. 589.

[66] J. Epstein and D. W. Peterson. "An experimental study of wave propagation at 850 Mc". In: *Proceedings of the IRE* 41.5 (1953), pp. 595–611.

[67] A. Paier et al. "Non-WSSUS vehicular channel characterization in highway and urban scenarios at 5.2 GHz using the local scattering function". In: *2008 international itg workshop on smart antennas.* IEEE. 2008, pp. 9–15.

[68] G. Matz. "On non-WSSUS wireless fading channels". In: *IEEE transactions on wireless communications* 4.5 (2005), pp. 2465–2478.

[69] A. Ispas et al. “Analysis of local quasi-stationarity regions in an urban macrocell scenario”. In: *2010 IEEE 71st Vehicular Technology Conference*. IEEE. 2010, pp. 1–5.

[70] D. Slepian. “Prolate spheroidal wave functions, Fourier analysis, and uncertainty—V: The discrete case”. In: *Bell System Technical Journal* 57.5 (1978), pp. 1371–1430.

[71] R. Thomä, M. Landmann, and A. Richter. “RIMAX—a maximum likelihood framework for parameter estimation in multidimensional channel sounding”. In: *Proceedings of the International Symposium on Antennas and Propagation (ISAP’04)*. Citeseer. 2004, pp. 53–56.

[72] B. H. Fleury et al. “Channel parameter estimation in mobile radio environments using the SAGE algorithm”. In: *IEEE Journal on selected areas in communications* 17.3 (1999), pp. 434–450.

[73] T. Jost et al. “Detection and tracking of mobile propagation channel paths”. In: *IEEE Transactions on Antennas and Propagation* 60.10 (2012), pp. 4875–4883.

[74] T. Jost et al. “Using an autoregressive model for DMC”. In: *2012 6th European Conference on Antennas and Propagation (EUCAP)*. IEEE. 2012, pp. 3504–3508.

[75] N. Savage et al. “Radio wave propagation through vegetation: Factors influencing signal attenuation”. In: *Radio Science* 38.5 (2003), pp. 9–1.

[76] M. Al-Nuaimi and A. Hammoudeh. “Measurements and predictions of attenuation and scatter of microwave signals by trees”. In: *IEE Proceedings-Microwaves, Antennas and Propagation* 141.2 (1994), pp. 70–76.

[77] N. Schneckenburger et al. “Reflector Localization for Geometrical Modeling the Air-Ground Channel”. In: *IEEE Transactions on Vehicular Technology* (2018).

[78] A. Richter. “Estimation of radio channel parameters: Models and algorithms”. In: ISLE. 2005.

[79] J. Poutanen et al. “Angular and shadowing characteristics of dense multipath components in indoor radio channels”. In: *IEEE Transactions on Antennas and Propagation* 59.1 (2010), pp. 245–253.

[80] A. Richter, J. Salmi, and V. Koivunen. “Distributed scattering in radio channels and its contribution to MIMO channel capacity”. In: *2006 First European Conference on Antennas and Propagation*. IEEE. 2006, pp. 1–7.

[81] G. Calcev et al. “A wideband spatial channel model for system-wide simulations”. In: *IEEE Transactions on Vehicular Technology* 56.2 (2007), pp. 389–403.

[82] M. Series. “Guidelines for evaluation of radio interface technologies for IMT-Advanced”. In: *Report ITU* 638 (2009), pp. 1–72.

[83] P. Kyosti. “WINNER II channel models”. In: *IST, Tech. Rep. IST-4-027756 WINNER II D1. 1.2 V1. 2* (2007).

[84] E. Tanghe et al. “Experimental analysis of dense multipath components in an industrial environment”. In: *IEEE Transactions on Antennas and Propagation* 62.7 (2014), pp. 3797–3805.

[85] B. Hanssens et al. “An extension of the RiMAX multipath estimation algorithm for ultra-wideband channel modeling”. In: *EURASIP journal on wireless communications and networking* 2018.1 (2018), p. 164.

[86] S. R. Saunders and A. Aragón-Zavala. *Antennas and propagation for wireless communication systems*. John Wiley & Sons, 2007.

[87] L. J. Greenstein, D. G. Michelson, and V. Erceg. “Moment-method estimation of the Ricean K-factor”. In: *IEEE communications letters* 3.6 (1999), pp. 175–176.

[88] v. 3GPP TR 25.996. *Spatial channel model for multiple input multiple output (MIMO) simulations*. Tech. rep. 3rd Generation Partnership Project (3GPP), 2003.